Reconstructing the paleoenvironment of an oxygenated Mesoproterozoic shoreline and its record of life

Sarah P. Slotznick[1], Nicholas L. Swanson-Hysell[2], Yiming Zhang[2], Katherine E. Clayton[3], Charles H. Wellman[4], Nicholas J. Tosca[5], and Paul K. Strother[6]

[1]Department of Earth Sciences, Dartmouth College, Hanover, NH, USA
[2]Department of Earth and Planetary Science, University of California, Berkeley, CA, USA
[3]Department of Earth Sciences, University of Oxford, Oxford, UK
[4]Department of Animal and Plant Sciences, University of Sheffield, Sheffield, UK
[5]Department of Earth Sciences, University of Cambridge, Cambridge, UK
[6]Department of Earth and Environmental Sciences, Weston Observatory of Boston College, Weston, MA, USA

Abstract

The Nonesuch Formation microbiota provide a window into ca. 1075 Ma life within the interior of ancient North America. The Nonesuch water body formed following the cessation of widespread volcanism within the Midcontinent Rift as the basin continued to subside. In northern Michigan and Wisconsin, the Copper Harbor Conglomerate records terrestrial alluvial fan and fluvial plain environments that transitioned into subaqueous lacustrine deposition of the Nonesuch Formation. These units thin towards a paleotopographic high associated with the Brownstone Falls angular unconformity. Due to these "Brownstone Highlands," we were able to explore the paleoenvironment laterally at different depths in contemporaneous deposits. Rock magnetic data constrain that when the lake was shallow it was oxygenated as evidenced by an oxidized mineral assemblage. Oxygen levels were lower at greater depth — in the deepest portions of the water body, anoxic conditions are recorded. An intermediate facies in depth and redox between these endmembers preserves detrital magnetite and hematite which can be present in high abundance due to the proximal volcanic highlands. This magnetic facies enabled the development of a paleomagnetic pole based on both detrital magnetite and hematite that constrains the paleolatitude of the lake to 7.1±2.8°N. Sediments of the intermediate facies preserve exquisite organic-walled microfossils with microfossils being less diverse to absent in the anoxic facies where amorphous organic matter is more likely to be preserved. The assemblage of cyanobacteria and eukaryotes (both photoautotrophs and heterotrophs) lived within the oxygenated waters of this tropical Mesoproterozoic water body.

This manuscript is the author's version of the publication:

Slotznick, S.P., Swanson-Hysell, N.L., Zhang, Y., Clayton, K., Wellman, C.H., Tosca, N.J., and Strother, P.K. (2023), Reconstructing the paleoenvironment of an oxygenated Mesoproterozoic shoreline and its record of life, *GSA Bulletin*, doi:10.1130/B36634.1..

INTRODUCTION

Ca. 1075 million years ago, portions of the North American Midcontinent Rift basin filled with water leading to the deposition of sediments that became the Nonesuch Formation (Fig. 1). Typically interpreted as a rift lake (e.g. Daniels (1982)), with some researchers suggesting a marine or estuarine environment (e.g. Moore et al. (1969)), this water body was host to diverse microbiota — a record of which is preserved as organic-walled microfossils of exceptional quality (Strother and Wellman, 2021). Despite their late Mesoproterozoic antiquity, the rocks of the Nonesuch Formation had a very mild post-depositional history due to the intracontinental tectonic setting in which they were deposited. While significant accommodation space developed through rift-driven tectonic subsidence, the lack of complete continental separation due to cessation of active rifting before Nonesuch Formation deposition allowed its preservation in the interior of cratonic North America. As a result, for its entire post-depositional history, the Nonesuch Formation has been located far from active continental margins that could have resulted in subsequent metamorphism. Apart from a spatially restricted zone of mineralization driven by migration of cupriferous brines (Mauk et al., 1992; Swenson et al., 2004), the very-low metamorphic grade of the Nonesuch Formation (Gallagher et al., 2017) results in excellent preservation and the ability to gain insight into Mesoproterozoic environmental conditions.

The remarkably preserved microfossil assemblage within the Nonesuch Formation records a diversity of life within the lake including both cyanobacteria and eukaryotes as well as simple multicellularity associated with some eukaryotic forms (Wellman and Strother, 2015; Strother and Wellman, 2016, 2021). While assignment of metabolism to the preserved eukaryotes is uncertain, they have been interpreted to include both photoautotrophs and heterotrophs (Strother and Wellman, 2021). Heterotrophic feeding mechanisms are interpreted to have included osmotrophy (ingesting dissolved organic compounds by osmosis) and probably phagotrophy (engulfment of particulate organic matter, even cells)(Strother and Wellman, 2021).

The typical paradigm for eukaryote evolution is that the first crown-group eukaryote to evolve required oxygen due to interpretations of eukaryotic evolutionary trees, the predominance of aerobic respiration in eukaryotes, and the necessity for oxygen in making certain biological compounds (sterols) contained

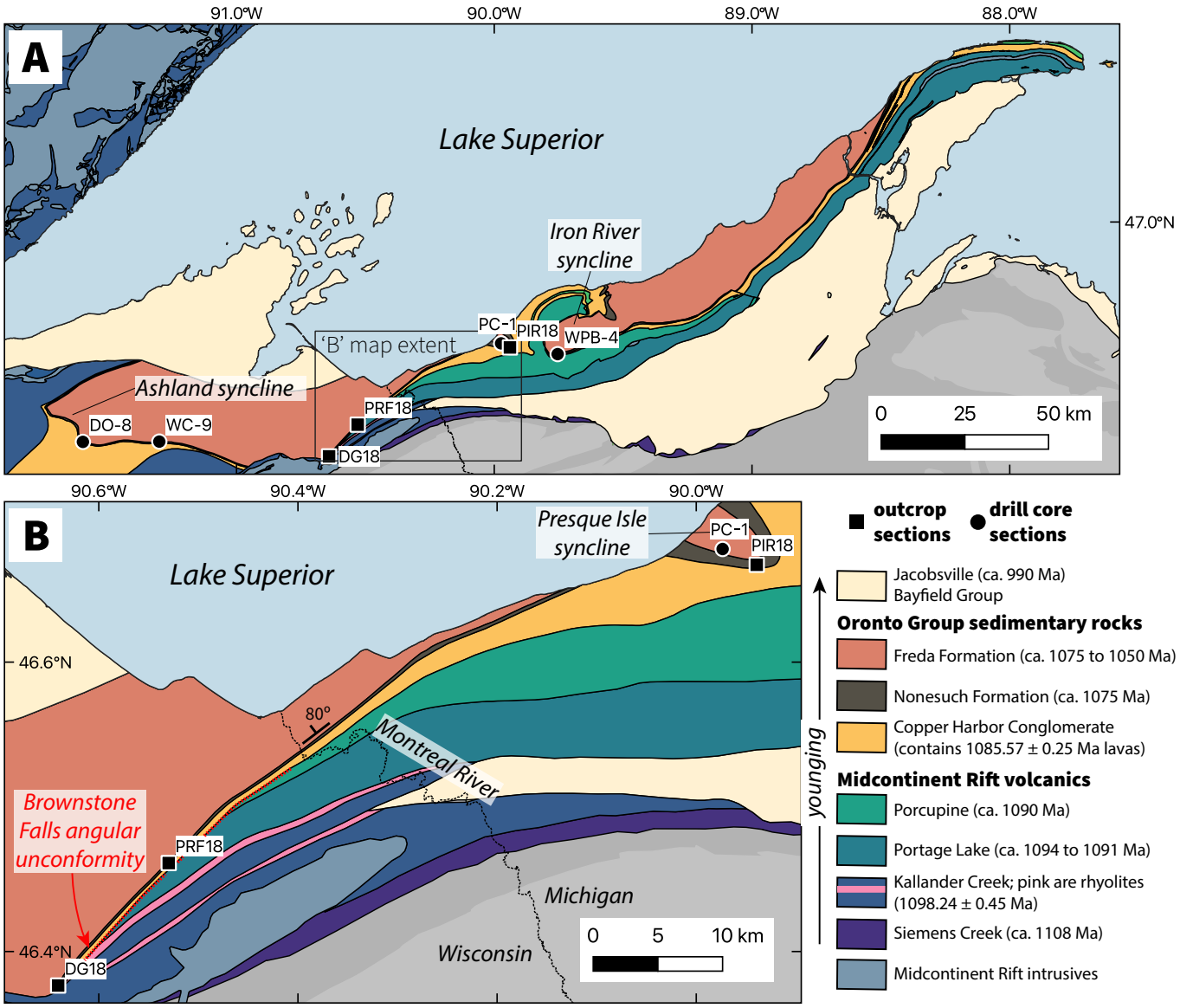

Figure 1: Geologic map of the region where the Nonesuch Formation outcrops and has been studied in stratigraphic drill core. Panel A shows the full extent of the Nonesuch Formation in northern Wisconsin and the Upper Peninsula of Michigan and the locations of studied outcrop and core sections. Panel B zooms in on the region of the Montreal River monocline from the Presque Isle River in the east to Brownstone Falls in the west where the sedimentary rocks of the Oronto Group rest on a post-rift unconformity (Brownstone Falls angular unconformity, red line). Geologic data are from Cannon et al. (1995) and Cannon et al. (1996) with minor modifications associated with new field data. As a result of this unconformity, the Copper Harbor Conglomerate is progressively in contact with older volcanic rocks to the southwest. The Copper Harbor Conglomerate and the Nonesuch Formation progressively thin to the southwest against this unconformity (Fig. 2). These lateral changes in stratigraphic thickness as well as lithofacies indicate that the stratigraphic section at Brownstone Falls was next to a persistent topographic high throughout Copper Harbor Conglomerate and Nonesuch Formation deposition which we refer to as the "Brownstone Highlands." Age constraints on the units come from Swanson-Hysell et al. (2019) and Hodgin et al. (2022).

in eukaryotes (Embley and Martin, 2006; Gold et al., 2017; Cohen and Kodner, 2021). However, traditional "body" fossils, molecular fossils derived from these sterols, and genomic molecular clock constraints give distinct perspectives on the timing of eukaryotic diversification and evolution (Cohen and Kodner, 2021). An additional consideration is recent proposals suggesting that stem-group eukaryotes could have thrived in diverse biogeochemical niches including those lacking oxygen (Porter et al., 2018; Porter, 2020). Studies directly connecting fossils and environmental conditions can be used to evaluate these hypotheses. Therefore, of particular interest in understanding the paleoenvironment and ecological setting of

this uniquely-preserved ancient lake system is characterizing its oxygen levels and the redox conditions of the sediment.

Iron mineralogy has the potential to give significant insights in this regard as the effects of oxygen on metabolic processes and abiotic chemistry lead to distinct mineral assemblages (Weibel and Friis, 2007). Rock magnetism provides mineral-specific insight and can constrain the abundance of iron oxide phases. Slotznick et al. (2018) demonstrated distinct iron oxide assemblages within two drill cores of the Nonesuch Formation in northern Wisconsin that can be categorized into three magnetic facies: a mixed assemblage of magnetite and hematite with relatively strong overall magnetization (Facies 2) that reflects the detrital input to the lake; an assemblage dominated by detrital and pigmentary hematite with weaker magnetization (Facies 3) that resulted from significant oxidation of the detrital magnetic minerals and reprecipitation of ferric oxides; and a facies with very weak magnetization carried by trace magnetite (Facies 1) that reflects reductive dissolution of iron oxides associated with anoxic conditions. These magnetic facies were interpreted to correspond with the deepening and progressive shallowing of the lake. Where the lithofacies are interpreted to indicate that the lake was deepest (Stewart and Mauk, 2017), the magnetic facies are indicative of anoxic conditions. At intermediate water depths, limited reductive/oxidative dissolution led to preservation of the detrital magnetic minerals. At shallow depths in the lake, nearly all the magnetite that was present in the detrital flux was oxidized to its most oxidized form of hematite.

In this contribution, we present new rock magnetic datasets from three outcrops sections (DG18, PRF18, PIR18) and two drill cores (PC-1, WPB-4) from northern Wisconsin and Michigan that can be integrated with the two drill cores studied in Slotznick et al. (2018) (DO-1, WC-9) to understand lateral variations. We use newly developed paleomagnetic data from one outcrop section (PRF18) to gain additional insight into magnetic mineralogy and provide refined constraints on the paleolatitude of deposition. New X-ray diffraction analyses on sister specimens to those targeted for rock magnetism give additional mineralogical insight for three cores (PC-1, DO-8, WC-9) and one outcrop section. Building on prior analyses (Wellman and Strother, 2015; Strother and Wellman, 2016, 2021), we document new palynological data from two outcrop sections and all four cores; samples which were often stratigraphically co-located with samples for rock magnetic analyses allowing data to be contextualized in terms of interpreted redox conditions.

Our newly described stratigraphic sections and field data document lateral variability in the thickness and lithofacies of the Nonesuch Formation across an outcrop belt in northern Wisconsin and the Upper Peninsula of Michigan. This lateral variability is associated with a paleotopographic high (described in Swanson-Hysell et al. (2019) and further elucidated here) that formed a shoreline of the lake. While previously studied cores record a single deepening and shallowing succession, outcrop successions close to this highlands region repeatedly transitioned into and out of the lake. We are therefore presented with the opportunity to investigate time-equivalent sediments that record distinct water depths of the lake. In contrast to more distal core and outcrop successions, there is minimal evidence for anoxic conditions in the nearshore successions. Rather, the magnetic mineral assemblages indicate oxic to low oxic conditions with progressive oxidation associated with shallowing as the lake transitioned back and forth between a lacustrine and fluvial environment.

GEOLOGIC SETTING

The Midcontinent Rift is a major intracratonic rift basin that developed in the interior of Laurentia (cratonic North America) and preserves a thick succession of mafic volcanic lava flows that erupted from ca. 1108 to 1084 million years ago (Green, 1983; Cannon et al., 1989; Swanson-Hysell et al., 2019; Woodruff et al., 2020). Along the south shore of Lake Superior, the rift volcanics are conformably overlain by the dominantly sedimentary strata of the Oronto Group (Figs. 1 and 2; Daniels (1982); Ojakangas et al. (2001)). The basal Oronto Group was deposited near the end of active extension and deposition continued as the basin thermally subsided prior to the rift undergoing contractional deformation in the later stages of the Grenvillian orogeny (Cannon, 1992; Hodgin et al., 2022).

The oldest formation of the Oronto Group is the Copper Harbor Conglomerate, which contains lava flows of the Lake Shore Traps on the Keweenaw Peninsula (Fig. 1). An andesitic flow within the Lake Shore Traps has a U-Pb date of 1085.57 ± 0.25/1.3 Ma (2σ analytical/analytical+decay constant uncertainty; Fairchild et al. (2017)) providing age constraints for this sedimentary sequence. The conglomerate, sandstone, and mudstone of the Copper Harbor Conglomerate were deposited within alluvial fan and fluvial plain environments (Daniels, 1982; Elmore, 1984). The conglomerate clasts are dominantly rift volcanics indicating the presence of rift highlands on the margins of the basin that sourced clastic debris into the subsiding rift basin (Daniels, 1982; Elmore, 1984). Paleocurrent data from the Copper Harbor Conglomerate indicate flow into the rift basin axis consistent with spatially restricted deposition within a basin where there was still significant topographic relief due to extension (Daniels, 1982). The Copper Harbor Conglomerate conformably transitions into the Nonesuch Formation which dominantly is comprised of siltstone to very fine sandstone with subordinate fine to medium sandstone (Daniels, 1982; Elmore et al., 1989; Stewart and Mauk, 2017). The Nonesuch Formation records both shallow water marginal lacustrine facies as well as deeper water facies and typically forms a deepening and then shallowing upward succession (Suszek, 1997; Elmore et al., 1989; Stewart and Mauk, 2017).

The Nonesuch Formation has been extensively studied with much of the research focused on economic-grade copper mineralization at the base of the formation in the White Pine region on the north limb of the Iron River syncline (Fig. 1; White and Wright (1954); Cannon et al. (1995)). This stratiform deposit is interpreted to have formed primarily due to a change in redox conditions when basinal fluids migrated from the oxidized Copper Harbor Conglomerate into the Nonesuch Formation (Mauk and Hieshima, 1992; Swenson et al., 2004). Portions of the Nonesuch Formation are relatively rich in organic carbon (Imbus et al., 1990, 1992) with petroleum seeps identified in the same region as copper mineralization (Mauk et al., 1992). In addition to sulfide, organic matter may have acted as a direct reductant enabling copper mineralization (Mauk et al., 1992). These organic-rich facies of the Nonesuch Formation were targeted for Re-Os geochronology which resulted in a preferred

date of 1078 ± 24 Ma (Cumming et al., 2013). While much early work focused in the White Pine Basin, recent stratigraphic and geochemical studies (Stewart and Mauk, 2017; Rico et al., 2019; Slotznick et al., 2018) have analyzed other sections of the Nonesuch Formation to the west within the Ashland syncline (Fig. 1) in order to understand development of this large water body as a window into a Mesoproterozoic environment.

The Nonesuch Formation conformably shallowed into the overlying fluvial lithofacies of the Freda Formation. The Freda Formation is a thick (>3 km) succession of fluvial channel and overbank deposits (Daniels, 1982). Notably for the purpose of interpreting the depositional context of the Nonesuch Formation, all of the units below and above the Nonesuch Formation were deposited in an emergent terrestrial setting. Consistently terrestrial depositional environments are recorded by interflow sedimentary rocks of the Portage Lake/Porcupine Volcanics as well as the Copper Harbor Conglomerate prior to the Nonesuch Formation deposition and by the Freda Formation afterwards. The observation that the Nonesuch Formation is ~100 to 300 m of strata within >13 km of demonstrably terrestrial volcanic and sedimentary deposits led Daniels (1982), Elmore et al. (1989) and Ojakangas et al. (2001) to conclude that the Nonesuch Formation was deposited in a lake and that it was unlikely that there was incursion of seawater far into Laurentia. Given that Laurentia was in the interior of supercontinent Rodinia, the Nonesuch was deposited >3,000 km from the open ocean. It is particularly difficult to understand how the basin would have been transiently below sea-level with marine deposition at the start of the post-rift thermal subsidence phase, but have then been a sustained fluvial environment for the tens of millions of years of deposition that followed during continued subsidence. Nevertheless, a renewed discussion on the depositional setting of the Nonesuch Formation has led to arguments of a marine environment based on interpretations of sedimentological and geochemical data (Jones et al., 2020; Stüeken et al., 2020). These researchers highlighted the presence of rare gypsum pseudomorphs and veins in the Copper Harbor Conglomerate and Nonesuch Formation as well as the presence of current ripples with varying paleocurrents which were argued to have formed through tidal currents (Jones et al., 2020; Stüeken et al., 2020). Additionally, Stüeken et al. (2020) use Sr/Ba values to argue for varying sulfate levels which they attribute to variable mixing between marine and lacustrine waters within an estuarine environment. They additionally document Mo enrichments in association with higher organic carbon and sulfur levels that they interpret to indicate a Mo-bearing water mass that is consistent with either a saline lake or seawater (Stüeken et al., 2020). Overall, it is extraordinarily challenging to differentiate between an ancient lake environment that periodically underwent evaporitic enrichment of solutes and a restricted marine environment in the Proterozoic Eon. Each line of geochemical and sedimentological evidence for a marine or estuarine environment is equivocal and dependent on assumptions, such as low sulfate levels in lacustrine environments, that may or may not be valid. We consider the stratigraphic, tectonic, and paleogeographic context to be most consistent with deposition within a lake and lacustrine terminology will be used here. Our interpretations in this regard are revisited in more detail in the discussion.

The outcrop belt of the Nonesuch Formation east of the Ashland syncline in northern Wisconsin into the Upper Peninsula of Michigan is part of a large-scale structure known as the Montreal River monocline (Cannon et al. (1993); Fig. 1). This structure developed as a result of far-field compressional effects of the Grenvillian orogeny and exhumed rocks along the Marenisco Fault (Cannon et al., 1993; Hodgin et al., 2022). The Nonesuch Formation was never deeply buried (Gallagher et al., 2017) and the overlying Freda Formation forms the structurally highest portion of the monocline (Fig. 1). As a result of monocline formation, the Nonesuch Formation is steeply dipping with dips of ~80° in the Brownstone Falls, Potato River and Montreal River exposures (Fig. 1). This steep tilt of the basal Oronto Group results in the bedrock geologic map approximating a cross-section at the time of Nonesuch deposition (Fig. 1). As can be seen in Figures 1 and 2, the Copper Harbor Conglomerate is in contact with progressively older volcanic rocks from the region of Presque Isle River and the Montreal River to the southwest towards Potato River and Brownstone Falls. In the area near Brownstone Falls, the Oronto Group is in contact with the oldest volcanics, the Kallander Creek Volcanics, which were locally dipping ~40° to the northeast when the Copper Harbor Conglomerate and Nonesuch Formations were deposited (Fig. 2; Swanson-Hysell et al. (2019)). This Brownstone Falls unconformity is therefore erosional and angular as a result of significant tilting and associated uplift on a rift flank prior to onlapping sedimentation of the Oronto Group. The stratigraphic thicknesses of the Copper Harbor Conglomerate and the Nonesuch Formation progressively thin towards Brownstone Falls in the southwest with lithofacies consistent with progressively shallower depths (Fig. 2). In addition to these lateral changes in stratigraphic thickness, lithofacies within both formations, discussed in more detail below, indicate deposition proximal to a paleotopographic high near Brownstone Falls that formed the shoreline of paleolake Nonesuch.

SEDIMENTOLOGIC AND STRATIGRAPHIC DATA WITH INTERPRETATION

Outcrop stratigraphic sections through the Nonesuch Formation were measured and samples collected at Brownstone Falls (DG18; 46.37629°N, 90.63977°W), Potato River Falls (PRF18; 46.46082°N, 90.52914°W), and Presque Isle River (PIR18; 46.66505°N, 89.93806°W). Additionally, a stratigraphic section was logged and samples collected from drill core PC-1 (46.6782°N, 89.9742°W; Fig. 1). This drill core was collected in 1959 by the Bear Creek Mining Company as part of an exploratory drilling campaign around the Presque Isle River; it was split and one half is stored at the Upper Peninsula Geological Repository. All sections span the entirety of the Nonesuch Formation (Figs. 3 and 4). Notably, the PIR18 measured section at Presque Isle River is at the southeast end of the Presque Isle syncline in order to span the entire Nonesuch Formation, in contrast to the partial section that is exposed at the Lake Superior shoreline (Jones et al., 2020). In addition, new data were collected from exposures of the Oronto Group along the Montreal River in order to constrain the thicknesses and lithofacies summarized in Figure 2.

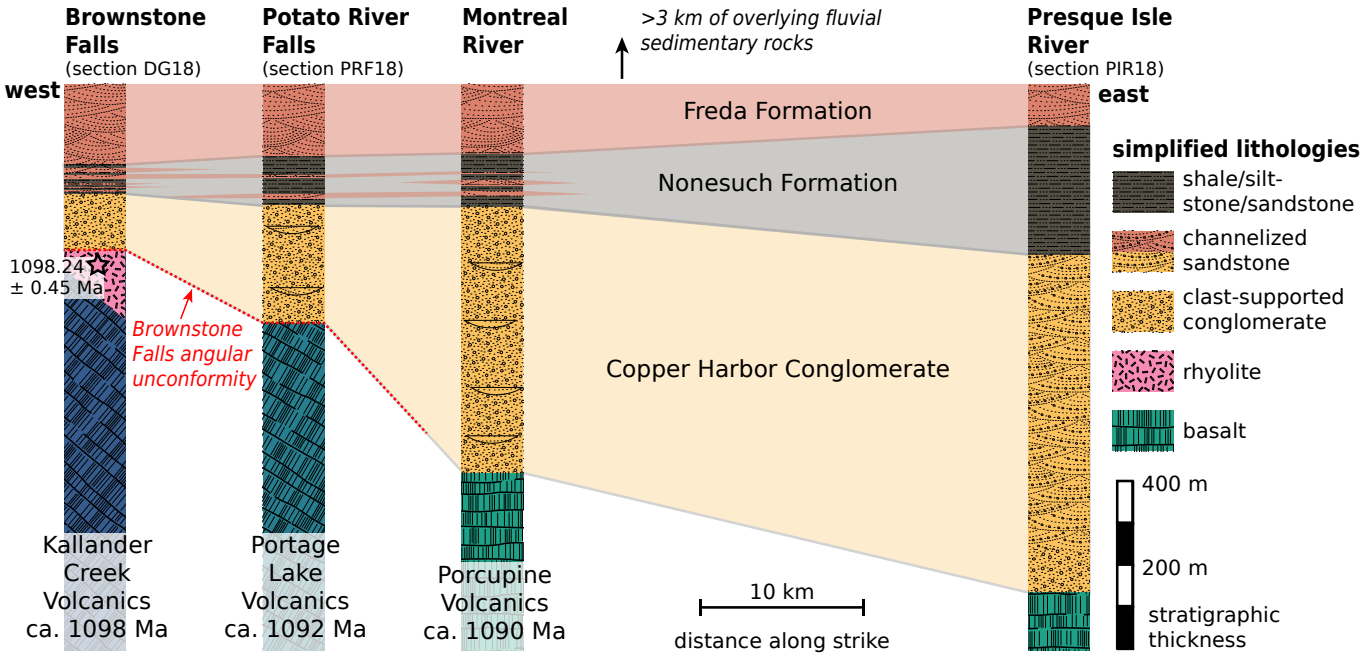

Figure 2: Summary of lithostratigraphy across the outcrop study region illustrating the change in formation thicknesses. The corresponding stratigraphic sections through the Nonesuch Formation shown in Figures 3 and 4 are written above each column. Where the Nonesuch Formation is thickest and consists of a single deepening and shallowing upward succession (at the Presque Isle River; section PIR18), the underlying Copper Harbor Conglomerate is also at its thickest. Both formations thin towards the paleotopographic high at Brownstone Falls where the DG18 section was measured (Fig. 1). Close to the paleotopographic high, the Nonesuch Formation records multiple transitions into and out of fluvial and lacustrine environments. These section locations near the paleotopographic high would have repeatedly been the shoreline while there was a continuously subaqueous environment to the east at the Presque Isle River section.

Close to the Brownstone Highlands where the Copper Harbor Conglomerate is thin (Fig. 2), the lithofacies of that formation are dominated by clast-supported pebble to boulder conglomerate of subrounded to rounded volcanic clasts (the conglomerate facies of Elmore (1984)). This dominantly cobble-sized, clast-supported lithofacies includes channelized lenses of sandstone that increase in frequency and thickness to the east from Brownstone Falls to the Montreal River. The conglomerate clasts are dominantly locally derived mafic and felsic volcanic rocks of the Midcontinent Rift. There is also a minor component of clasts from older Paleoproterozoic and Archean lithologies including banded iron formation. Overall, from Brownstone Falls to the Montreal River, the Copper Harbor Conglomerate is consistent with being deposited in stream-channel alluvial fans. At Presque Isle River, where the Copper Harbor further thickens (Fig. 2), the lower 80 meters of the Copper Harbor Conglomerate are composed of a similar conglomeratic lithofacies. However, the lithofacies then changes up section to be dominated by dune-scale (typical amplitude of ~20 cm) trough-cross-stratified medium sandstone with horizons of pebbles and with intervals both of current-rippled fine sandstone and clast-supported pebble to cobble conglomerate (with some small boulders). This lithofacies is indicative of deposition within a braided fluvial system wherein the trough-cross-stratified medium sandstone was deposited in channels, the conglomerate beds are remnants of gravel bars, and the fine sandstone beds were deposited as flood plain deposits (similar to the interpretations of Elmore (1984)). The lateral variability from dominant alluvial fan deposition at Brownstone Falls to that of a fluvial braidplain at the Presque Isle River, together with the thinning of the formation towards Brownstone Falls is consistent with a topographic highland associated with the Brownstone Falls angular unconformity (Fig. 2).

The typical stratigraphic succession of the Nonesuch Formation records a water deepening then shallowing (Elmore et al., 1989; Stewart and Mauk, 2017). This stratigraphic pattern is seen in the sections from the Presque Isle syncline (PC-1 core and PIR18 outcrop section; Figs. 1 and 3). The more extensive and three-dimensional exposure of the outcrop section better facilitated observations of sedimentary structures, but the same overall lithofacies succession was seen in both outcrop and core. The uppermost fluvial lithofacies of the Copper Harbor Conglomerate at the Presque Isle River comprises fine to coarse sandstone with dune-scale trough cross-stratification with channelized horizons of pebbles as well as interbeds of red-brown fine sandstone that can have mud-cracks, current ripples, and oscillatory ripples close to the contact with the Nonesuch Formation (Fig. 3). The trough cross-stratified sandstone can contain rip-up clasts of siltstone. This fluvial lithofacies abruptly transitions into grey siltstone to fine sandstone with symmetric wave ripples (at meter level 50 in PIR18; Fig. 3). In outcrop, there are nodules of native copper as well as disseminated copper mineralization in these lowest few meters of lacus-

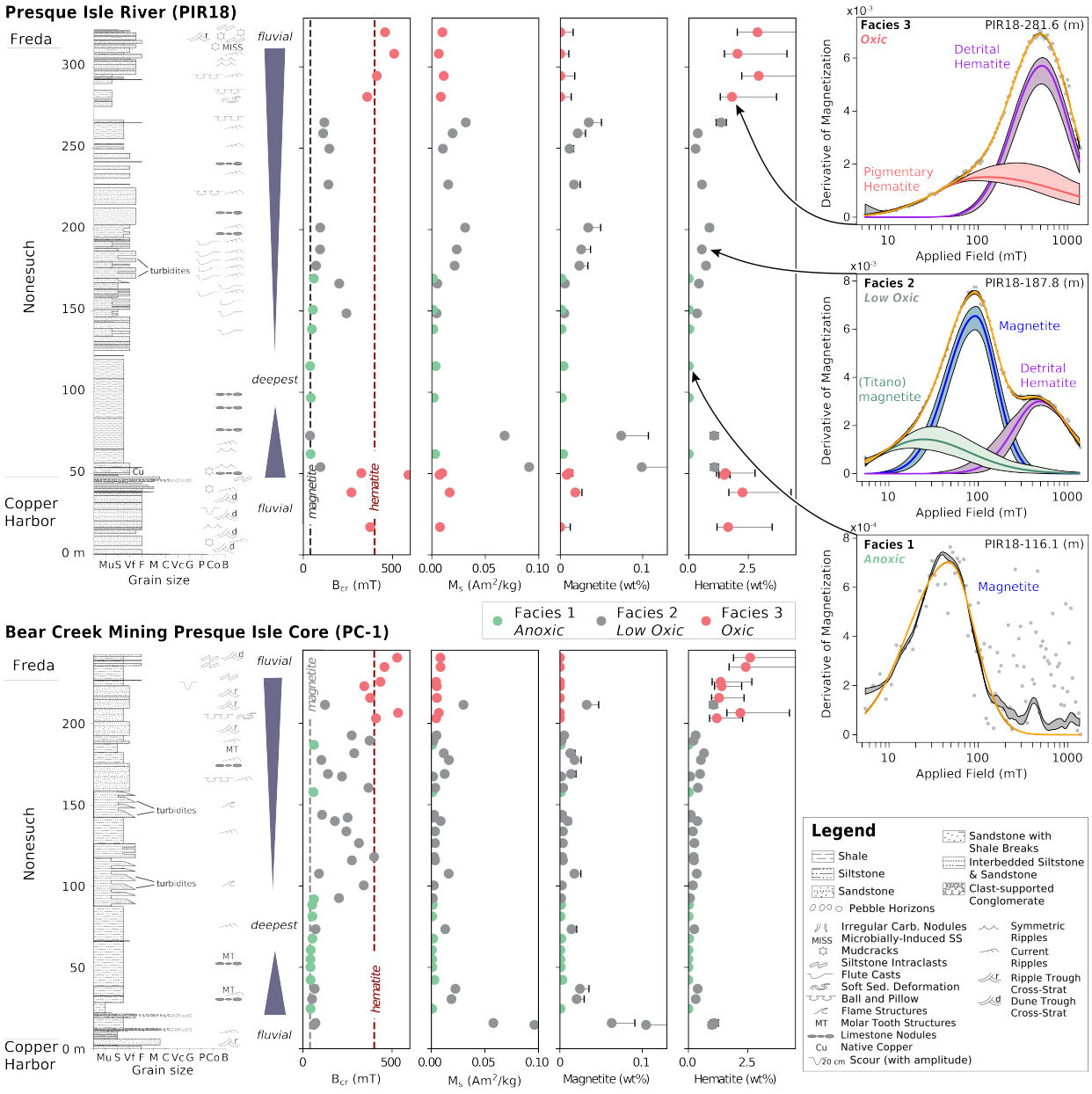

Figure 3: Stratigraphic sections with sedimentological observations, magnetic data, and facies interpretations from Presque Isle River and nearby drill core PC-1. These data constrain an abrupt deepening into the lake before progressive shallowing into marginal lacustrine facies and, eventually, into fluvial sediments as shown schematically with blue triangles. Magnetic parameters and quantification of magnetic minerals (see Appendix for methodology) delineate three magnetic facies linked to environmental conditions. Example representative coercivity spectra are shown for each of the three magnetic facies. Note the change in y-axis scale for the Facies 1 example due to an order of magnitude weaker magnetization. Abbreviations: B_{cr} = coercivity of remanence, M_s = saturation magnetization, SS = sedimentary structure, Cross-Strat = cross-stratification

trine sedimentary rocks — defining the base of the Nonesuch Formation. The evidence for current activity wanes up section as the succession is dominated by finely parallel-laminated dark-grey siltstone to very fine sandstone with minor carbonate (such as at meter level 100 in PIR18; Fig. 3; Fig. 5B) consistent with deposition at greater depth below wave base. Limestone nodules formed early within the sediment as evidenced by differential compaction around them. These nodules are indicative of an increase of alkalinity in pore water likely associated with anaerobic respiration of organic carbon (Bergmann et al., 2013). In the PC-1 core, molar tooth structures (small ptygmatically folded calcite microspar-filled veins) are also observed along horizons within the deeper water siltstone facies (Fig. 3 and 5H). These siltstones are followed by an interval of interbedded siltstone and very fine to fine sandstone. The outcrop exposure along the Presque Isle River en-

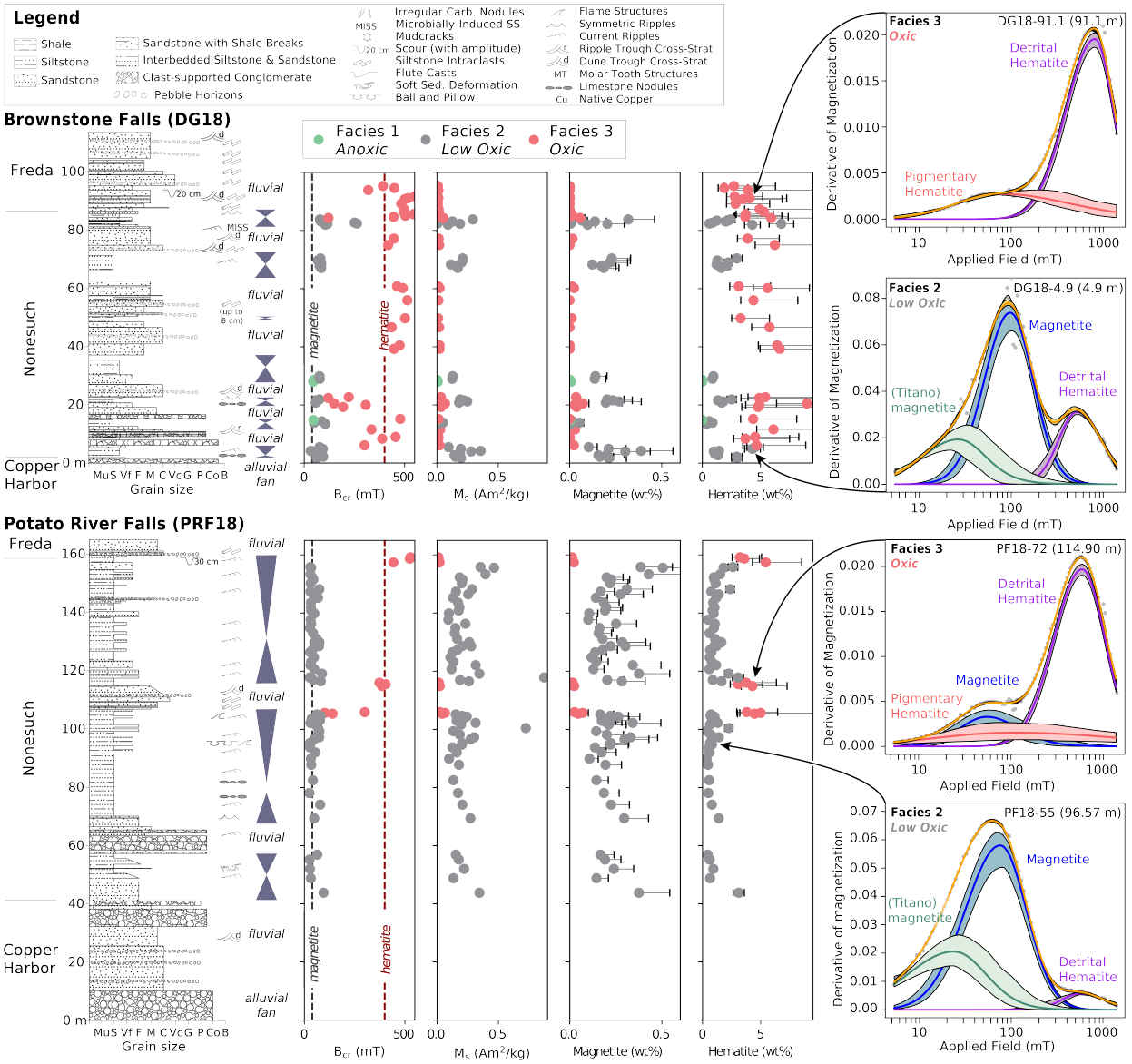

Figure 4: Stratigraphic observations, magnetic data, and facies interpretations from the Brownstone Falls (DG18) and Potato River Falls (PRF18) outcrop sections. These sections reveal several packages of lacustrine deposition separated by fluvial sediments. The interpretation of deepening and shallowing into and out of fluvial and lacustrine systems is shown with blue triangles. Magnetic parameters and absolute quantification of magnetic minerals allowed separation of samples into three magnetic facies linked to environmental conditions Example representative coercivity spectra are shown for each magnetic facies within each section. Note that the scales for M_s, magnetite (wt%), and hematite (wt%) are distinct than those in Figure 3. The two samples with highest M_s values in PRF18 are off-scale in the magnetite (wt%) plot. Abbreviations: B_{cr} = coercivity of remanence, M_s = saturation magnetization, SS = sedimentary structure, Cross-Strat = cross-stratification

ables the observation that the very fine to fine sandstone beds can have flute casts on their base and current ripples at their tops consistent with them being deposited as turbidites (Figs. 3 and 5E). The succession then continues with wavy-laminated siltstone to very fine sandstone with soft-sediment folds and ball-and-pillow structures. At meter level 299 in PIR18, there are symmetric ripples in very fine sandstone reflecting continued shallowing of the lake and the bottom sands experiencing oscillatory wave currents (Fig. 5F). Up-section, the siltstones are mud-cracked with crinkly bedding planes that likely are microbially-induced sedimentary structures (Noffke et al., 2001; Callow et al., 2011) (Fig. 5G) and transition into fluvial lithofacies, including trough cross-stratified ripples with siltstone rip-up clasts (including an observed mud-cracked clast) indicating that there were fluvial channels running over desiccated mudflats. Fluvial lithofacies are then sustained up-section throughout the overlying Freda Formation. Note that the conformable contact between the Nonesuch and the Freda Formation is variably defined given the transitional nature of the units. Prior work on drill cores from the Ashland syncline of Wiscon-

sin have defined the contact based on sustained red color (Munsell chroma of YR greater than 1; Stewart and Mauk (2017); Slotznick et al. (2018)). While this could be an effective definition, oscillatory wave ripples in the PIR18 section indicate that these red siltstones were deposited within standing water that was likely associated with a lacustrine environment (Fig. 5). An alternate definition for the base of the Freda Formation may be the presence of a sustained fluvial lithofacies assemblage including sedimentary structures such as current ripples with siltstone rip-up clasts which is the definition we use here (Figs. 3 and 4).

In contrast to the single deepening and shallowing upward succession observed in the Presque Isle syncline, further to the southwest at Potato River Falls (section PRF18), there are lacustrine lithofacies in three distinct stratigraphic packages separated by fluvial sandstone and conglomerate (Figs. 2 and 4). The dominant lithofacies within these lacustrine packages is finely laminated grey siltstone with sub-cm to cm-scale beds of very fine to fine sandstone that have wavy lamination and sediment-starved current ripples (Fig. 5C). The lamination in the siltstone to very fine sandstone is the result of mm-scale fining-upwards packages (Fig. 5D). Between these lacustrine packages are intervals of medium to very coarse sandstone with dune-scale trough cross-stratification and horizons of pebbles to cobbles and of red siltstone rip-up clasts (Fig. 4). These lithofacies are the same as in overlying fluvial sandstones of the Freda Formation. The lacustrine siltstones transition from grey to red brown (and to brick red in the uppermost package) prior to sharp erosional contacts that exhibit erosional scours associated with the base of the fluvial sediments (Fig. 4). As the stratigraphy returns to be siltstone-dominated above these sandstone beds, the siltstone transitions from red brown to brown to grey. A similar number of lacustrine to fluvial to lacustrine transitions are observed in the exposure of the Nonesuch Formation at the Montreal River (Fig. 2). The southwestern-most studied section at Brownstone Falls (section DG18; named after the Devil's Gate exposure of the Copper Harbor Conglomerate) records additional fluvial to lacustrine to fluvial transitions (Figs. 2 and 4). The fluvial interludes can be composed of clast-supported cobble conglomerate or of dune-scale trough cross-stratified sandstone with horizons of pebbles (Fig. 4). The lithofacies interpreted to be lacustrine are red brown to grey siltstone with horizons of symmetric wave ripples (Figs. 4 and 5). At Brownstone Falls, the Nonesuch Formation is the thinnest of the studied sections (as is the underlying Copper Harbor Conglomerate; Fig. 2) and much of the formation is the result of fluvial rather than lacustrine deposition. These observations are all consistent with the Brownstone Falls succession being the most proximal studied section, repeatedly becoming the lake margin due to its location on a persistent topographic high.

MAGNETIC AND X-RAY DIFFRACTION DATA WITH INTERPRETATION

IRON MINERALOGY

Rock magnetic analyses were performed on small rock chips from the outcrop stratigraphic sections and on samples from two drill cores of the Presque Isle Syncline, PC-1 located near Presque Isle River and WPB-4 located near the White Pine Mine and Big Iron River (Fig. 1). WPB-4 was collected in 1957 by the Bear Creek Mining Company as part of a large drilling campaign in the White Pine Basin beyond the then-active mine workings; the drill core was split and one half is stored at the Upper Peninsula Geological Repository. For each sample, room-temperature analyses were used to determine their coercivity (B_c), saturation magnetization (M_s), remanent saturation magnetization (M_{rs}), coercivity of remanence (B_{cr}), and coercivity spectra (Figs. 3 and 4). Coercivity parameters, B_c and B_{cr}, are the result of the aggregate behavior of the ferromagnetic minerals in a sample with coercivity spectra giving further insight into ferromagnetic phases and grain size distributions. Mineral identifications were made based on deconvolving of coercivity spectra and corroborated by low-temperature rock magnetic experiments and high-temperature thermal demagnetization. Low-temperature experiments cycle samples between 10 and 300 K and give insight due to diagnostic low-temperature magnetic mineral transitions (Figs. S1-S3). High-temperature thermal demagnetization data gives insight into mineralogy given the distinct unblocking temperatures of different ferromagnetic minerals as they approach their Néel/Curie temperatures. Petrography via optical microscopy and electron microscopy paired with energy dispersive X-ray spectroscopy (EDS) was used to corroborate grain-size interpretations, identify additional non-magnetic iron-bearing minerals, and provide additional context. Methodological details associated with these techniques are provided in the Appendix.

Four ferromagnetic components were identified in proximal sections at Brownstone Falls and Potato River Falls (Fig. 4) and at the more distal Presque Isle River section and core (Fig. 3): a) a low coercivity component (mean B_{cr} 10-45 mT) interpreted to be detrital titanomagnetite, maghemite, and/or coarse-grained magnetite, b) a mid-coercivity component (mean B_{cr} 28-127 mT) interpreted as detrital near-stoichiometric magnetite, c) a mid-high coercivity component (mean B_{cr} 106-408 mT) with a broadly dispersed peak interpreted as pigmentary hematite, d) a high coercivity component (mean B_{cr} 322-956 mT) interpreted as detrital hematite.

In the Presque Isle syncline, the remarkable similarity in iron mineralogy between core and outcrop highlights the excellent outcrop preservation of the Nonesuch Formation. Significant goethite (an iron oxyhydroxide often associated with surface weathering that can form at the expense of primary iron-bearing phases) was not identified in any of the outcrop samples including those containing pyrite. The studied surface rock exposures throughout the region consist of bedrock that has only recently been near the surface due to Pleistocene glacial and ongoing fluvial erosion. Glacial erosion is evident in striated rock exposures with ^{10}Be exposure dates constraining the timing of regional ice retreat from the Last Glacial Maximum to have occurred 13.2 ± 0.4 ka (Ullman et al., 2015). In the time since ice retreat ca. 13 ka, there has been significant river incision forming the river gorges in which the Nonesuch Formation is freshly exposed.

Magnetic data were used to group samples into three distinct magnetic facies. While facies match prior work (Slotznick et al., 2018), they were further developed here incorporating the new data from distinct parts of the basin. Facies 1 has very low

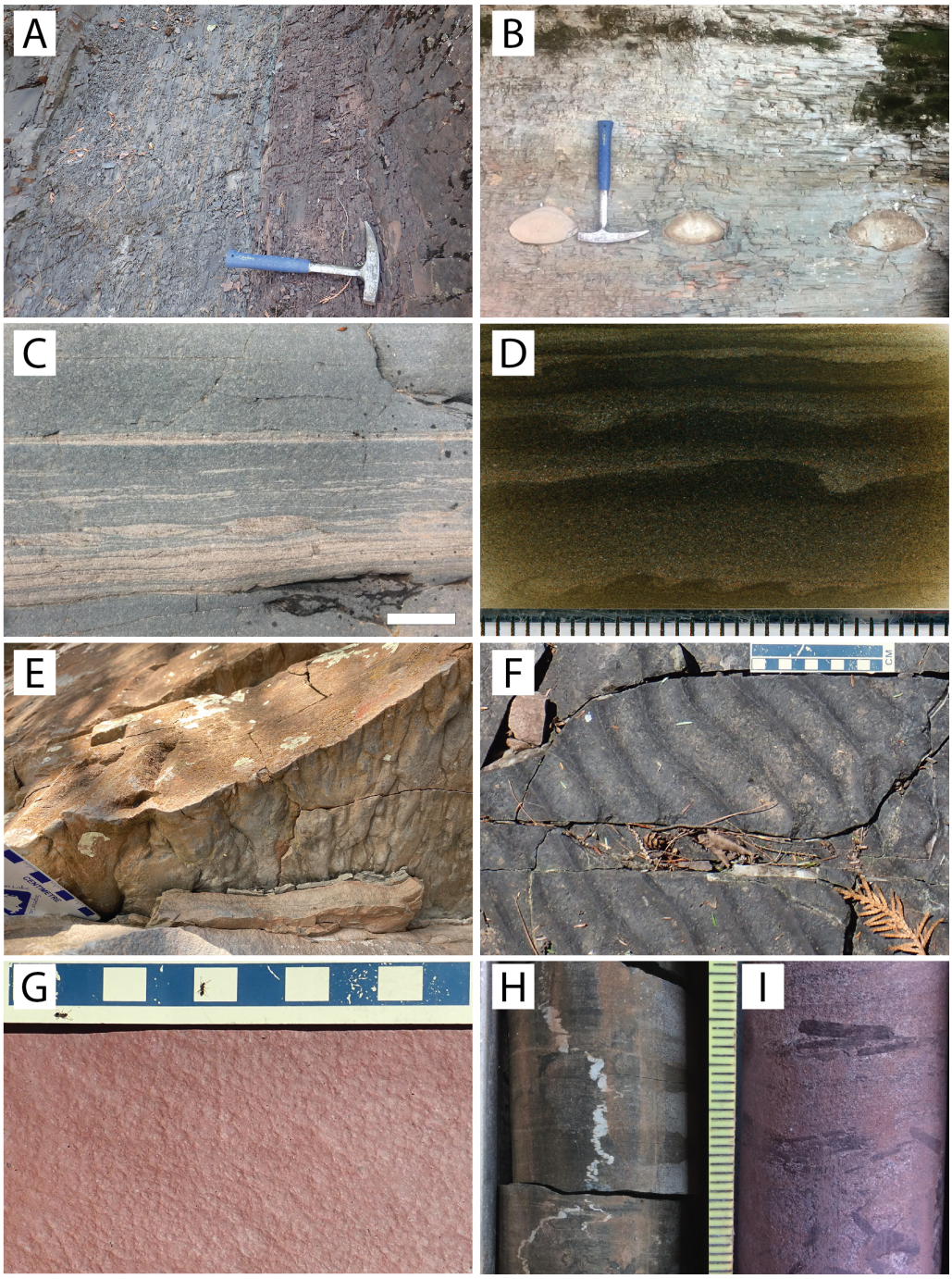

Figure 5: A) Color change from magnetic Facies 3 with pigmentary hematite on the right into magnetic Facies 2 on the left. The beds are steeply dipping with stratigraphic up to the left (82.0 m in section DG18; hammer is 33 cm long). B) Limestone nodules within siltstone of the Nonesuch Formation corresponding to magnetic Facies 1 (~94 m in section PIR18). Differential compaction of the siltstone bedding around the nodules indicates that they formed early within the sediment. C) Sediment-starved current ripples (tan colored) of very fine to fine sand within grey siltstone (between 70 and 100 m in section PRF18; white bar is 2 cm). D) Fining-upwards packages and dewatering structures, which give the siltstone to very fine sandstone a wavy lamination, seen in a thin section scan (78.1 m in section PRF18; ticks are 1 mm). E) Flute casts at the base of a turbidite (~170 m in section PIR18, scale bar is in centimeters). F) Oscillatory wave ripples in the uppermost Nonesuch Formation (298.5 m in section PIR18; scale bar rectangles are 1 cm). G) Crinkly texture on siltstone/very fine sandstone that could be the result of a microbial mat and therefore a microbially-induced sedimentary structure (307.7 m in section PIR18; scale bar rectangles are 1 cm). H) Molar tooth structure in PC-1 core (depth of 306 ft; ticks are 1 mm). I) Cross-stratified fluvial sandstone in PC-1 core with red siltstone rip-up clasts (depth of 133 ft; same scale as H with 1 mm ticks).

magnetization and a low coercivity; values of $B_{cr} < 100$ mT and $M_s < 0.01$ Am^2/kg were used as cutoffs for consistency across sections, with this facies being distinctly clustered (Fig. S4). Beyond these bulk values, unmixed spectra highlight that the single peak of magnetite preserved has a lower coercivity than in other facies (Fig. 3); this result is interpreted to be due to preferential dissolution of higher-coercivity iron oxide grains. Petrographic observations highlight an abundance of pyrite and a lack of visible iron-oxide phases with titanium oxides remaining (Fig. S5) similar to microscopy data in Slotznick et al. (2018). This mineral assemblage is interpreted to be due to reductive dissolution of detrital iron oxides in anoxic waters. These anoxic waters may have extended into the water column, but could have been restricted to sediment pore waters which were sulfidic based on the presence of diagenetic pyrite.

Facies 2 spans a range of coercivity and magnetization intensity due to different relative proportions of (titano)magnetite, maghemite, and hematite of varying grainsizes (Figs. 3, 4, S2, S4). Petrographic observations highlight that magnetite, titanomagnetite, and hematite co-exist in these samples including minerals with igneous origin (high-temperature oxyexsolution textures) that require them to be detrital particles (Fig. S5, Slotznick et al. (2018)). We therefore interpret that these iron oxides are detrital in origin and Facies 2 records the original mineralogy delivered fluvially from the catchment into the lake. Magnetite abundance can be particularly high in Facies 2 within the proximal sections, which is interpreted to reflect the close proximity of these samples to an actively eroding mafic volcanic highlands. Limited pyrite is observed petrographically in pore-spaces within some samples. The wide range of coercivity and magnetization in Facies 2 thus represents a mix of changes in detrital abundances (due to provenance, catchment size, distance from source, and/or hydrodynamic sorting) as well as diagenetic processes (reductive dissolution, maghemitization, etc.) albeit to a lesser extent than in the other facies. The increased diversity of this facies found due to the additional sections considered here also lends complexity to redox interpretations. However, the presence of detrital hematite and magnetite suggest that a) the samples existed in redox disequilibrium and b) conditions were not too reducing or oxidizing, and thus it represents a “middle" ground in environmental conditions — we will refer to it as low oxic to indicate this intermediate redox interpretation.

Data from Facies 3 samples have high coercivity of remanence and relatively low saturation magnetization compared to Facies 2 (Figs. 3, 4, S4) and are characterized based on the presence of pigmentary hematite. In coercivity spectra, pigmentary hematite can be difficult to identify in cases where magnetite is also present due to their overlapping coercivity distributions. For these samples, Munsell color data of YR with chroma greater than 1 was used as an indicator of pigmentary hematite and a guide for what components should be unmixed from the coercivity spectra (Table S2). In some cases, there is magnetite in Facies 3 in addition to detrital hematite, but at significantly lower concentrations than in Facies 2 (Figs. 4 and S3). We interpret this magnetite as being residual from a larger population that has been oxidized to hematite (an interpretation supported by microscopy; Fig. S5). The pigmentary hematite in Facies 3 would have formed from ferrihydrite precursors that are indicative of oxygenated pore-waters. Overall, the magnetic mineral assemblage of Facies 3 dominated by detrital and pigmentary hematite is interpreted to indicate an oxic water column and pore waters.

The exposure of the Nonesuch Formation at the Big Iron River has been the target of prior investigations (e.g. Symons et al. (2013); Spinks et al. (2014); Jones et al. (2020)) due to its accessibility and in some cases because researchers were interested in understanding processes associated with copper mineralization. The section is ~4 km from the historical underground workings of the White Pine Mine and has copper mineralization near the base. While economic copper mineralization is confined to the lower 5 meters of the Nonesuch Formation in the region, field observations of the Nonesuch Formation at Big Iron River suggest that fluids altered the iron mineralogy far upwards into the section. Color variations from bleached light tan to dark brown and dark purple as well as alternating green and purple were seen that are uncharacteristic of the Nonesuch Formation in regions without ore mineralization and are indicative of dissolution and reprecipitation of iron oxides. For this reason, we did not develop rock magnetic data from this section although we did develop rock magnetic data for core WPB-4 from the same Iron River syncline (Fig. S6). Caution is advised when applying geochemical proxies for paleoenvironment to samples from the White Pine region that experienced alteration from mineralizing fluids given this evidence for the secondary mobility of metals.

Bulk and Clay Mineralogy

X-ray diffraction (XRD) analyses were performed on a subset of samples from the Potato River Falls outcrop section and drill cores PC-1, WC-9, and DO-8 (the latter two having been analyzed with rock magnetism and iron speciation in Slotznick et al. (2018)). Each specimen (paired with a sample targeted for rock magnetic experiments) was analyzed with three different approaches: 1) bulk analyses across a wide 2θ range to identify major minerals, 2) high-angle region analyses for further constraining clay mineralogy, 3) clay peel analyses. Clay peel analyses physically separate and orient the clay minerals to provide a distinctive detailed analysis of them; for example, they are helpful for distinguishing relative amounts of muscovite versus illite (with interlayered smectite). For more detailed methodological information, see the Appendix section.

XRD analyses were not aimed at identifying iron oxides as the detection limits for iron oxides are much lower in magnetic analyses than for XRD. The goal of the XRD was to probe the clay mineralogy in more detail; in these fine-grained samples, clay minerals made up on average half of the sample (up to 71% based on bulk analyses) (Fig. S7). A wide variety of clay minerals were identified and record detrital, authigenic (water-column precipitation), and diagenetic (early or late post-depositional) processes. The excellent preservation of the Nonesuch Formation is highlighted by the fact that smectite is preserved (Fig. S8). During burial diagenesis of fine-grained siliciclastic sediments, dioctahedral smectite (an expandable clay) progressively transforms to non-expandable illite (Eberl and Hower, 1976). This transformation proceeds through the production of mixed-layer illite/smectite where the percentage of illite layers increases with both time and temperature until the reaction is complete and discrete illite is formed

(Bethke and Altaner, 1986). The temperature dependence of illitization has been investigated experimentally and derived by fitting kinetic equations to illite/smectite mineralogy in well-characterized sedimentary basins (Velde and Vasseur, 1992). Although smectite rarely occurs as a discrete phase in high-angle XRD analyses, almost all the clay peels analyzed show swelling or collapse in the XRD region dominated by interlayered illite/smectite clay. These behaviors are consistent with those reported by Price and McDowell (1993) whose estimates of smectite expandability from cores of the Nonesuch Formation led to proposed maximum burial temperatures of ~115°C in the Iron River syncline and ~140°C in the western portion of the Ashland syncline near DG18 and PRF18 (Fig. 1). Similar maximum temperature estimates of 125 to 155°C have been estimated through modeling solid-state reordering of clumped isotope data (Gallagher et al., 2017). These temperatures are consistent with burial by the ~3.3 km of Freda Formation that can be documented to overlay the Nonesuch Formation at the Wisconsin/Michigan border (this estimate is a minimum thickness as exposure disappears into Lake Superior, but is likely close to the true thickness). An average surface temperature of 20°C combined with 4 km burial in a geothermal gradient of ~30°C/km would lead to temperatures of 140°C.

To first order, the XRD data are fairly consistent within each stratigraphic section (Fig. S7, S8). This result is noteworthy due to the fact that there are interpreted variations in paleodepth (and redox state) within the samples of each individual location. There is much greater between-site variation than within-site variation in bulk mineralogy. For example, drill core DO-8 does not contain potassium feldspar (XRD determined a better fit with plagioclase feldspar) whereas all the other locations do contain potassium feldspar throughout their stratigraphy. Due to potassium feldspar's igneous origins, this result suggests distinct provenance of detrital minerals between sites. Notably, DO-8 also has the highest clay abundances in bulk analyses, perhaps due to clays being delivered via rivers from a deeply chemically-weathered source. However, alteration in the water-column or during diagenesis is difficult to rule out in this and many cases. For example, the Potato River Falls section contains the lowest amount of illite/smectite. In the detailed high-angle XRD analyses, Potato River Falls also is the only section to not contain berthierine or chamosite (Fig. S7). It is difficult to untangle whether these differences are the result of different provenance, water depth (as it is the shallowest section analyzed for XRD), or diagenesis (perhaps due to alteration of distinct detrital phases).

One unusual section-specific mineral identified in XRD is laumontite, a hydrated calcium-aluminium silicate in the zeolite group. It was only discovered at the Potato River Falls section and is limited to the upper two lacustrine packages where it can reach 7 wt%. EDS observations of three laumontite-bearing samples highlight pseudomorphic replacement of iron-titanium oxide detrital grains with calcium titanium silicates with minor aluminum, potentially a mixture of laumontite and titanite (Fig. S5). Laumontite formation is commonly associated with saline, alkaline lakes and is typically derived from alteration of volcanic glass. Zeolite formation rates increase with pH, which may have been facilitated in pore waters through rapid dissolution of the glassy substrate, and/or through interactions with alkaline lake water. As PRF18 is the shallowest of the regions analyzed for XRD, the presence of laumontite could indicate distinct chemical conditions in proximal lake sediments (i.e., more evaporation at the margins). However, the fact that it is only noted in some (not all) lacustrine packages suggests that laumonite's appearance could relate to distinct sediment grain provenance such as volcanic lithic fragments; magnetite data of high magnetite concentration at Potato River Falls are consistent with such a provenance. This provenance likely contributed to a detrital flux that was dissolved to form the laumontite within the lake sediment. Because laumontite is associated with distinctive provenance, zeolite formation was likely driven by local effects on pore water pH; its sporadic presence is unlikely to reflect a persistently alkaline water column.

Within stratigraphic sections, some overarching trends were also noted. In the three drill cores, WC-9, DO-8, and PC-1, kaolinite is more abundant in the shallowest samples of Facies 3 and absent from the deepest parts of the lake represented by Facies 1 (Fig. S7). Its presence at the base of PC-1 (during the deepening into Paleolake Nonesuch) as well as abundance throughout the Potato River Falls section suggests the abundance of kaolinite is connected to paleo-water depth. Highlighting this connection, in PC-1, a turbiditic sandstone (at 445.3 ft core-depth) contains more kaolinite than very fine sandstone immediately below the turbidite, representing background sedimentation at the same paleodepth. Another observation is that in all sites, chlorite is more abundant when the lake is deeper, with greater abundance in Facies 1 and 2 compared to Facies 3 (Fig. S7). The fact that this difference is noted in both the very shallow Potato River Falls section as well as in the three more distal drill cores suggests that it could be linked to redox conditions. Supporting this hypothesis, in the detailed high-angle XRD analyses, no berthierine/chamosite (Fe(II)-rich serpentine that transforms readily into the Fe-chlorite at temperatures $\geq$ 70°C (e.g. (Hornibrook, 1996; Jahren, 1989)) is identified in Facies 3. The possible redox link suggests chlorite is either detrital and being modified by lacustrine conditions or authigenic and forming in anoxic (pore) waters. SEM-EDS observations are consistent with both formation pathways. Samples from Facies 1 and Facies 2 contain small ($< 5\mu$m) iron-magnesium aluminosilicates associated with iron/titanium oxides suggesting authigenesis as well as larger ($\sim 20 - 100\mu$m) elongate grains including some with clear differential compaction that indicate a detrital origin (Fig. S5, Slotznick et al. (2018)).

PALEODIRECTIONAL DATA AND PALEOLATITUDE

Samples collected from the Potato River Falls section underwent high resolution thermal demagnetization to isolate paleomagnetic directions (see Appendix for detailed methods). Samples typically have a component removed in the initial thermal demagnetization steps (up to ~250°C) with a similar direction to the present local geomagnetic field (Fig. 6). After removal of this present local field overprint, thermal demagnetization data reveal distinct demagnetization behaviors linked to magnetic mineralogy and grain size. Siltstones to very fine sandstones in Facies 3 reveal two components that are similar but distinct in direction, with one component that progressively demagnetized up to ~660°C and the other that was removed over a narrower temperature range from 660°C to 696°C (Fig. 6). This demagnetization behavior is very similar to that observed in red

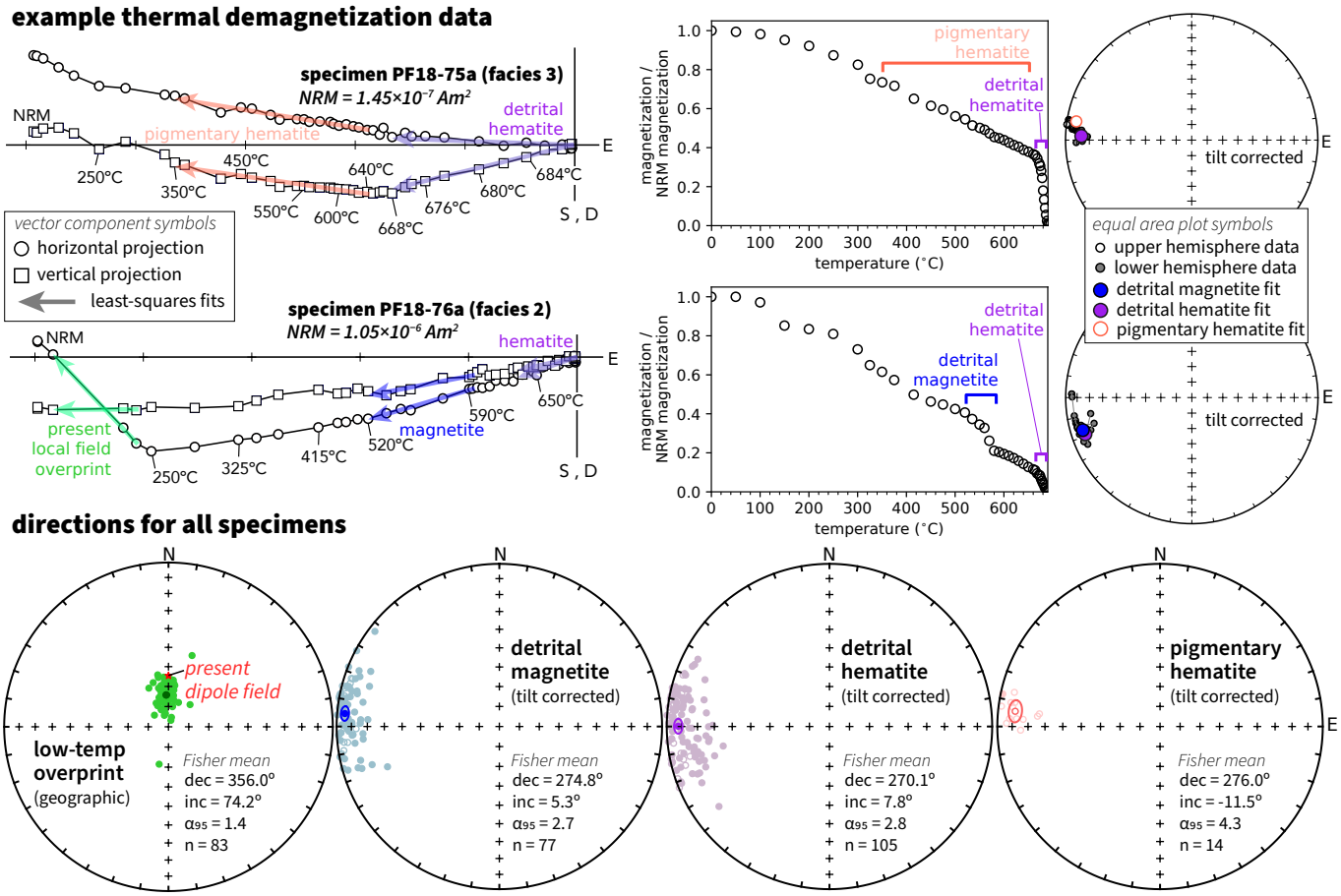

Figure 6: Thermal demagnetization paleomagnetic data for a specimen from Facies 3 (PF18-75a) and a specimen from Facies 2 (PF18-76a) shown as vector component plots, magnetic moment plots, and equal area plots. The Facies 3 data have a well-resolved high unblocking-temperature component (consistent with being held by detrital hematite) and a component that progressively unblocks up to ~660°C (consistent with being held by pigmentary hematite) that is in a distinct direction. The Facies 2 data reveal components held by magnetite and high unblocking temperature hematite that give similar directions — consistent with being primary detrital remanent magnetization held by the two different magnetic minerals. Directions for siltstone to very fine-sandstone specimens analyzed and fit with the different components are shown in the bottom panel of equal area plots. The low-temperature overprint has a similar direction to that of the present local field. The detrital magnetite and detrital hematite directions are both west and shallowly down. The pigmentary hematite direction has a similar but distinct direction from the detrital remanence directions. NRM = natural remanent magnetization.

siltstones of the overlying lower Freda Formation (Swanson-Hysell et al., 2019). In the Freda Formation, an intraclast conglomerate test revealed that the highest unblocking temperature steps were primary detrital remanent magnetization held by detrital hematite with grain sizes that are >400 nm (Swanson-Hysell et al., 2019). The remanence removed over a lower and more expansive temperature range was held by finer-grained pigmentary hematite that formed during burial likely from ferrihydrite/goethite precursors (Swanson-Hysell et al., 2019). The similarity in the thermal demagnetization behavior of the Nonesuch Formation Facies 3 data with the same magnetic facies in the lowermost Freda Formation support the highest unblocking temperature being detrital hematite with the distinct direction removed up to ~660°C being pigmentary hematite.

Siltstones to very fine sandstones from Facies 2 also have a magnetization component that unblocks at the highest thermal demagnetization steps (>660°C) consistent with it being held by detrital hematite, but lack a clear pigmentary hematite component (Fig. 6). Instead, the specimens typically have substantial magnetization unblock between ~520 and 580°C as evidenced through a "shoulder" in the thermal demagnetization spectra that is indicative of remanence held by magnetite (specimen PF18-76a in Fig. 6). The direction held by this magnetite is in the same direction as that of the detrital hematite (Fig. 6) as they pass a bootstrap statistical test for a common mean (Tauxe, 2010). This similarity in direction is consistent with the magnetite also being a primary detrital phase. Petrographic observations of (titano)magnetite and hematite grains reveal grain size, shape, and, in the case of magnetite, evidence for an ig-

neous origin that support this detrital interpretation (Fig. S5, Slotznick et al. (2018)).

While rock magnetic experiments and paleomagnetic analyses largely focused on siltstone and very fine sandstone, we also collected and developed data from fine to medium-grained sandstone within the Potato River Falls section. These sandstone samples revealed a distinct demagnetization behavior with remanence unblocking over a broad unblocking range up to 620°C (Fig. S10). This component has a distinct direction from the detrital hematite component and a similar direction to the secondary pigmentary hematite component of Facies 3 samples suggesting that it was also secondary and acquired during burial. These sandstones are lighter in color than the surrounding lithologies (tan rather than grey). With a lower clay mineral content and higher porosity, these sandstone beds would have been more susceptible to secondary fluid flow and remagnetization. We interpret this component as secondary and likely held by maghemite that formed during later diagenetic oxidative fluid flow that preferentially altered the more porous coarser sandstone lithologies in contrast to the siltstones which preserve primary detrital magnetite and hematite.

Henry et al. (1977) developed paleomagnetic data from samples of the Nonesuch Formation collected at sites located on Presque Isle River, Big Iron River, and the shoreline near Silver City. Specimen level data from that study are documented within Henry (1976) and are available in the MagIC database (`http://dx.doi.org/10.7288/V4/MAGIC/16450`). Henry et al. (1977) isolated both a component consistent with the detrital hematite component in terms of the temperature at which it unblocked as well as a component consistent with the pigmentary hematite component. These data are from Nonesuch strata that have quite different orientations than the data we have developed from Potato River Falls which enables a fold test. Both the primary detrital magnetization and the secondary pigmentary hematite magnetization pass the fold test. This result constrains both magnetizations to have been acquired prior to ca. 1050 to 990 Ma tilting associated with the Grenvillian orogeny (Cannon et al., 1993; Hodgin et al., 2022).

As the result of depositional processes and post-depositional compaction, detrital ferromagnetic minerals undergo inclination shallowing that results in remanent inclinations being shallower than the local geomagnetic field at the time of deposition (Tauxe and Kent, 2004). This shallowing can be expressed as $\tan(I_o) = f\tan(I_f)$ where I_o is the inclination that is observed for a specimen's magnetization, I_f is the inclination of the field in which the magnetization was acquired, and f is the flattening factor where 1 is unflattened and 0 is completely flattened. The elongation/inclination method can be applied to the detrital magnetization vectors wherein the shape of the distribution is compared to that expected to arise through secular variation associated with a statistical model of the geomagnetic field (Tauxe and Kent, 2004). This method provides an estimate of the flattening factor as well as associated uncertainty. Applied to the detrital hematite directions, it yields f=0.46 (with 95% confidence bounds of 0.71 to 0.38) and for the detrital magnetite directions, a value of f=0.38 (with 95% confidence bounds of 0.63 to 0.30). We combine the detrital magnetite and hematite directions to calculate a paleomagnetic pole and apply the method of Pierce et al. (2022) to incorporate the uncertainty on inclination shallowing (mean pole position shown in Fig. 7 and Table S1 with details on inclination correction in Fig. S11). The resultant mean pole is located at Plon=182.9°E, Plat=6.6°N with an elliptical uncertainty with a semi-angle of ζ_{95}=2.8° in the major axis direction of γ_2=[280.2°E, 27.6°N] and a semi-angle of η_{95}=2.0° in the minor axis direction of γ_3=[87.0°E, 41.6°N]. This inclination shallowing corrected pole position constrains the PRF18 section to have been at a paleolatitude of 7.1±2.8°N at the time of Nonesuch deposition (Fig. 7).

PALYNOLOGICAL DATA

Samples for palynological analyses were collected from drill cores DO-8, WC-9, PC-1, and WPB-4. Where possible, palynological samples were collected immediately adjacent to those used for magnetic analysis. Additional samples were collected from outcrop at the Potato River Falls section and at the Big Iron River (see Fig. 1). Palynological analyses were performed to make observations of the extracted, acid-insoluble organic fraction of a sedimentary rock that is structurally intact and visible with an optical microscope. The organic fraction is a combination of ancient cell walls (sometimes preserved with residual cell content), degraded structural organic matter, and amorphous organic matter which corresponds roughly to the kerogen fraction of a fine-grained siliciclastic rock. A provisional taxonomic assessment of the palynology was undertaken by scanning a single slide from each sample and noting the presence of provisional palynomorph taxa along with the palynofacies type based on the dominant form of preserved organic matter which varied between amorphous organic matter, structural organic fragments, and palynomorphs (complete vesicular organic-walled microfossils) (Fig. S12). See Appendix for slide preparation and microscopy methodological details. In Paleozoic and younger deposits, the biological affinities of organic-walled microfossils are well-known, and palynology can be used to further constraining a number of paleoecological and sedimentary depositional parameters such as terrestrial versus marine environment. In contrast, Precambrian palynology suffers from a high degree of uncertainty surrounding the biological assignment of even well-preserved organic-walled microfossils. Therefore, provisional palynomorph taxa corresponding to individual genera or species were grouped into the following categories: basic sphaeromorphs, striate cell walls, complex walls, discoids, other acritarchs, complex protists, elongates, multicellular forms, and prokaryotes (Fig. 8, Fig. S13).

THE PALYNOLOGICAL ASSEMBLAGE

The extracts reveal diverse palynological assemblages including up to 20 different provisional species in a single sample (Table S3). An overview description of the microfossils can be found in Strother and Wellman (2021); no new taxa are identified in this study. The assemblages are overwhelmingly dominated by sphaeromorph acritarchs (Fig. 8A), and within this group, most cells walls do not have sculptural elements on the largely smooth to granular walls. The assemblages also contain a wide range of more complex forms that have yet to be formally described (see broad categories above) as well as mul-

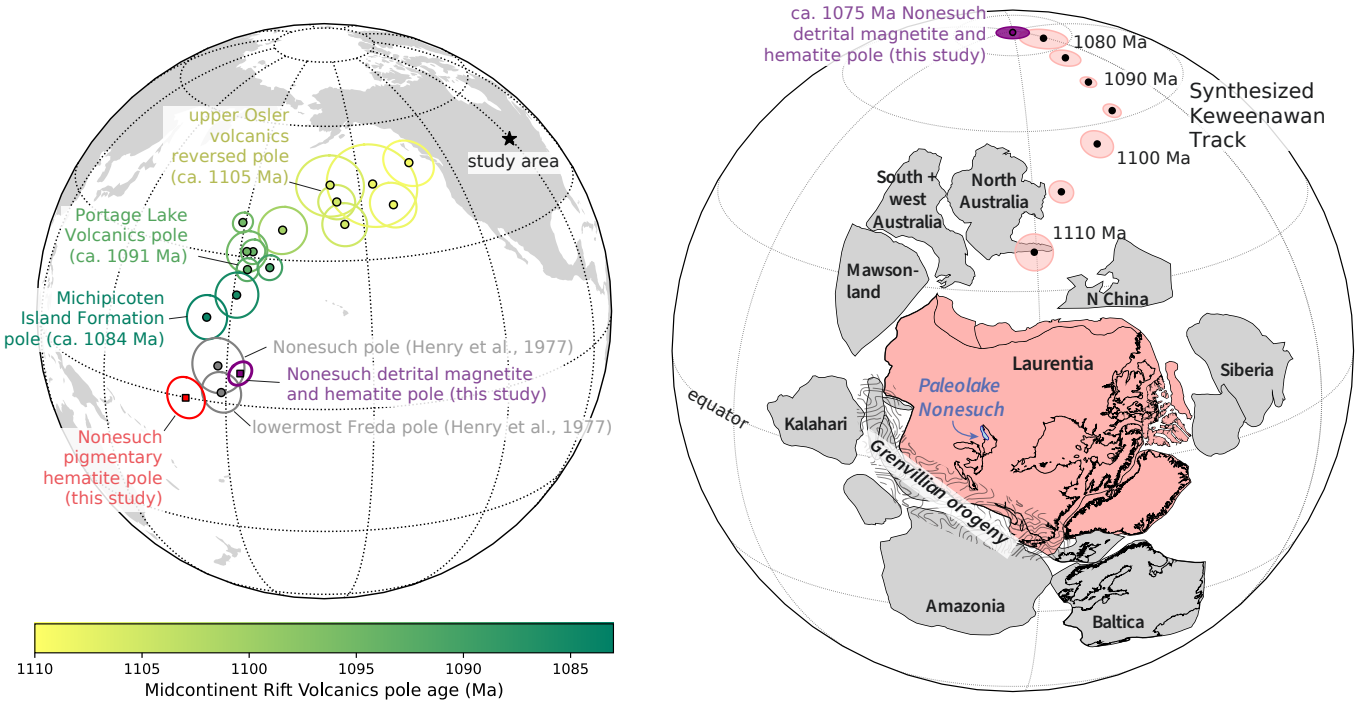

Figure 7: Left panel: Comparison of paleomagnetic poles from this work with those from the literature from the Midcontinent Rift (pole compilation from Swanson-Hysell (2021)). Note that our inclination-corrected Nonesuch detrital pole location agrees within uncertainty with that of Henry et al. (1977). The new detrital magnetization pole has an uncertainty that is smaller due to the increased number of samples and is elliptical in shape due to the incorporation of flattening factor uncertainty using the method of Pierce et al. (2022). The pigmentary hematite pole is in a distinct position and formed following deposition during burial after plate motion slowed due the Grenvillian Orogeny. Right panel: Paleogeography of Laurentia and associated continents during deposition of the Nonesuch Formation (modified from Swanson-Hysell et al. (2022)). Paleolake Nonesuch is shown as a minimum extent that encircles the outcrop exposures of the Nonesuch Formation in northern Wisconsin and Michigan. The lake was at a tropical latitude in the interior of Laurentia (cratonic North America) which was conjoined with other continents in the supercontinent Rodinia.

ticellular aggregates (Fig. 8D), although these are often far less abundant than the sphaeromorphs.

Although eukaryotic organic-walled microfossils dominate the assemblages in terms of abundance, most samples also contain some prokaryotes. The dominant prokaryotic taxon is *Eohalothece lacustrina* (Fig. 8H) – a presumed *Microcystis*-like cyanobacterial species (Strother and Wellman, 2016). Other prokaryotes occur in the form of individual empty sheaths that are assumed to be the remains of filamentous cyanobacteria. Trichomes, the cell filaments that secrete exopolymeric sheaths, are almost never found. Empty sheaths are assigned to the form taxon, *Siphonophycus* (Fig. 8G).

Sphaeromorphs represent the resistant walls or external cell coverings of unicellular organisms. However, the basic systematic affiliations of the dominant sphaeromorphs are not known; they are thought to be polyphyletic representing multiple different organisms (Cohen and Macdonald, 2015). One interpretation is that sphaeromorph acritarchs are ancestors belonging to stem groups of marine phytoplankton that exist today, such as chlorophyte and prasinophyte algae (Moczydłowska, 2015). More cautiously, we can infer that some sphaeromorphs in the Nonesuch assemblage may have been members of the green algae (Chlorophyceae) which today are freshwater in distribution.

The identification of more complex forms has a greater probability of success, although there is little certainty when making systematic assignments with unicellular fossils. One group that can be identified with higher confidence in the assemblage are the euglenids, including the photosynthetic Euglenophyceae. This interpretation is based on the recovery of forms that bear some morphological similarity to *Moyeria*, a Palaeozoic organic-walled microfossil belonging to the Euglenophyceae (Strother et al., 2020). These protists are covered by a proteinaceous pellicle that forms a series of discrete strips that wrap the cell in a distinctive helical pattern (Fig. 8F). They are not common in the Nonesuch assemblage (Strother and Wellman, 2021), but they have been identified in core PC-1 at depths of 305 ft (187 m in Fig. 3) and 564 ft (108 m in Fig. 3) and in core WC-9 at 1439 ft. Although our assignment of these forms to the Euglenophyceae is tentative, their confirmation would be significant. The evolutionary origins of species of the Euglenophyceae involved the endosymbiotic acquisition of a chl a+b chloroplast (Gibbs, 1978) derived from a free-living pyramimonadalean alga (Jackson et al., 2018). Confirmation

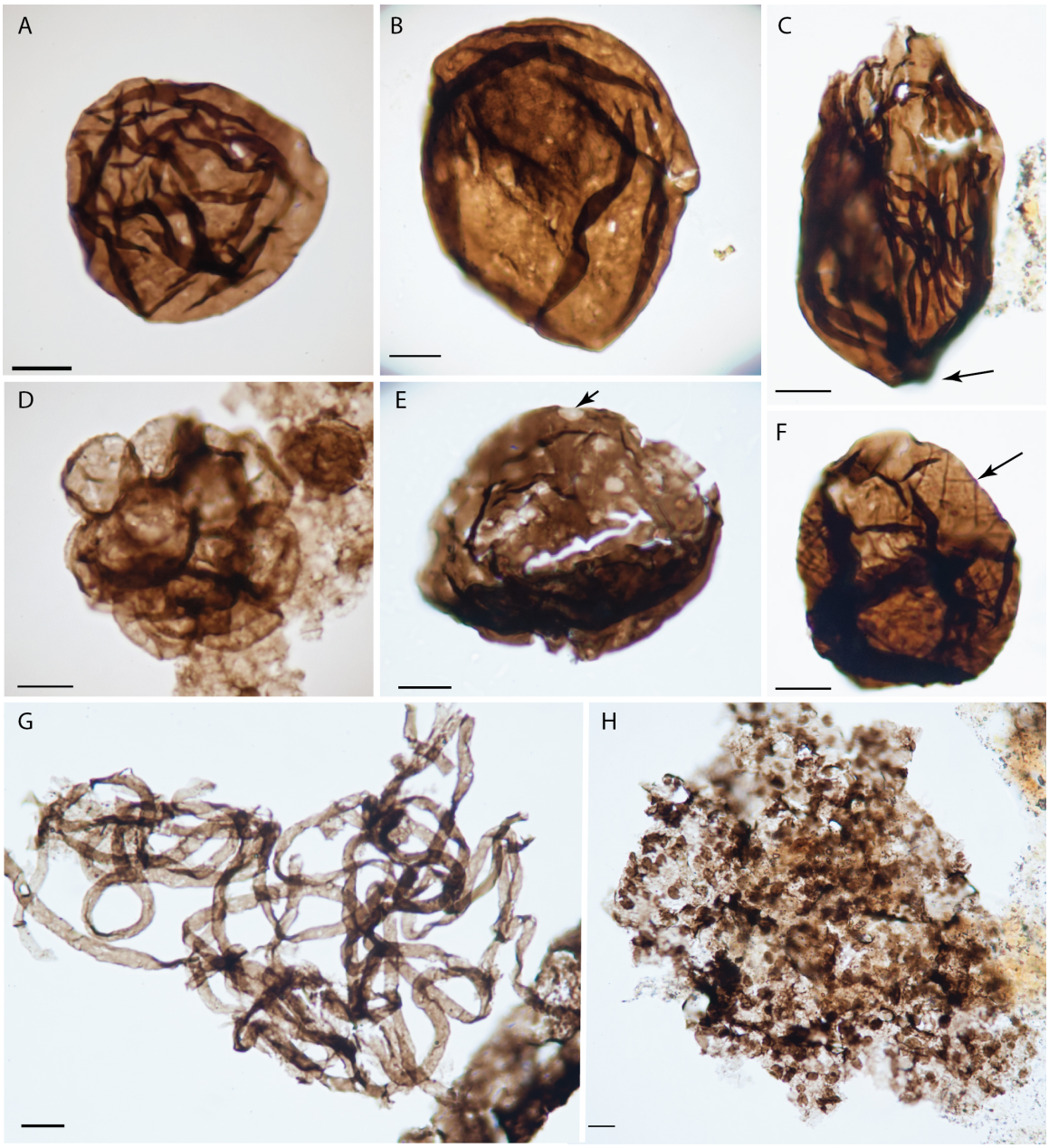

Figure 8: Examples of palynomorphs from the Nonesuch Formation mentioned in the text (all scale bars are 10 μm). A) *Leiosphaeridia crassa* from WC-9, 1292 ft (sample NON18-79) is a common sphaeromorph acritarch in the assemblage. Note the compression folds likely associated with flattening of an original spherical shape. B) *Valeria lophostriata* from WC-9, 1439 ft (sample NON18-64) is a sphaeromorph characterized by its wall pattern of fine concentric laminae, just barely visible here (see Strother and Wellman (2021) for close-up of striations in another specimens from the Nonesuch Formation). C) Unnamed elongate protist from the Big Iron River outcrop section (sample NON18-89) with a basal attachment scar (indicated with arrow) suggesting the presence of a stalk. This morphology suggests that the protist was a benthic organism. D) (Multi)cellular cluster, similar in morphology to the reproductive stages of living basal Holozoa, from DO-8, 1164.5 ft (sample NON18-14). E) Holes (one of which is indicated with arrow) in a microfossil from the Big Iron River outcrop section (sample NON18-114). These perforations could be the result of predation – possibly from chytrids. F) Possible euglenid characterized by helical striae that wrap around the wall (arrow) from the Big Iron River outcrop section (sample NON18-115). G) Mass of entangled *Siphonophycus*, a cyanobacterial sheath, that was likely derived from a microbial mat rip-up from the Big Iron River outcrop section (NON18-114). H) Cells of the planktonic cyanobacterium *Eohalothece lacustrina* from the Big Iron River outcrop section (sample NON18-111) embedded in organic material, that is potentially a remnant of a microbial mat.

of the presence of Euglenophyceae would provide evidence for the evolutionary existence of phagotrophy (eukaryivory) (Lax et al., 2021) and of eukaryotic photosynthesis in a chl a + b lineage. Euglenid microfossils would also be evidence of the presence of crown-group eukaryotes in these ca. 1075 Ma rocks (slightly older than the oft-cited first appearance of *Bangiomorpha* at 1047 +13/–17 Ma Gibson et al. (2018)).

Another potential systematic identification is the interpretation by Tang et al. (2020) that branching microfossils in the Nonesuch Formation are *Proterocladus* – interpreted as a multicellular benthic green algae. This interpretation is based on branching characteristics seen in two fragmentary specimens illustrated in Wellman and Strother (2015). An additional fragmentary specimen (Fig. 5c of Strother and Wellman (2021)), which occurs in core WPB-4 at a depth of 396 ft, also shows a singular branch that is even more similar to the well-preserved *Proterocladus* strengthening the interpretation of Tang et al. (2020). Following the interpretation of Tang et al. (2020) of *Proterocladus* as an epibenthic chlorophyte, these fossils from the Nonesuch would be the earliest known occurrence of crown group chlorophyte algae. This timing matches estimates from some molecular clocks for the emergence of chlorophytes by ca. 1090 Ma (Sánchez-Baracaldo et al., 2017).

Another example of complex morphology which may allow for systematic identification concerns the recently described likely holozoan, *Bicellum brasieri* (Strother et al., 2021). Although *B. brasieri* itself is not known from the Nonesuch Formation, there are multicellular clusters that look similar to multicellular reproductive stages found in the living ichthyosporean, *Creolimax fragrantissima* (Suga and Ruiz-Trillo, 2013, 2015) (Fig. 8D). Simple cell aggregates are typically placed into Synsphaeridium, but these undescribed forms in the Nonesuch Formation possess limited numbers of sub-reniform cells that form spheroidal clusters enclosed in a typically fragmented membrane, mimicking the morula-phase in some species of living ichthyosporeans. Today, holozoan species feed largely as osmotrophs, so confirmation of their presence in the Nonesuch Formation could be indicative of osmotrophy within the paleolake ecosystem.

Finally, there are perforations in cell walls that could be the result of early fungal (chytrid) activity (Fig. 8E). These holes occur when fungal haustorial filaments penetrate the host cell wall. Chytrid behavior has been documented for Devonian and recent times, but it has also been suggested to occur in the Nonesuch Formation (Berbee et al., 2020). Similar perforations have been noted in organic-walled microfossils within the approximately coeval Escape Rapids Formation of the Shaler Supergroup (1067 ± 14 Ma Re-Os date from Rainbird et al. (2020)) as well as younger formations within the group and similarly interpreted to represent selective predation, potentially by amoeba (Loron et al., 2018). If the perforations of the Nonesuch Formation are the result of predation, they would be amongst the oldest records of eukaryvory. This evidence in merely suggestive; however, along with other morphological indicators of various eukaryotes, it makes sense to consider that some level of trophic complexity existed in the benthic ecosystem of Paleolake Nonesuch.

PALEOECOLOGY INTERPRETATION

The limited ability to identify systematic affinities of problematic species adds considerable uncertainty when attempting to construct a picture of the ecology of Paleolake Nonesuch. Much of what we can infer is subject to change as additional fossil species are more critically identified. However, we are able to interpret a few basic aspects of the ecology.

Eohalothece lacustrina, originally described from the Nonesuch Formation as well as the Diabaig Formation (Torridon Group, Scotland; Strother and Wellman (2016)), is a planktonic cyanobacterium that may have had an ecology similar to that of modern-day *Microcystis aeruginosa*. This species forms large, sometimes clathrate colonies, which is a characteristic of planktonic life mode in extant cyanobacteria. However, single cells of *E. lacustrina* also appear embedded in organic groundmass associated with microbial mat-like features, such as embedded cyanobacterial sheaths (Fig. 8H). In modern-day lakes, *M. aeruginosa* overwinters in bottom sediments as individual cells which, upon perennation, develop into larger colonies capable of rising into the water column (Preston et al., 1980). This benthic-pelagic coupling does not occur in estuarine or marine settings, only in freshwater lakes (Verspagen et al., 2005). Because we have recovered both of these two ecotypes in the Nonesuch Formation sample, we infer that *E. lacustrina* was living in the water column, and may have dominated primary productivity in the Nonesuch trophic ecosystem. That dominance would have been shared with benthic cyanobacterial mats, although the evidence for such mats is based on inference from isolated sheath recovery. The scattered nature of sheath recovery may be the result of remobilization and transport of marginal, shoreline benthic microbial mats. Stromatolites interpreted as microbialites have been documented in the underlying Copper Harbor Conglomerate (Wilmeth et al., 2014; Hren and Sheldon, 2020), suggesting microbial mats were present in shallow-water environments. In a few instances, a small cluster of sheaths was observed — this might be considered evidence of microbial mat rip-ups (Fig. 8G), but such forms are not common.

Intriguingly, except for simple encystment, there is very little evidence of morphological adaptation associated with living in the water column. Spines and a range of elaborate cyst wall protrusions such as muri, crests, and flanges are absent. Even simple encystment, as characterized by a central body embedded within an enclosed vesicle, could equally be interpreted as an adaptation for living in benthic conditions. The planktonic component of eukaryotic algae living in lakes today appears to be missing at ca. 1075 Ma. This absence includes both coenocytic forms of hydrodictyacean chlorophytes and zygnematacean algal cysts. A conclusion could be that cyanobacteria dominated primary productivity in the water column and that benthic carbon fixation was from a combination of benthic eukaryotic algae and cyanobacteria. Overall, our paleoecological analyses provide a more robust understanding of the differences between modern and ancient lake ecosystems and further constrain hypotheses about the biology of eukaryotes in the late Mesoproterozoic.

DISCUSSION

Redox Data in Stratigraphic Context

Combining lithostratigraphy observations with iron mineralogical data allows us to confidently tie redox facies to lithofacies that give depth insight. In the Presque Isle River section (PIR18), sediments with oscillatory wave ripples within oxic Facies 3 are followed up-section by mudcracks that indicate subaqueous exposure associated with progressive shallowing. The paired sedimentological and redox data indicate that regions of shallow water were well-oxygenated with oxygen penetrating into sediment pore waters. The presence of likely microbially induced sedimentary structures in oxic Facies 3 gives tantalizing hints of photosynthetic microbial mats living in these shallow depths (Fig. 5G).

In the region near Brownstone Falls, the Nonesuch Formation was deposited atop a paleotopographic high associated with an angular unconformity that resulted from active rift development and rift flank uplift. In many sections of the Nonesuch Formation, there is a single deepening followed by a shallowing upward succession. However, the Brownstone Falls paleotopographic high was the margin of the lake. As a result, coeval shallow and deep environments are preserved in distinct sections (Fig. 9). In the shallow environments on the margin of the lake (DG18 and PRF18 sections), there are alternations between fluvial and lacustrine environments due to modulations in lake depth and extent. The rarity of the anoxic magnetic facies in the consistently shallow to emergent environments indicates that anoxic conditions that lead to the Facies 1 were dominantly restricted to greater depths in the lake (Fig. 9).

The ability to sample the transition into and out of Paleolake Nonesuch also emphasizes the connection between depth and magnetic facies with mirrored redox transitions (Fig. 9). Fine to very fine-grained sandstones of the Copper Harbor Conglomerate contain pigmentary hematite (Facies 3) as do shallow water lacustrine lithofacies within the Nonesuch Formation. In the PIR18 outcrop section and the PC-1 core, sediments deposited as the lake deepens are low-oxic Facies 2 prior to an extended interval of deeper water sediments which are anoxic Facies 1. The transition is then mirrored progressing back to low-oxic Facies 2 and then to oxic Facies 3 in the shallowest lacustrine sediments.

Pushing beyond drill cores to outcrop sections has expanded the geologic context of magnetic facies interpretations. These results corroborate the interpretation of Slotznick et al. (2018) that an oxycline existed in Paleolake Nonesuch. In Slotznick et al. (2018), Walther's Law was applied to interpret that the stratigraphic changes in interpreted redox are indicative of contemporaneous depth-dependent oxygen concentrations. With data from the outcrop sections in the present work, we are able to show that coeval shallow and deep portions of the lake had differing redox (Fig. 9), consistent with well-oxygenated shallow waters and a decrease of oxygen at depth associated with aerobic respiration of settling organic carbon.

Redox Data in Context of Timing of Mineral Formation

Our redox interpretations rely heavily on the fact that hematite represents the most oxidized form of iron that is stable over geologic time and is linked to environmental oxygen. The iron speciation redox proxy, a widely applied approach for interpreting ancient environments, includes hematite within the "highly reactive" pool due to hematite's reactivity toward sulfide. As a result, hematite-rich sedimentary rocks (like those in Facies 3) could be erroneously classified as being reflective of an anoxic environment if the technique was applied "blindly" without mineralogical or geologic context. Prior application of iron speciation to the Nonesuch Formation led to ambiguous redox interpretations (either ferruginous Cumming et al. (2013) or possibly anoxic and oxic Rico et al. (2019)) from samples that spanned all three of our magnetic facies. We hypothesize that iron speciation data from the Nonesuch Formation are hard to interpret as there is abundant highly reactive iron in an oxygenated system due to the nearby detrital source of hematite and abundant magnetite as well as pigmentary hematite formation within Facies 3. Compounding the issues associated with this geologic context, there is known mineralogical ambiguity in the operational chemical extractions; the oxalate extraction targets phases other than magnetite, hypothesized to be iron-rich clays by Slotznick et al. (2020). The Nonesuch Formation contains samples with abundant iron extracted by oxalate (up to 1.75 wt%). Similar to data within Slotznick et al. (2020), the high-angle XRD data from the Nonesuch Formation show a rough correlation with iron from this extraction and the Fe-bearing clays berthierine and chamosite (Fig. S9). As initial proxy calibrations were conducted without the oxalate extraction step (and in modern sediments lacking Fe(II)-bearing chlorites), we conclude that the iron speciation proxy yields limited insight when applied to these rocks.

In contrast, pairing mineralogic data with magnetic analyses provides a unique perspective on redox transformations within the lake, in the sediments and interstitial waters, and post-depositionally. In particular, paleodirectional data can give chronologic insight. Paleomagnetic data show magnetite and coarser-grained hematite to record the same direction. This hematite is confirmed to be a primary detrital remanence based on its reorientation in Facies 3 fluvial intraclasts from the lowermost Freda Formation just stratigraphically above the Nonesuch Formation (Swanson-Hysell et al., 2019). That the magnetization held by magnetite is indistinguishable from detrital hematite in siltstones and very fine sandstones (Fig. 6) supports it also being a primary detrital phase. The distribution of directions are consistent with them being primary and having undergone detrital inclination shallowing (Figs. 6 and S11). The paleomagnetic directions of the detrital magnetite and hematite lead to a paleomagnetic pole that is in an expected position along the apparent polar wander path from the Midcontinent Rift volcanics consistent with progressive movement of the rift basin following eruption of the ca. 1084 Ma Michipicoten Island Formation volcanics (Fig. 7).

In addition to detrital magnetite and hematite, the thermal demagnetization curves of some samples reveal the presence of lower unblocking temperature titanomagnetite that holds the same direction as the stoichiometric magnetite. The pres-

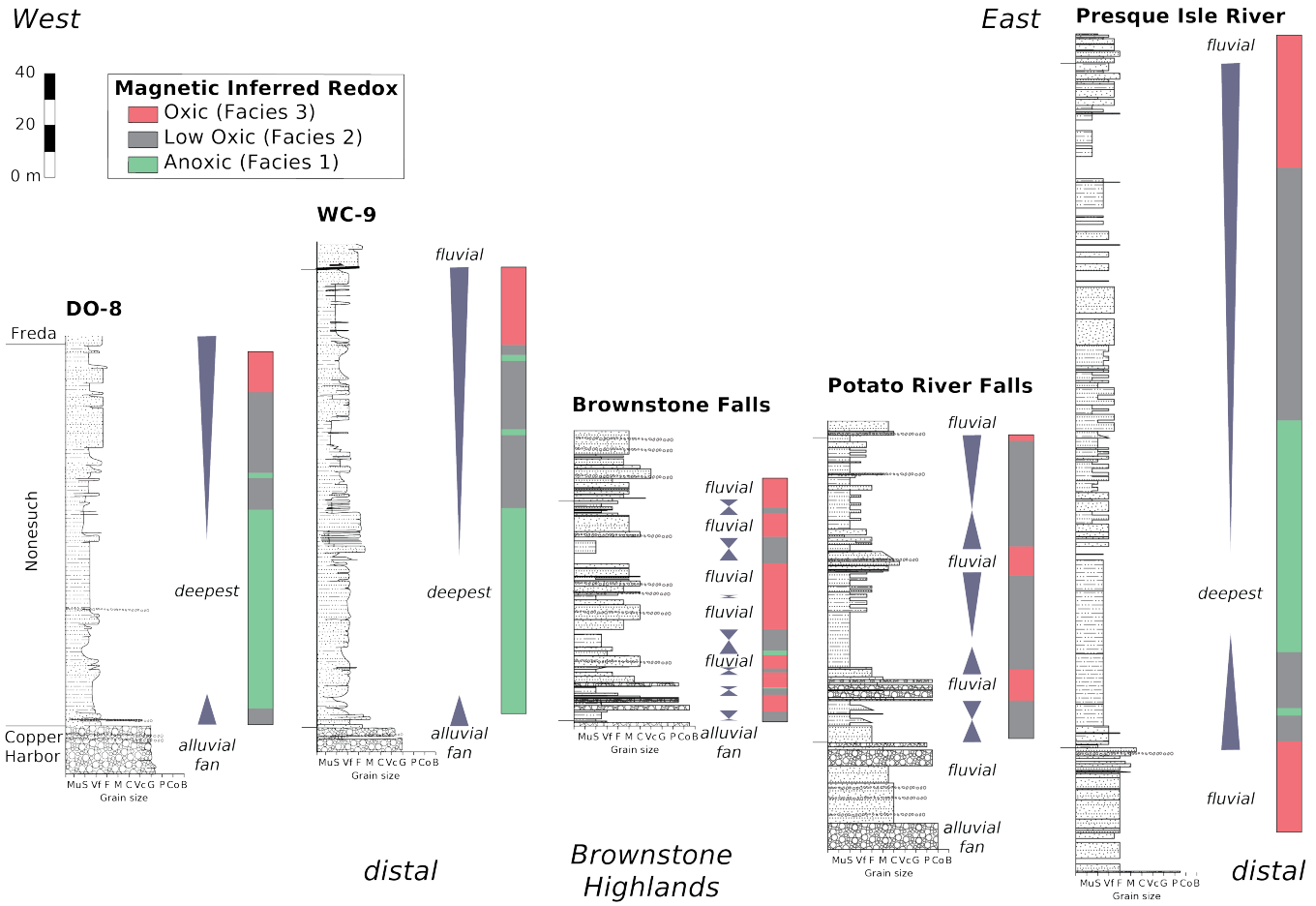

Figure 9: Redox interpretations across the Nonesuch Formation spanning drill cores and outcrop sections from Wisconsin to Michigan. The DO-8 and WC-9 drill cores are from the region of the Ashland syncline (Fig. 1, Slotznick et al. (2018)). It is likely that there was connectivity of Paleolake Nonesuch from this region to that of Presque Isle River through the main rift axis with the Brownstone Falls Highlands being associated with an intervening peninsula. The legend for lithologic symbols can be found in Fig. 4. Based on magnetic data and facies interpretations, all sections show similar trends where the deepest water sediments record anoxic conditions (Facies 1; green) and sediments deposited at shallow depths record oxic conditions (Facies 3; red) with a transitional facies between at intermediate depths (Facies 2; grey). Sections proximal to shore near the Brownstone Highlands do not have lithofacies indicating deep water deposition nor prolonged intervals of anoxic sediments; these redox interpretations are indicative of an oxycline within Paleolake Nonesuch.

ence of titanomagnetite is corroborated with petrographic and rock magnetic data and is expected in catchments eroding diverse volcanic and intrusive igneous rocks (Figs. S1-S2, S5, Slotznick et al. (2018)). Detrital (titano)magnetite and hematite can be present in quite high abundances within the Nonesuch Formation (Fig. 4) likely due to this proximity to mafic volcanics of the Midcontinent Rift on the rift margin. While the abundance of these detrital phases differs between sections, it remains relatively consistent within Facies 2 in each section (Figs. 3 and 4). As with the bulk XRD data, these data are indicative of consistent sediment provenance at each locale through the deposition of the Nonesuch Formation. The primary control on the abundance of magnetic minerals is instead associated with the redox-dependent magnetic facies: in Facies 1, both the detrital hematite and magnetite are dissolved preserving only trace magnetite; in Facies 3, the detrital magnetite is dominantly dissolved with the detrital hematite preserved.

Paleomagnetic data can also give insight into the timing of the formation of the pigmentary hematite that is characteristic of Facies 3. This hematite can be differentiated from the μm-scale detrital hematite as its finer grain size (<400 nm) leads to it thermally unblocking at lower temperatures (Fig. 6; Swanson-Hysell et al. (2019).) This paleomagnetic direction is similar, but distinct, from that held by the detrital phase with a slightly upwards inclination and a more northerly declination (Fig. 6). While the paleomagnetic analyses of siltstone rip-up clasts within Facies 3 siltstones in the lower Freda Formation revealed primary detrital hematite directions, they indicate that the finer-grained pigmentary hematite formed and acquired its magnetization direction after deposition (Swanson-Hysell et al., 2019). This pigmentary hematite component was

also isolated in paleomagnetic study of the Nonesuch Formation by Henry et al. (1977). Comparison of the directions between regions with different bedding tilts leads to a positive fold test described above. This result indicates that the pigmentary hematite magnetization must have formed during burial and prior to tilting of the strata, which occurred associated with far-field effects of the Grenvillian orogeny ca. 1050 to 980 Ma (Cannon et al., 1993; Hodgin et al., 2022). The distinct, but nearby, pole position of the pigmentary hematite relative to the detrital pole is consistent with it forming during burial after ca. 1075 Ma deposition and prior to ca. 1050 Ma tilting.

Pigmentary hematite forms from the transformation of metastable nanocrystalline ferrihydrite, which precipitates in oxidized water and sediments (Jiang et al., 2015, 2018; Gutiérrez et al., 2016). Ferrihydrite is the dominant Fe(III) oxide found in modern oxic sediments (Chen et al., 2017) and is experimentally constrained to transform to hematite through pathways that can include an intermediary of nanogoethite (Das et al., 2010). That this transformation is constrained paleomagnetically to have occurred during burial in the basin is consistent with observations that moderate heating during burial (~60-75°C) results in the transformation of these metastable phases, including goethite, to stable pigmentary hematite (Weibel and Grobety, 1999). Therefore, while it is secondary, pigmentary hematite is an indicator of pore-water oxygenation.

PALEOGEOGRAPHY AND PALEOENVIRONMENT OF THE NONESUCH LAGERSTÄTTE

Depositional Setting

The paleolatitudinal constraints from the primary detrital magnetization highlight that the organisms preserved within the Nonesuch Formation inhabited a tropical basin at 7.1±2.8°. This latitude is similar to that in modern-day East African Rift lakes. Significant sedimentary-lithofacies variability exist in East African Rift lakes on the scale of tens of kilometers (Rosendahl and Livingstone, 1983) as is observed in the Nonesuch Formation (Fig. 2). Additionally, intracontinental rift systems can be quite responsive to changes in regional hydroclimate which can lead to frequent water level variations such as those observed in the East African Rift (Scholz et al., 1990) interpreted to have varied on ~20 kyr timescales (Deino et al., 2006; Ashley, 2007). Lake-level variations consistent with such an intracontinental tropical rift environment are recorded in the Nonesuch Formation in the sections proximal to the Brownstone Highlands (Figs. 2 and 4). Similar to the modern East African Rift, other contemporaneous lakes may have existed within the rift system leading to deposition of shale and siltstone within the Midcontinent Rift in Iowa that has been correlated with the Nonesuch Formation (Anderson, 1997).

As introduced above, there are long-standing discussions in the literature of a non-marine or marine origin for the Nonesuch Formation (e.g. Hise and Leith (1911)). Researchers have long pointed out that Nonesuch Formation lithofacies are consistent with many features found in lacustrine systems while also acknowledging the difficulty in differentiating between a lacustrine and marine origin (Daniels, 1982; Elmore et al., 1989). A differing perspective was put forward in the work of Jones et al. (2020) where they documented lithofacies and sedimentary structures within the Nonesuch Formation and argued for deposition within a shallow marine embayment. Given that the majority of sedimentary features are equivocal with regards to a lacustrine or marine setting, Jones et al. (2020) place particular emphasis on the interpreted presence of large-scale hummocky cross-stratification and "herring-bone" ripples. We find the interpretation of these sedimentary features to be unconvincing. The ripple cross lamination in the Nonesuch Formation reported as being "herring-bone" (shown in Figure 14 of Jones et al. (2020)) are similar to the ripples shown in Figure 5C) and do not meet the definition of herringbone cross-bedding in which foresets in successive sets are going in opposite directions (Allaby, 2020). While it is the case that these current ripples are not unidirectional, directional variability does not necessitate a tidal influence. The only interval where Jones et al. (2020) report large-scale hummocky cross-stratification is in their Presque Isle section within the uppermost Nonesuch Formation four meters below the contact with the Freda Formation. In this portion of the Nonesuch Formation at that locality, there are abundant sedimentary structures indicating a shallow water environment with periodic exposure including asymmetric current ripples, symmetric ripples, and mudcracks. It is difficult to reconcile this facies association (the marginal lake facies association of Elmore et al. (1989)) with the interpretation of large-scale combined flow generating hummocky cross-stratification. We have not observed the specific bedform depicted in Figure 15 of Jones et al. (2020) as an example of meter-scale hummocky cross-stratification; however, that portion of the stratigraphy does contain some rare ~40 cm amplitude stratification due to migrating dunes similar to sand channels, which are interpreted as deltaic deposits in the White Pine region (Daniels, 1982), suggesting that alternate origins are possible.

Another line of evidence put forward by Jones et al. (2020) and by Stüeken et al. (2020) in favor of a marine depositional environment is the presence of sparse sulfate evaporites in the Copper Harbor Conglomerate and Nonesuch Formation. However, saline waters and evaporite deposits are common within tropical East African Rift lakes (Eugster, 1980; Scholz et al., 1990). Closed basins within volcanic provinces often have high sulfate concentrations that can lead to sulfate-rich brines upon evaporative concentration (Risacher et al., 2003). Within the Midcontinent Rift, there is substantial magmatic sulfide mineralization in rift units (Woodruff et al., 2020) and the Nonesuch basin catchment would have also included sulfide-rich Paleoproterozoic metasedimentary rocks (Ojakangas, 1994). This geologic context indicates that there would have been significant sulfate delivered to the Nonesuch water body following subaerial sulfide oxidation. The presence of significant sulfate is indicated by the evidence for microbial sulfate reduction and the formation of pyrite within anoxic Facies 1 of the Nonesuch Formation (Fig. S5, Slotznick et al. (2018)). An interpretation that the presence of sulfate, as indicated by gypsum or the Sr/Ba proxy, is indicative of marine waters (e.g. Jones et al. (2020); Stüeken et al. (2020)) relies on an assumption that lakes have low sulfate. This assumption is likely erroneous in the context of a lake that would have developed within the Midcontinent Rift.

The more prevalent interpretation in the literature that the Nonesuch Formation was deposited in a lacustrine environ-

ment comes from researchers who have studied the formation in the broader context of the rift basin and the Oronto Group (Ojakangas and Morey, 1982; Daniels, 1982; Elmore et al., 1989; Ojakangas et al., 2001). The broader stratigraphic context and considerations of basin development make it difficult to envision the basin at sea level at the time of Nonesuch Formation deposition. Appreciable subsidence occurred following deposition of the Nonesuch Formation leading to the continuous fluvial deposition of the >3 km Freda Formation (Daniels, 1982). If the Nonesuch was deposited at a low enough elevation such that there could be a marine incursion, the expectation would be that the Freda Formation would have been deposited at or below sea level as subsidence continued. Instead of having evidence of marine incursion or lithofacies that would be indicative of an isolated endorheic (internally-drained) basin below sea level, the Freda Formation consists of fluvial channel and flood plain deposits consistent with a terrestrial exorheic fluvial system (Daniels, 1982). The broader paleogeographic context places the Nonesuch water body in the interior of the supercontinent Rodinia (Fig. 7). While there can be incursions of marine waters far into the interior of continents, the stratigraphic context of the Nonesuch Formation is ~100 to 300 m of strata with >10 km of terrestrial volcanic and sedimentary deposits below and >3 km of terrestrial sedimentary deposits above. As in the East African rift system, there was an interval of plateau volcanism followed by rift basin development in the Midcontinent Rift (Woodruff et al., 2020). Similar to modern-day East African Rift lakes, the Nonesuch Formation was likely deposited within an endorheic basin at an elevation well above sea level. Subsequent changes in sedimentation and the hydrologic regime led to the above-sea-level fluvial system that deposited the Freda Formation as regional thermal subsidence continued.

Redox Context of the Microfossils

The presence of an oxycline within Paleolake Nonesuch presents an opportunity to evaluate the ambient redox environment and oxygen levels experienced by contemporary life and associated with microfossil preservation. Sediments integrate records across water depths; thus with sufficient preservation, one would expect to find planktonic organisms inhabiting shallow oxygenated waters at all water depths, but could potentially isolate distinct organisms inhabiting other water depths depending on the redox conditions (as described in Porter et al. (2018).) For Paleolake Nonesuch, there is an opportunity to examine the correspondence between the palynological data (preservation, abundance and diversity) with redox-based facies patterns as well as inferences about relative shoreline proximity and water depth.

Three palynological samples were collected from oxic Facies 3 — they were processed using the same methods as other samples and determined to be barren of organic matter or microfossils (Fig. 10). These barren samples indicate that there was degradation of the microfossil assemblage associated with the oxic conditions of Facies 3. In contrast, microfossils are found in both low-oxic Facies 2 and anoxic Facies 1. However, there are significant differences in the types of organic matter and microfossil abundance/diversity between these facies with the Nonesuch Lagerstätte primarily preserved in sediments of the low-oxic Facies 2 (Fig. 10). Samples from Facies 1 often yield amorphous organic matter or poorly preserved palynomorphs that cannot be identified (Fig. 10, S13). In contrast, samples from Facies 2 are much more likely to be microfossil-rich and to contain a more diverse assemblage of microfossils (Fig. 10). Given that depth is strongly connected to redox in Paleolake Nonesuch, it is possible that the deepest parts of the lake received fewer preservable organic remains. However, short intervals of Facies 1 in larger packages of Facies 2 have poor microfossil preservation and vice versa with Facies 2 having better microfossil preservation; this result suggests that redox is a major control. Both clay composition and organic carbon content associated with these redox facies could play a role in this preservational difference. Facies 2 is the only facies containing both kaolinite and berthierine/chamosite; these clay minerals have been indicated as important in soft-tissue preservation of animal Lagerstätten (Anderson et al., 2018, 2021) and could potentially play a role in enhanced preservation of organic-walled microfossils as well. In terms of organic carbon content, recent analysis of a compilation of data from Precambrian shales elucidate a trend wherein samples that best preserve organic-walled microfossils are those with relatively low total organic carbon (< 0.66 wt%) (Woltz et al., 2020). Total organic carbon values vary greatly across the Nonesuch and were not analyzed in these paired samples, but tend to be higher in the deeper lithofacies that are predominantly magnetic Facies 1 where organic matter is preserved, but microfossils are more degraded (Imbus et al., 1992; Slotznick et al., 2018). The cause of this relationship to organic carbon is hypothesized to be related to microbial degradation where reactive transport of extracellular enzymes are more likely to contact organic matter and further stimulate microbial activity (Rothman and Forney, 2007; van Nugteren et al., 2009) with possible additive factors from interactions of organic matter with clays and/or sedimentation rate affecting time in zones of microbial activity (Woltz et al., 2020).

Where preserved, there are similar palynological assemblages throughout Facies 1 and 2 of PC-1, DO-8, and WC-9 indicating that there is not a strong depth dependence (Fig. S13). Prokaryotes interpreted to be photosynthetic with both planktonic and benthic modes are found equally in sediment deposited in shallow and deeper water(Fig. S13); this is contrary to expectations based on photosynthetic requirements of light-filled waters. There is some relationship with depth as microbial mat fragments were only found in the upper half of the Nonesuch Formation in the WC-9 core (>1432 ft) indicating that at this location photosynthetic mats were not transported intact and preserved in the deepest part of the lake. We hypothesize that most of the organic-walled microfossils preserved, even those that have benthic ecologies, have been transported within the lake waters including remobilization of shallow benthic systems. This interpretation is consistent with bedforms that record traction currents as well as evidence of sediment gravity flows. Samples collected from the high-energy PRF18 section with abundant density currents contained broken microfossils of low-diversity (6-7 species of sphaeromorphs, discoids, multicellular forms, and filamentous/benthic prokaryotes), supporting ideas of transport potentially even from fluvial systems. Transportation of organic remains from shallow light-filled environments to deeper regions of the lake is an important factor to consider for interpretation of diversity of microfossil

assemblages in shallow aqueous systems and for Precambrian organic carbon cycling more broadly.

Early work from the Nonesuch Formation putatively identified steranes, biomarkers indicative of eukaryotes (Pratt et al., 1991), but recent analyses suggest this was contamination and any steranes present are below detection limits (Brocks et al., 2008; Brocks, 2018). This result contrasts with microfossil identifications of eukaryotes suggesting three options: a) eukaryotes are in low absolute-abundance compared to prokaryotes in the lake (in contrast with organic-walled microfossil species richness and abundance, Fig. S13) and a minor component of primary productivity, b) steranes were not preserved in the samples targeted for biomarker analyses (e.g. Cohen and Kodner (2021)) or c) the eukaryotic microfossils did not produce sterane precursors (sterols) and were thus stem-group organisms (e.g. Porter (2020)). Notably, the putative presence of euglenids and *Proterocladus* suggest that crown-group eukaryotes are present in Paleolake Nonesuch.

CONCLUSIONS

Following the end of volcanism and extension within the Midcontinent Rift, there was an extended period of sedimentation as the basin thermally subsided from ca. 1085 to 1050 Ma. While the environment was dominated by streams and rivers through this interval of sedimentation, changes in local hydrology led to the development of a lake ca. 1075 Ma and the deposition of the Nonesuch Formation. The lateral extent of the Nonesuch Formation indicates that the lake was large and extended over at least 300 km. Paleomagnetic directions held by detrital hematite and magnetite within the Nonesuch Formation constrains the paleolatitude of deposition to have been 7.1±2.8°N.

Given that the ~200 meters of Nonesuch Formation strata is within a ~14,000 meter interval of terrestrial deposits and is early in the thermal subsidence phase of the basin, it is very unlikely that the basin was below sea level and could have been influenced by an incursion of seawater. Rather, the Nonesuch Formation represents a terrestrial lake environment that was rapidly colonized by diverse prokaryotic and eukaryotic biota. These organisms lived and were preserved in oxygenated waters; they are best preserved at intermediate depths and oxygen-levels. The deepest lake sediments record anoxia in which microbial iron reduction led to the dissolution of iron oxides and sulfate reduction led to the formation of sulfides. These anerobic metabolisms significantly impacted the iron mineralogy of the sediments in the deeper water facies and could have contributed to the degradation of microfossils. While the lake was anoxic at depth (with anoxia potentially restricted to pore waters), coeval environments at intermediate and shallow depths were oxygenated as constrained by the magnetic iron oxide assemblages.

This redox-stratified lake system bears a passing resemblance to ones that might be found on other terrestrial planets; analyses of Gale Crater by the Mars Science Laboratory Rover suggest the ancient lake filling that basin had shallow oxidized waters and deep anoxic waters (Hurowitz et al., 2017). While the palynological community has targeted rocks with low-organic carbon for decades (Butterfield, 1990), this search-image is not the traditional one for paleobiology studies, which typically target anoxic sediments and sedimentary rocks as they often have high-organic contents due to slower rates of oxidative degradation (Hartnett et al., 1998; Inagaki et al., 2005; Hays et al., 2017). Minimally impacted by metamorphism and deposited in a time-period without bioturbation, the Nonesuch Formation provides insight into preservation of biosignatures with implications for the search for early life on Earth and other planets. The excellent preservation of the Nonesuch sediments and biota give a unique window into a tropical rift lake system 1.1 billion years ago providing a path for future discoveries.

ACKNOWLEDGMENTS

Research permits that enabled sampling from the Wisconsin Department of Natural Resources, Iron County, and the Michigan Department of Natural Resources are gratefully acknowledged. Melanie Humphrey from the Michigan Department of Environmental Quality helped with access and sampling of cores at the Upper Peninsula Geological Repository. Madeline Swanson-Hysell assisted in georeferencing geologic maps. Robert Sherwood, Grady Florence, and James Pierce assisted in magnetic sample collection, sample preparation, and thermal demagnetization analyses respectively. Bas van de Schootbrugge and Wilson A. Taylor provided field assistance associated with palynological sample collection. Conversations with Esther Stewart provided insight on the sedimentology of the Nonesuch Formation and comments from Heda Agić improved the paleontological context. We thank the editor, Robert Rainbird, and two anonymous reviewers for their helpful comments on all aspects of the manuscript. Project research was supported by NSF EAR-1847277 to N.L.S.-H., a Miller Research Fellowship to S.P.S., an Esper Larsen fund grant to N.L.S.-H., a visiting fellowship to the Institute for Rock Magnetism (IRM) to N.L.S.-H., and NERC funding to C.H.W. for fieldwork and palynological processing. The IRM and its visiting fellowship program are made possible through the Instrumentation and Facilities program of the National Science Foundation, Earth Science Division and funding from the University of Minnesota. Data associated with this study as well as Python code that conducts data analysis within Jupyter notebooks are available in a Github repository associated with this work (`https://github.com/Swanson-Hysell-Group/Nonesuch_Formation`) that is also archived on Zenodo (`(https://doi.org/10.5281/zenodo.8034426)`).

APPENDIX

ROCK MAGNETIC EXPERIMENT METHODS

Room-temperature measurements using a Princeton Measurements Vibrating Sample Magnetometer at the Institute for Rock Magnetism (University of Minnesota) were performed on 238 samples in total. Rock chips between 0.17 to 6.3 g were used for these analyses with two different holders depending on mass. Hysteresis loops up to 1 T allowed determination of B_c, M_s, and M_{rs} while direct current demagnetization curves up to 1.5 T provided B_{cr} and coercivity spectra. Coercivity spectra were obtained by taking the derivative of the direct current demagnetization curves. In most samples, these spectra indicate

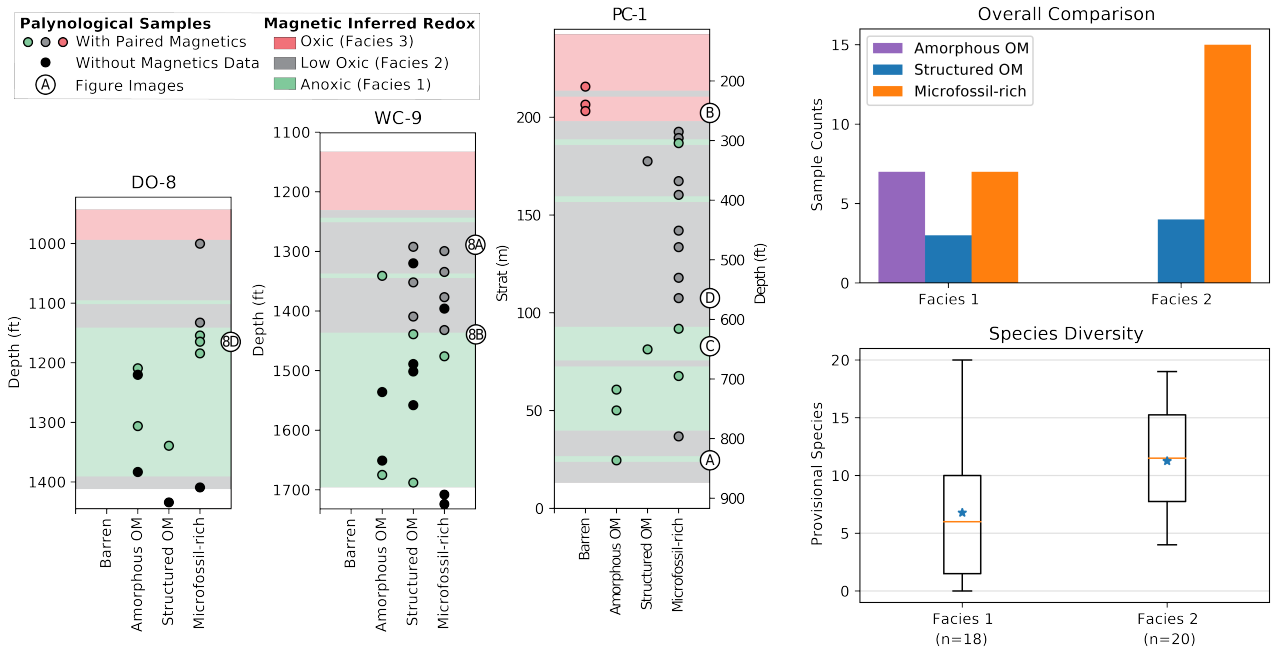

Figure 10: Palynological data shown in the context of stratigraphic position and magnetic-mineralogy-based redox interpretations for three drill cores. Organic matter (OM) was categorized into one of four categories: 1) barren; 2) amorphous (sometimes in chunks suggestive of microbial mats) with no (or in 1 case rare) microfossils; 3) structured with low-density scrappy palynomorphs that can be difficult to identity; 4) microfossil-rich. Stratigraphic plots show these categorized samples which are color-coded by redox if paired magnetic measurements were made; broad redox interpretations are shown with the background colors. Microfossil images from DO-8 and WC-9 in Fig. 8 and organic matter classification images from PC-1 in Fig. S12 are keyed via text in circles on the right side of the plots. The histogram in the upper right highlights that anoxic Facies 1 contains more amorphous organic matter than low-oxic Facies 2 which has more microfossil-rich samples. Species diversity is typically greater in Facies 2 as seen in the box plot in the lower right. The box represents the lower and upper quartiles of the number of provisional species, with the orange line indicating the median, the blue star indicating the mean, and whiskers showing the range of the data.

that more than one phase is present and they were deconvolved with skewed log-gaussian distributions using the MAX UnMix program (Maxbauer et al. (2016); Figs. 3 and 4).

Magnetite abundance was quantified by dividing M_s by that for pure magnetite (92 Am^2/kg) following Slotznick et al. (2020). Even when other ferromagnetic phases are present, this approach can be justified given how relatively large M_s values are for magnetite. This abundance can be considered a minimum value as it assumes all magnetite is stoichiometric; in order to account for uncertainty in the composition, and therefore M_s, the average value for maghemite (63.6 Am^2/kg, Peters and Dekkers (2003)) was used to calculate an upper bound. Hematite abundance was quantified using M_{rs} with the proportions of hematite components estimated from unmixed coercivity spectra (Table S2). The error bars incorporate uncertainty in M_{rs} and its variability with grain size. The M_{rs} value used for detrital hematite was 0.22 Am^2/kg (range of 0.19 to 0.26 Am^2/kg) and for pigmentary hematite was 0.15 Am^2/kg (range of 0.05 to 0.25 Am^2/kg) (Özdemir and Dunlop, 2014).

Mineral identifications from these room-temperature rock magnetic experiments were corroborated with diagnostic low-temperature magnetic mineral transitions observed in low-temperature cycling experiments (between 10 and 300 K). Two to four specimens per stratigraphic section or core were run through a suite of low-temperature experiments using a Quantum Designs Magnetic Property Measurement System at the Institute for Rock Magnetism. Specifically, samples were a) cooled from 300 to 10 K in a 2.5-T field, then the field was turned off, and remanence measurements were made upon warming; b) cooled again to 10 K with no applied field, at 10 K pulsed with a 2.5-T field, and remanence measurements were made upon warming ; c) pulsed with a 2.5-T field at 300 K before cooling to 10 K and warming back to 300 K during which remanence measurements were collected (Figs. S1-S3).

PALEOMAGNETIC METHODS

One-hundred and sixty-three oriented paleomagnetic core samples (2.5 cm in diameter) were collected from the PFR18 (Potato River Falls) section. Following sample orientation, small portions of the host rocks of the core holes were removed through chiseling to minimize the visual impact of drill hole collection, leaving a rough natural-looking surface. Specimens were cut from these cores; one was used for paleomagnetism and for sixty of the samples, a paired specimen was

used for the rock magnetic experiments described above. Thermal demagnetization was performed in the UC Berkeley Paleomagnetism Laboratory in ~38 temperature steps that typically proceeded at progressively higher resolution from 50°C to 25°C to 15°C to 10°C to 4°C ending in 2°C at 696°C (specimen PF18-75a in Fig. 6). Remanent magnetization vectors were measured at each step using a 2G Enterprises superconducting rock magnetometer. Fits to magnetization components were made using PmagPy (Tauxe et al., 2016) and the measurement level data as well as the interpreted directions for each specimen are available in the MagIC database (https://doi.org/10.7288/V4/MAGIC/19390).

PETROGRAPHIC MICROSCOPY METHODS

Optical and electron microscopy was also performed on 15 thin sections made from samples at the PRF18 section and PC-1, as a representative proximal and distal section respectively. Electron microscopy was performed using a Thermo Scientific Helios 5CX Dual Beam scanning electron microscope (SEM) at the Dartmouth College Electron Microscopy Facility. This instrument contains a paired Oxford Instruments UltimMax 100 energy dispersive X-ray spectrometer (EDS) that is used to estimate elemental abundance at submicron-sized spots. This EDS system was used to collect spectra at specified points as well as in a mapped grid.

X-RAY DIFFRACTION METHODS

Forty-three specimens were measured on a PANalytical Empyrean Series 2 powder diffractometer at the University of Oxford. The instrument is equipped with a PIXcel1D detector and utilized a Co Kα source operated at 40 kV and 40 mA. Prior to analysis, sample powders were deposited on a single crystal silicon substrate that has zero detectable background. Samples were then mounted on a spinning sample stage during analysis (rotating at 10 revolutions per minute). Three different approaches were taken to develop the data. First, a bulk analysis from 5 to 80° 2θ was used to identify major minerals present via the International Center for Diffraction Data (ICDD) Powder Diffraction File 4+ database of mineral standards. Once identified, semi-quantitative bulk mineral abundances were calculated using the reference intensity ratio method (Snyder and Bish, 1989) and scale factors published with mineral standards in the ICDD PDF-4+ database.

In order to further constrain clay mineralogy beyond the bulk analysis, a second analysis was run on the same powdered specimen by focusing on the high-angle region of the diffraction pattern between 69 and 75° 2θ. Clay mineral speciation at the family level (i.e. Fe-rich chlorites and/or serpentine (berthierine), Mg-rich chlorites, glauconites, Al-rich dioctahedral 2:1 clays and micas, and kaolinites) is possible due to diagnostic 060 reflections corresponding to octahedral layer composition (Środoń, 2001). These “high-angle" XRD data were analyzed using the Panalytical HighScore software which deconvolves and fits the peaks enabling them to be assigned to specific minerals. Clay abundance determined using this method scales linearly with peak area in this part of the spectra. As a result, quantification of clay minerals is possible by assessing relative abundances with respect to quartz as an internal standard. Following this determination, these abundances are multiplied by the total quartz content determined through bulk analysis.

The third XRD analysis was performed on clay peels of the same powdered core samples and some of the PRF18 samples. Clay peels were produced using the methodology described in Moore and Reynolds (1997). Ten grams of whole rock samples were blended in a Waring Commercial Blender with 200 ml of deionized water and sodium phosphate as a dispersant to inhibit flocculation of the clay particles. The fine-grained portion was decanted into large beakers (~800 ml) and ultrasonicated for 3-5 minutes. To separate the <2 μm fraction, the slurry was left for four hours to gravitationally settle. The suspended fines were then decanted into 100ml bottles. Using the Millipore Filter Transfer Method (Drever, 1973), the suspended fines were then adhered to a 47 mm 0.45 μm hydrophilic nylon filter, using a vacuum filtration apparatus (~3 minutes). The sample on the filter was then placed face-down on a single silicon crystal 0-background holder, and dried in an oven at 50°C for 3-4 minutes. The filter was then peeled away, leaving an oriented clay sample on the zero background plate. XRD analyses were performed on this “air-dried" sample following the procedures for the first bulk analysis. Afterwards, the samples were placed above a tray of glycol in an oven at 50°C for several hours (overnight) and then re-analyzed on the diffractometer. After glycolation, most samples showed swelling or collapse in the smectite region, indicating a fair amount of interlayered illite and smectite.

PALYNOLOGICAL METHODS

Samples of ~40 to 100 g were collected from drill cores and outcrop focusing on shales and siltstones (predominantly dark gray in color). These samples were crushed and treated in a sequence of 10% HCl – 52% HF – 10% HCl dissolutions. Residues were water washed and filtered through a 10 μm screen. Acid insoluble minerals were removed by heavy liquid centrifugation and the filtrate mounted onto regular glass microscope slides using a synthetic mounting medium. Prepared slides were examined on a Zeiss Universal microscope equipped with an Achromatic-Aplanatic (ACHR APL) 1.4 substage condenser, and Zeiss Plan-Apochromat (APO) 25/0.65 and Leitz APO 40x/0.95 objectives. Images were captured with a Nikon D700 digital camera back mounted directly to the microscope phototube, in combination with a coplanar electronic shutter mounted between the field stop and condenser. The light source was a 20 W halogen bulb with a color temperature of 3450° K. No infrared filters were used in the optical light path.

REFERENCES

Allaby, M., 2020, A Dictionary of Geology and Earth Sciences: Oxford University Press, doi:10.1093/acref/9780198839033.001.0001.

Anderson, R. P., Tosca, N. J., Gaines, R. R., Koch, N. M., and Briggs, D. E., 2018, A mineralogical signature for Burgess Shale–type fossilization: Geology, vol. 46, pp. 347–350, doi: 10.1130/g39941.1.

Anderson, R. P., Tosca, N. J., Saupe, E. E., Wade, J., and Briggs, D. E., 2021, Early formation and taphonomic sig-

nificance of kaolinite associated with Burgess Shale fossils: Geology, vol. 49, pp. 355–359, doi:10.1130/g48067.1.

Anderson, R. R., 1997, Middle Proterozoic to Cambrian rifting, central North America, Geological Society of America, vol. 312, chap. Keweenawan Supergroup clastic rocks in the Midcontinent Rift of Iowa, pp. 211–230: doi:10.1130/0-8137-2312-4.211.

Ashley, G. M., 2007, Orbital rhythms, monsoons, and playa lake response, Olduvai Basin, equatorial East Africa (ca. 1.85–1.74 Ma): Geology, vol. 35, p. 1091, doi:10.1130/g24163a.1.

Berbee, M. L., Strullu-Derrien, C., Delaux, P.-M., Strother, P. K., Kenrick, P., Selosse, M.-A., and Taylor, J. W., 2020, Genomic and fossil windows into the secret lives of the most ancient fungi: Nature Reviews Microbiology, doi:10.1038/s41579-020-0426-8.

Bergmann, K. D., Grotzinger, J. P., and Fischer, W. W., 2013, Biological influences on seafloor carbonate precipitation: PALAIOS, vol. 28, pp. 99–115, doi:10.2110/palo.2012.p12-088r.

Bethke, C. M. and Altaner, S. P., 1986, Layer-by-layer mechanism of smectite illitization and application to a new rate law: Clays and Clay Minerals, vol. 34, pp. 136–145, doi:10.1346/ccmn.1986.0340204.

Brocks, J. J., 2018, The transition from a cyanobacterial to algal world and the emergence of animals: Emerging Topics in Life Sciences, vol. 2, pp. 181–190, doi:10.1042/etls20180039.

Brocks, J. J., Grosjean, E., and Logan, G. A., 2008, Assessing biomarker syngeneity using branched alkanes with quaternary carbon (BAQCs) and other plastic contaminants: Geochimica et Cosmochimica Acta, vol. 72, pp. 871–888, doi:10.1016/j.gca.2007.11.028.

Butterfield, N. J., 1990, Organic preservation of non-mineralizing organisms and the taphonomy of the Burgess Shale: Paleobiology, vol. 16, pp. 272–286, doi:10.1017/S0094837300009994.

Callow, R. H., Battison, L., and Brasier, M. D., 2011, Diverse microbially induced sedimentary structures from 1 Ga lakes of the Diabaig Formation, Torridon Group, northwest Scotland: Sedimentary Geology, vol. 239, pp. 117–128, doi:10.1016/j.sedgeo.2011.06.002.

Cannon, W. F., 1992, The Midcontinent Rift in the Lake Superior region with emphasis on its geodynamic evolution: Tectonophysics, vol. 213, pp. 41–48, doi:10.1016/0040-1951(92)90250-A.

Cannon, W. F., Green, A. G., Hutchinson, D. R., Lee, M., Milkereit, B., Behrendt, J. C., Halls, H. C., Green, J. C., Dickas, A. B., Morey, G. B., Sutcliffe, R., and Spencer, C., 1989, The North American Midcontinent Rift beneath Lake Superior from GLIMPCE seismic reflection profiling: Tectonics, vol. 8, pp. 305–332, doi:10.1029/tc008i002p00305.

Cannon, W. F., Nicholson, S. W., Woodruff, L. G., Hedgman, C. A., and Schulz, K. J., 1995, Geologic map of the Ontonagon and part of the Wakefield 30' X 60' quadrangles, Michigan: USGS Miscellaneous Geologic Investigations Map I-2499.

Cannon, W. F., Peterman, Z. E., and Sims, P. K., 1993, Crustal-scale thrusting and origin of the Montreal River monocline – A 35-km-thick cross section of the Midcontinent Rift in northern Michigan and Wisconsin: Tectonics, vol. 12, pp. 728–744, doi:10.1029/93TC00204.

Cannon, W. F., Woodruff, L. G., Nicholson, S. W., and Hedgman, C. A., 1996, Bedrock geologic map of the Ashland and the northern part of the Ironwood 30' X 60' quadrangles, Wisconsin, and Michigan: USGS Miscellaneous Geologic Investigations Map I-2566.

Chen, C., Kukkadapu, R. K., Lazareva, O., and Sparks, D. L., 2017, Solid-phase Fe speciation along the vertical redox gradients in floodplains using XAS and Mössbauer spectroscopies: Environmental Science & Technology, vol. 51, pp. 7903–7912, doi:10.1021/acs.est.7b00700.

Cohen, P. A. and Kodner, R. B., 2021, The earliest history of eukaryotic life: uncovering an evolutionary story through the integration of biological and geological data: Trends in Ecology & Evolution, doi:10.1016/j.tree.2021.11.005.

Cohen, P. A. and Macdonald, F. A., 2015, The Proterozoic record of eukaryotes: Paleobiology, vol. 41, pp. 1–23.

Cumming, V. M., Poulton, S. W., Rooney, A. D., and Selby, D., 2013, Anoxia in the terrestrial environment during the late Mesoproterozoic: Geology, vol. 41, pp. 583–586, doi:10.1130/G34299.1.

Daniels, P. A., 1982, 7C: Upper Precambrian sedimentary rocks: Oronto Group, Michigan-Wisconsin: Geology and Tectonics of the Lake Superior Basin, pp. 107–134, doi:10.1130/mem156-p107.

Das, S., Hendry, M. J., and Essilfie-Dughan, J., 2010, Transformation of two-line ferrihydrite to goethite and hematite as a function of pH and temperature: Environmental Science & Technology, vol. 45, pp. 268–275, doi:10.1021/es101903y.

Deino, A., Kingston, J., Glen, J., Edgar, R., and Hill, A., 2006, Precessional forcing of lacustrine sedimentation in the late Cenozoic Chemeron Basin, Central Kenya Rift, and calibration of the Gauss/Matuyama boundary: Earth and Planetary Science Letters, vol. 247, pp. 41–60, doi:10.1016/j.epsl.2006.04.009.

Drever, J. I., 1973, The preparation of oriented clay mineral specimens for X-ray diffraction analysis by a filter-membrane peel technique: American Mineralogist, vol. 58, pp. 553–554.

Eberl, D. and Hower, J., 1976, Kinetics of illite formation: Geological Society of America Bulletin, vol. 87, p. 1326, doi:10.1130/0016-7606(1976)87<1326:koif>2.0.co;2.

Elmore, R. D., 1984, The Copper Harbor Conglomerate: A late Precambrian fining-upward alluvial fan sequence in northern Michigan: Geological Society of America Bulletin, vol. 95, pp. 610–617, doi:10.1130/0016-7606(1984)95<610:TCHCAL>2.0.CO;2.

Elmore, R. D., Milavec, G. J., Imbus, S. W., and Engel, M. H., 1989, The Precambrian Nonesuch Formation of the North American Mid-Continent Rift, sedimentology and organic geochemical aspects of lacustrine deposition: Precambrian Research, vol. 43, pp. 191–213, doi:10.1016/0301-9268(89)90056-9.

Embley, T. M. and Martin, W., 2006, Eukaryotic evolution, changes and challenges: Nature, vol. 440, pp. 623–630, doi:10.1038/nature04546.

Eugster, H. P., 1980, Chapter 15 Lake Magadi, Kenya, and Its Precursors: *In* Nissenbaum, A., ed., Developments in Sedimentology, Elsevier, pp. 195–232, doi:10.1016/s0070-4571(08)70239-5.

Fairchild, L. M., Swanson-Hysell, N. L., Ramezani, J., Sprain, C. J., and Bowring, S. A., 2017, The end of Midcontinent Rift magmatism and the paleogeography of Laurentia: Lithosphere, vol. 9, pp. 117–133, doi:10.1130/L580.1.

Gallagher, T. M., Sheldon, N. D., Mauk, J. L., Petersen, S. V., Gueneli, N., and Brocks, J. J., 2017, Constraining the thermal history of the North American Midcontinent Rift System using carbonate clumped isotopes and organic thermal maturity indices: Precambrian Research, vol. 294, pp. 53–66, doi:10.1016/j.precamres.2017.03.022.

Gibbs, S. P., 1978, The chloroplasts of euglena may have evolved from symbiotic green algae: Canadian Journal of Botany, vol. 56, pp. 2883–2889.

Gibson, T. M., Shih, P. M., Cumming, V. M., Fischer, W. W., Crockford, P. W., Hodgskiss, M. S., Wörndle, S., Creaser, R. A., Rainbird, R. H., Skulski, T. M., and et al., 2018, Precise age of Bangiomorpha pubescens dates the origin of eukaryotic photosynthesis: Geology, vol. 46, pp. 135–138, doi:10.1130/g39829.1.

Gold, D. A., Caron, A., Fournier, G. P., and Summons, R. E., 2017, Paleoproterozoic sterol biosynthesis and the rise of oxygen: Nature, vol. 543, pp. 420–423, doi:10.1038/nature21412.

Green, J., 1983, Geologic and geochemical evidence for the nature and development of the Middle Proterozoic (Keweenawan) Midcontinent Rift of North America: Tectonophysics, vol. 94, pp. 413–437, doi:10.1016/0040-1951(83)90027-6.

Gutiérrez, L., Barrón, V., Andrés-Vergés, M., Serna, C. J., Veintemillas-Verdaguer, S., Morales, M. P., and Lázaro, F. J., 2016, Detailed magnetic monitoring of the enhanced magnetism of ferrihydrite along its progressive transformation into hematite: Journal of Geophysical Research: Solid Earth, vol. 121, pp. 4118–4129, doi:10.1002/2016jb013016.

Hartnett, H. E., Keil, R. G., Hedges, J. I., and Devol, A. H., 1998, Influence of oxygen exposure time on organic carbon preservation in continental margin sediments: Nature, vol. 391, pp. 572–575, doi:10.1038/35351.

Hays, L. E., Graham, H. V., Marais, D. J. D., Hausrath, E. M., Horgan, B., McCollom, T. M., Parenteau, M. N., Potter-McIntyre, S. L., Williams, A. J., and Lynch, K. L., 2017, Biosignature preservation and detection in mars analog environments: Astrobiology, vol. 17, pp. 363–400, doi:10.1089/ast.2016.1627.

Henry, S. G., 1976, Paleomagnetism of the upper Keweenawan sediments: the Nonesuch Shale and Freda Sandstone: Master's thesis, University of Michigan.

Henry, S. G., Mauk, F. J., and Van der Voo, R., 1977, Paleomagnetism of the upper Keweenawan sediments: Nonesuch Shale and Freda Sandstone: Canadian Journal of Earth Science, vol. 14, pp. 1128–1138, doi:10.1139/e77-103.

Hise, C. R. V. and Leith, C. K., 1911, The geology of the lake superior region: Tech. rep., USGS, doi:10.3133/m52.

Hodgin, E. B., Swanson-Hysell, N. L., DeGraff, J. M., Kylander-Clark, A. R., Schmitz, M., Turner, A. C., Zhang, Y., and Stolper, D. A., 2022, Final inversion of the Midcontinent Rift during the Rigolet Phase of the Grenvillian orogeny: Geology, vol. 50, pp. 547–551, doi:10.1130/G49439.1.

Hornibrook, E. R. C., 1996, Berthierine from the Lower Cretaceous Clearwater Formation, Alberta, Canada: Clays and Clay Minerals, vol. 44, pp. 1–21, doi:10.1346/ccmn.1996.0440101.

Hren, M. T. and Sheldon, N. D., 2020, Terrestrial microbialites provide constraints on the mesoproterozoic atmosphere: The Depositional Record, vol. 6, pp. 4–20.

Hurowitz, J. A., Grotzinger, J. P., Fischer, W. W., McLennan, S. M., Milliken, R. E., Stein, N., Vasavada, A. R., Blake, D. F., Dehouck, E., Eigenbrode, J. L., Fairén, A. G., Frydenvang, J., Gellert, R., Grant, J. A., Gupta, S., Herkenhoff, K. E., Ming, D. W., Rampe, E. B., Schmidt, M. E., Siebach, K. L., Stack-Morgan, K., Sumner, D. Y., and Wiens, R. C., 2017, Redox stratification of an ancient lake in Gale crater, Mars: Science, vol. 356, doi:10.1126/science.aah6849.

Imbus, S. W., Engel, M. H., and Elmore, R. D., 1990, Organic geochemistry and sedimentology of middle Proterozoic Nonesuch Formation–hydrocarbon source rock assessment of a lacustrine rift deposit: Chapter 12: *In* Lacustrine Basin Exploration: Case Studies and Modern Analogs, AAPG, pp. 197–208.

Imbus, S. W., Macko, S. A., Elmore, D. R., and Engel, M. H., 1992, Stable isotope (C, S, N) and molecular studies on the Precambrian Nonesuch Shale (Wisconsin-Michigan, U.S.A.): Evidence for differential preservation rates, depositional environment and hydrothermal influence: Chemical Geology: Isotope Geoscience section, vol. 101, pp. 255–281, doi:10.1016/0009-2541(92)90007-r.

Inagaki, F., Okada, H., Tsapin, A. I., and Nealson, K. H., 2005, MICROBIAL SURVIVAL: The paleome: A sedimentary genetic record of past microbial communities: Astrobiology, vol. 5, pp. 141–153, doi:10.1089/ast.2005.5.141.

Jackson, C., Knoll, A. H., Chan, C. X., and Verbruggen, H., 2018, Plastid phylogenomics with broad taxon sampling further elucidates the distinct evolutionary origins and timing of secondary green plastids: Scientific Reports, vol. 8, pp. 1–10, doi:10.1038/s41598-017-18805-w.

Jahren, J. S., 1989, Compositional variations in diagenetic chlorites and illites, and relationships with formation-water chemistry: Clay Minerals, vol. 24, pp. 157–170, doi:10.1180/claymin.1989.024.2.04.

Jiang, Z., Liu, Q., Dekkers, M. J., Tauxe, L., Qin, H., Barrón, V., and Torrent, J., 2015, Acquisition of chemical remanent magnetization during experimental ferrihydrite–hematite conversion in earth-like magnetic field—implications for paleomagnetic studies of red beds: Earth and Planetary Science Letters, vol. 428, pp. 1–10, doi:10.1016/j.epsl.2015.07.024.

Jiang, Z., Liu, Q., Roberts, A. P., Barrón, V., Torrent, J., and Zhang, Q., 2018, A new model for transformation of fer-

rihydrite to hematite in soils and sediments: Geology, doi: 10.1130/g45386.1.

Jones, S., Prave, A., Raub, T., Cloutier, J., Stüeken, E., Rose, C., Linnekogel, S., and Nazarov, K., 2020, A marine origin for the late Mesoproterozoic Copper Harbor and Nonesuch Formations of the Midcontinent Rift of Laurentia: Precambrian Research, vol. 336, p. 105,510, doi:10.1016/j.precamres.2019.105510.

Lax, G., Kolisko, M., Eglit, Y., Lee, W. J., Yubuki, N., Karnkowska, A., Leander, B., Burger, G., Keeling, P., and Simpson, A., 2021, Multigene phylogenetics of euglenids based on single-cell transcriptomics of diverse phagotrophs: Molecular phylogenetics and evolution, vol. 159, p. 107,088, doi:10.1016/j.ympev.2021.107088.

Loron, C. C., Rainbird, R. H., Turner, E. C., Greenman, J. W., and Javaux, E. J., 2018, Implications of selective predation on the macroevolution of eukaryotes: evidence from Arctic Canada: Emerging topics in life sciences, vol. 2, pp. 247–255, doi:10.1042/ETLS20170153.

Mauk, J. L. and Hieshima, G. B., 1992, Organic matter and copper mineralization at White Pine, Michigan, U.S.A.: Chemical Geology, vol. 99, pp. 189–211, doi:10.1016/0009-2541(92)90038-7.

Mauk, J. L., Kelly, W. C., van der Pluijm, B. A., and Seasor, R. W., 1992, Relations between deformation and sediment-hosted copper mineralization: Evidence from the White Pine part of the Midcontinent rift system: Geology, vol. 20, p. 427, doi:10.1130/0091-7613(1992)020<0427:rbdash>2.3.co;2.

Maxbauer, D. P., Feinberg, J. M., and Fox, D. L., 2016, MAX UnMix: A web application for unmixing magnetic coercivity distributions: Computers and Geosciences, vol. 95, pp. 140–145, doi:10.1016/j.cageo.2016.07.009.

Moczydłowska, M., 2015, Algal affinities of Ediacaran and Cambrian organic-walled microfossils with internal reproductive bodies: Tanariumand and other morphotypes: Palynology, vol. 40, pp. 83–121, doi:10.1080/01916122.2015.1006341.

Moore, D. and Reynolds, R., 1997, X-ray Diffraction and the Identification and Analysis of Clay Minerals: Oxford University Press.

Moore, L. R., Moore, J. R. M., and Spinner, E., 1969, A geomicrobiologigal study of the pre-Cambrian Nonesuch Shale: Proceedings of the Yorkshire Geological Society, vol. 37, pp. 351–394, doi:10.1144/pygs.37.3.351.

Noffke, N., Gerdes, G., Klenke, T., and Krumbein, W. E., 2001, Microbially induced sedimentary structures: A new category within the classification of primary sedimentary structures: Journal of Sedimentary Research, vol. 71, pp. 649–656, doi:10.1306/2dc4095d-0e47-11d7-8643000102c1865d.

Ojakangas, R. W., 1994, Sedimentology and provenance of the early Proterozoic Michigamme Formation and Goodrich Quartzite, northern Michigan; regional stratigraphic implications and suggested correlations: USGS Bulletin 1904-R, doi:10.3133/b1904r.

Ojakangas, R. W. and Morey, G. B., 1982, 7: Proterozoic sedimentary rocks: *In* Geological Society of America Memoirs, Geological Society of America, pp. 83–84, doi:10.1130/mem156-p83.

Ojakangas, R. W., Morey, G. B., and Green, J. C., 2001, The Mesoproterozoic Midcontinent Rift System, Lake Superior Region, USA: Sedimentary Geology, vol. 141-142, pp. 421–442, doi:10.1016/s0037-0738(01)00085-9.

Özdemir, Ö. and Dunlop, D. J., 2014, Hysteresis and coercivity of hematite: Journal of Geophysical Research: Solid Earth, vol. 119, pp. 2582–2594, doi:10.1002/2013JB010739.

Peters, C. and Dekkers, M., 2003, Selected room temperature magnetic parameters as a function of mineralogy, concentration and grain size: Physics and Chemistry of the Earth, Parts A/B/C, vol. 28, pp. 659–667, doi:10.1016/s1474-7065(03)00120-7.

Pierce, J., Zhang, Y., Hodgin, E. B., and Swanson-Hysell, N. L., 2022, Quantifying inclination shallowing and representing flattening uncertainty in sedimentary paleomagnetic poles: Geochemistry, Geophysics, Geosystems, doi:10.1029/2022gc010682.

Porter, S. M., 2020, Insights into eukaryogenesis from the fossil record: Interface Focus, vol. 10, p. 20190,105, doi:10.1098/rsfs.2019.0105.

Porter, S. M., Agić, H., and Riedman, L. A., 2018, Anoxic ecosystems and early eukaryotes: Emerging Topics in Life Sciences, p. ETLS20170162, doi:10.1042/etls20170162.

Pratt, L. M., Summons, R. E., and Hieshima, G. B., 1991, Sterane and triterpane biomarkers in the Precambrian Nonesuch Formation, North American Midcontinent Rift: Geochimica et Cosmochimica Acta, vol. 55, pp. 911–916, doi:10.1016/0016-7037(91)90351-5.

Preston, T., Stewart, W., and Reynolds, C., 1980, Bloom-forming cyanobacterium microcystis aeruginosa overwinters on sediment surface: Nature, vol. 288, pp. 365–367.

Price, K. L. and McDowell, S. D., 1993, Illite/smectite geothermometry of the Proterozoic Oronto Group, Midcontinent Rift System: Clays and Clay Minerals, vol. 41, pp. 134–147, doi:10.1346/CCMN.1993.0410203.

Rainbird, R. H., Rooney, A. D., Creaser, R. A., and Skulski, T., 2020, Shale and pyrite Re-Os ages from the Hornby Bay and Amundsen basins provide new chronological markers for Mesoproterozoic stratigraphic successions of northern Canada: Earth and Planetary Science Letters, vol. 548, doi:10.1016/j.epsl.2020.116492.

Rico, K. I., Sheldon, N. D., Gallagher, T. M., and Chappaz, A., 2019, Redox chemistry and molybdenum burial in a Mesoproterozoic lake: Geophysical Research Letters, vol. 46, pp. 5871–5878, doi:10.1029/2019gl083316.

Risacher, F., Alonso, H., and Salazar, C., 2003, The origin of brines and salts in Chilean salars: a hydrochemical review: Earth-Science Reviews, vol. 63, pp. 249–293, doi:10.1016/s0012-8252(03)00037-0.

Rosendahl, B. and Livingstone, D., 1983, Rift lakes of East Africa - new seismic data and implications for future research: Episodes, vol. 6, pp. 14–19, doi:10.18814/epiiugs/1983/v6i1/004.

Rothman, D. H. and Forney, D. C., 2007, Physical model for the decay and preservation of marine organic carbon: Science, vol. 316, pp. 1325–1328, doi:10.1126/science.1138211.

Sánchez-Baracaldo, P., Raven, J. A., Pisani, D., and Knoll, A. H., 2017, Early photosynthetic eukaryotes inhabited low-salinity habitats: Proceedings of the National Academy of Sciences, vol. 114, pp. E7737–E7745, doi:10.1073/pnas.1620089114.

Scholz, C. A., Rosendahl, B. R., and Scott, D. L., 1990, Development of coarse-grained facies in lacustrine rift basins: Examples from East Africa: Geology, vol. 18, pp. 140–144, doi:10.1130/0091-7613(1990)018<0140:docgfi>2.3.co;2.

Slotznick, S. P., Sperling, E. A., Tosca, N. J., Miller, A. J., Clayton, K. E., Helmond, N. A. G. M., Slomp, C. P., and Swanson-Hysell, N. L., 2020, Unraveling the mineralogical complexity of sediment iron speciation using sequential extractions: Geochemistry, Geophysics, Geosystems, vol. 21, doi:10.1029/2019gc008666.

Slotznick, S. P., Swanson-Hysell, N. L., and Sperling, E. A., 2018, Oxygenated Mesoproterozoic lake revealed through magnetic mineralogy: Proceedings of the National Academy of Sciences, vol. 1115, pp. 12,938–12,943, doi:10.1073/pnas.1813493115.

Snyder, R. L. and Bish, D. L., 1989, Quantitative analysis: Reviews in Mineralogy and Geochemistry, vol. 20, pp. 101–144.

Spinks, S. C., Parnell, J., Bowden, S. A., Taylor, R. A. D., and Maclean, M. E., 2014, Enhanced organic carbon burial in large Proterozoic lakes: Implications for atmospheric oxygenation: Precambrian Research, vol. 255, pp. 202–215, doi:10.1016/j.precamres.2014.09.026.

Środoń, J., 2001, Quantitative X-ray diffraction analysis of clay-bearing rocks from random preparations: Clays and Clay Minerals, vol. 49, pp. 514–528, doi:10.1346/ccmn.2001.0490604.

Stewart, E. K. and Mauk, J. L., 2017, Sedimentology, sequence-stratigraphy, and geochemical variations in the Mesoproterozoic Nonesuch Formation, northern Wisconsin, USA: Precambrian Research, vol. 294, pp. 111–132, doi:10.1016/j.precamres.2017.03.023.

Strother, P. K., Brasier, M. D., Wacey, D., Timpe, L., Saunders, M., and Wellman, C. H., 2021, A possible billion-year-old holozoan with differentiated multicellularity: Current Biology, vol. 31, pp. 2658–2665.e2, doi:10.1016/j.cub.2021.03.051.

Strother, P. K., Taylor, W. A., Van De Schootbrugge, B., Leander, B. S., and Wellman, C. H., 2020, Pellicle ultrastructure demonstrates that Moyeria is a fossil euglenid: Palynology, vol. 44, pp. 461–471, doi:10.1080/01916122.2019.1625457.

Strother, P. K. and Wellman, C. H., 2016, Palaeoecology of a billion-year-old non-marine cyanobacterium from the Torridon Group and Nonesuch Formation: Palaeontology, vol. 59, pp. 89–108, doi:10.1111/pala.12212.

Strother, P. K. and Wellman, C. H., 2021, The Nonesuch Formation Lagerstätte: a rare window into freshwater life one billion years ago: Journal of the Geological Society, vol. 178, doi:10.1144/jgs2020-133.

Stüeken, E. E., Jones, S., Raub, T. D., Prave, A. R., Rose, C. V., Linnekogel, S., and Cloutier, J., 2020, Geochemical fingerprints of seawater in the Late Mesoproterozoic Midcontinent Rift, North America: Life at the marine-land divide: Chemical Geology, vol. 553, p. 119,812, doi:10.1016/j.chemgeo.2020.119812.

Suga, H. and Ruiz-Trillo, I., 2013, Development of ichthyosporeans sheds light on the origin of metazoan multicellularity: Developmental Biology, vol. 377, pp. 284–292, doi:10.1016/j.ydbio.2013.01.009.

Suga, H. and Ruiz-Trillo, I., 2015, Filastereans and Ichthyosporeans: Models to Understand the Origin of Metazoan Multicellularity, Springer Netherlands, pp. 117–128: doi:10.1007/978-94-017-9642-2_6.

Suszek, T., 1997, Petrography and sedimentation of the middle Proterozoic (Keweenawan) Nonesuch Formation, western Lake Superior region, Midcontinent Rift System: Geological Society of America Special Papers, vol. 312, pp. 195–210, doi:10.1130/0-8137-2312-4.195.

Swanson-Hysell, N. L., 2021, The Precambrian Paleogeography of Laurentia: *In* Pesonen, L. J., Evans, D. A. D., Elming, S. Å., Salminen, J. M., and Veikkolainen, T., eds., Ancient Supercontinents and the Paleogeography of the Earth, Elsevier, pp. 109–153, doi:10.1016/B978-0-12-818533-9.00009-6.

Swanson-Hysell, N. L., Ramezani, J., Fairchild, L. M., and Rose, I. R., 2019, Failed rifting and fast drifting: Midcontinent Rift development, Laurentia's rapid motion and the driver of Grenvillian orogenesis: GSA Bulletin, vol. 131, pp. 913–940, doi:10.1130/b31944.1.

Swanson-Hysell, N. L., Rivers, T., and van der Lee, S., 2022, The late Mesoproterozoic to early Neoproterozoic Grenvillian Orogeny and the assembly of Rodinia: Turning point in the tectonic evolution of Laurentia: *In* Whitmeyer, S., Kellett, D., Tikoff, B., and Williams, M., eds., Laurentia: Evolution of a Continent, Geological Society of America Memoir, doi:10.1130/2022.1220(14).

Swanson-Hysell, N. L., Fairchild, L. M., and Slotznick, S. P., 2019, Primary and secondary red bed magnetization constrained by fluvial intraclasts: Journal of Geophysical Research: Solid Earth, vol. 124, pp. 4276–4289, doi:10.1029/2018jb017067.

Swenson, J. B., Person, M., Raffensperger, J. P., Cannon, W. F., Woodruff, L. G., and Berndt, M. E., 2004, A hydrogeologic model of stratiform copper mineralization in the Midcontinent Rift System, Northern Michigan, USA: Geofluids, vol. 4, pp. 1–22, doi:10.1111/j.1468-8123.2004.00062.x.

Symons, D. T. A., Kawasaki, K., and Diehl, J. F., 2013, Age and genesis of the White Pine stratiform copper mineralization, northern Michigan, USA, from paleomagnetism: Geofluids, vol. 13, pp. 112–126, doi:10.1111/gfl.12024.

Tang, Q., Pang, K., Yuan, X., and Xiao, S., 2020, A one-billion-year-old multicellular chlorophyte: Nature Ecology & Evolution, vol. 4, pp. 543–549, doi:10.1038/s41559-020-1122-9.

Tauxe, L., 2010, Essentials of paleomagnetism: Univ. of California Press.

Tauxe, L. and Kent, D. V., 2004, A simplified statistical model for the geomagnetic field and the detection of shallow bias in paleomagnetic inclinations: was the ancient magnetic field dipolar?: *In* Timescales of the Paleomagnetic field, AGU Geophysical Monograph Series, pp. 101–115, doi:10.1029/145GM08.

Tauxe, L., Shaar, R., Jonestrask, L., Swanson-Hysell, N., Minnett, R., Koppers, A., Constable, C., Jarboe, N., Gaastra, K., and Fairchild, L., 2016, PmagPy: Software package for paleomagnetic data analysis and a bridge to the Magnetics Information Consortium (MagIC) Database: Geochemistry, Geophysics, Geosystems, vol. 17, pp. 2450–2463, doi:10.1002/2016GC006307.

Ullman, D. J., Carlson, A. E., LeGrande, A. N., Anslow, F. S., Moore, A. K., Caffee, M., Syverson, K. M., and Licciardi, J. M., 2015, Southern Laurentide ice-sheet retreat synchronous with rising boreal summer insolation: Geology, vol. 43, pp. 23–26, doi:10.1130/g36179.1.

van Nugteren, P., Moodley, L., Brummer, G.-J., Heip, C. H., Herman, P. M., and Middelburg, J. J., 2009, Seafloor ecosystem functioning: the importance of organic matter priming: Marine biology, vol. 156, pp. 2277–2287, doi:10.1007/s00227-009-1255-5.

Velde, B. and Vasseur, G., 1992, Estimation of the diagenetic smectite to illite transformation in time-temperature space: American Mineralogist, vol. 77, pp. 967–976.

Verspagen, J. M. H., Snelder, E. O. F. M., Visser, P. M., Johnk, K. D., Ibelings, B. W., Mur, L. R., and Huisman, J., 2005, Benthic-pelagic coupling in the population dynamics of the harmful cyanobacterium Microcystis: Freshwater Biology, vol. 50, pp. 854–867, doi:10.1111/j.1365-2427.2005.01368.x.

Weibel, R. and Friis, H., 2007, Chapter 10: Alteration of opaque heavy minerals as a reflection of the geochemical conditions in depositional and diagenetic environments: *In* Developments in Sedimentology, Elsevier, pp. 277–303, doi:10.1016/s0070-4571(07)58010-6.

Weibel, R. and Grobety, B., 1999, Pseudomorphous transformation of goethite needles into hematite in sediments of the Triassic Skagerrak Formation, Denmark: Clay Minerals, vol. 34, pp. 657–660, doi:10.1180/000985599546415.

Wellman, C. H. and Strother, P. K., 2015, The terrestrial biota prior to the origin of land plants (embryophytes): a review of the evidence: Palaeontology, vol. 58, pp. 601–627, doi:10.1111/pala.12172.

White, W. S. and Wright, J. C., 1954, The White Pine copper deposit, Ontonagon County, Michigan: Economic Geology, vol. 49, pp. 675–716, doi:10.2113/gsecongeo.49.7.675.

Wilmeth, D. T., Dornbos, S. Q., Isbell, J. L., and Czaja, A. D., 2014, Putative domal microbial structures in fluvial siliciclastic facies of the Mesoproterozoic (1.09 Ga) Copper Harbor Conglomerate, Upper Peninsula of Michigan, USA: Geobiology, vol. 12, pp. 99–108, doi:10.1111/gbi.12071.

Woltz, C., Porter, S., Agić, H., Dehler, C., Junium, C., Riedman, L., Hodgskiss, M., Wörndle, S., and Halverson, G., 2020, Total organic carbon and the preservation of organic-walled microfossils in Precambrian shale: Geology, vol. 49, pp. 556–560, doi:10.1130/g48116.1.

Woodruff, L. G., Schulz, K. J., Nicholson, S. W., and Dicken, C. L., 2020, Mineral deposits of the Mesoproterozoic Midcontinent Rift system in the Lake Superior region – A space and time classification: Ore Geology Reviews, vol. 126, p. 103,716, doi:10.1016/j.oregeorev.2020.103716.

Slotznick, S.P., Swanson-Hysell, N.L., Zhang, Y., Clayton, K.E., Wellman, C.H., Tosca, N.J., and Strother, P.K., 2023, Reconstructing the paleoenvironment of an oxygenated Mesoproterozoic shoreline and its record of life: GSA Bulletin, https://doi.org/10.1130/B36634.1.

Supplemental Material

Figure S1. Low-temperature rock magnetic experiment data for Facies 1 specimens.

Figure S2. Low-temperature rock magnetic experiment data for Facies 2 specimens.

Figure S3. Low-temperature rock magnetic experiment data for Facies 3 specimens.

Figure S4. Cross-plots of rock magnetic parameters delineating magnetic facies.

Figure S5. Petrographic data from PC-1 and PRF18.

Figure S6. Rock magnetic data from core WPB4.

Figure S7. XRD data from bulk specimens.

Figure S8. XRD data from clay peels.

Figure S9. XRD minerals versus iron speciation oxalate extraction.

Figure S10. Thermal demagnetization data for specimen with “mht” component.

Figure S11. Inclination shallowing correction applied to Nonesuch paleomagnetic data.

Figure S12. Example images of categorized organic material.

Figure S13. Provisional palynomorph taxa in stratigraphic context.

Table S1. Mean paleomagnetic poles for the Nonesuch Formation.

Table S2. Nonesuch rock magnetic data.

Table S3. Summary of palynological data.

Supporting Information for "Reconstructing the paleoenvironment of an oxygenated Mesoproterozoic shoreline and its record of life"

Sarah P. Slotznick[1], Nicholas L. Swanson-Hysell[2], Yiming Zhang[2], Katherine E. Clayton[3], Charles H. Wellman[4], Nicholas J. Tosca[5], Paul K. Strother[6]

[1]Department of Earth Sciences, Dartmouth College, Hanover, NH, USA
[2]Department of Earth and Planetary Science, University of California, Berkeley, CA, USA
[3]Department of Earth Sciences, University of Oxford, Oxford, UK
[4]Department of Animal and Plant Sciences, University of Sheffield, Sheffield, UK
[5]Department of Earth Sciences, University of Cambridge, Cambridge, UK
[6]Department of Earth and Environmental Sciences, Weston Observatory of Boston College, Weston, MA, USA

List of Figures

S1 Low-temperature rock magnetic experiment data for Facies 1 specimens 2
S2 Low-temperature rock magnetic experiment data for Facies 2 specimens 3
S3 Low-temperature rock magnetic experiment data for Facies 3 specimens 4
S4 Cross-plots of rock magnetic parameters delineating magnetic facies 5
S5 Petrographic data from PC-1 and PRF18 6
S6 Rock magnetic data from core WPB4 7
S7 XRD data from bulk specimens 8
S8 XRD data from clay peels 9
S9 XRD minerals versus iron speciation oxalate extraction 10
S10 Thermal demagnetization data for specimen with "mht" component 11
S11 Inclination shallowing correction applied to Nonesuch paleomagnetic data 12
S12 Example images of categorized organic material 13
S13 Provisional palynomorph taxa in stratigraphic context 14

List of Tables

S1 Mean paleomagnetic poles for the Nonesuch Formation 15
S2 Nonesuch Rock Magnetic Data (published as accompanying Excel spreadsheet) 16
S3 Summary Palynological Data (published as accompanying Excel spreadsheet) 16

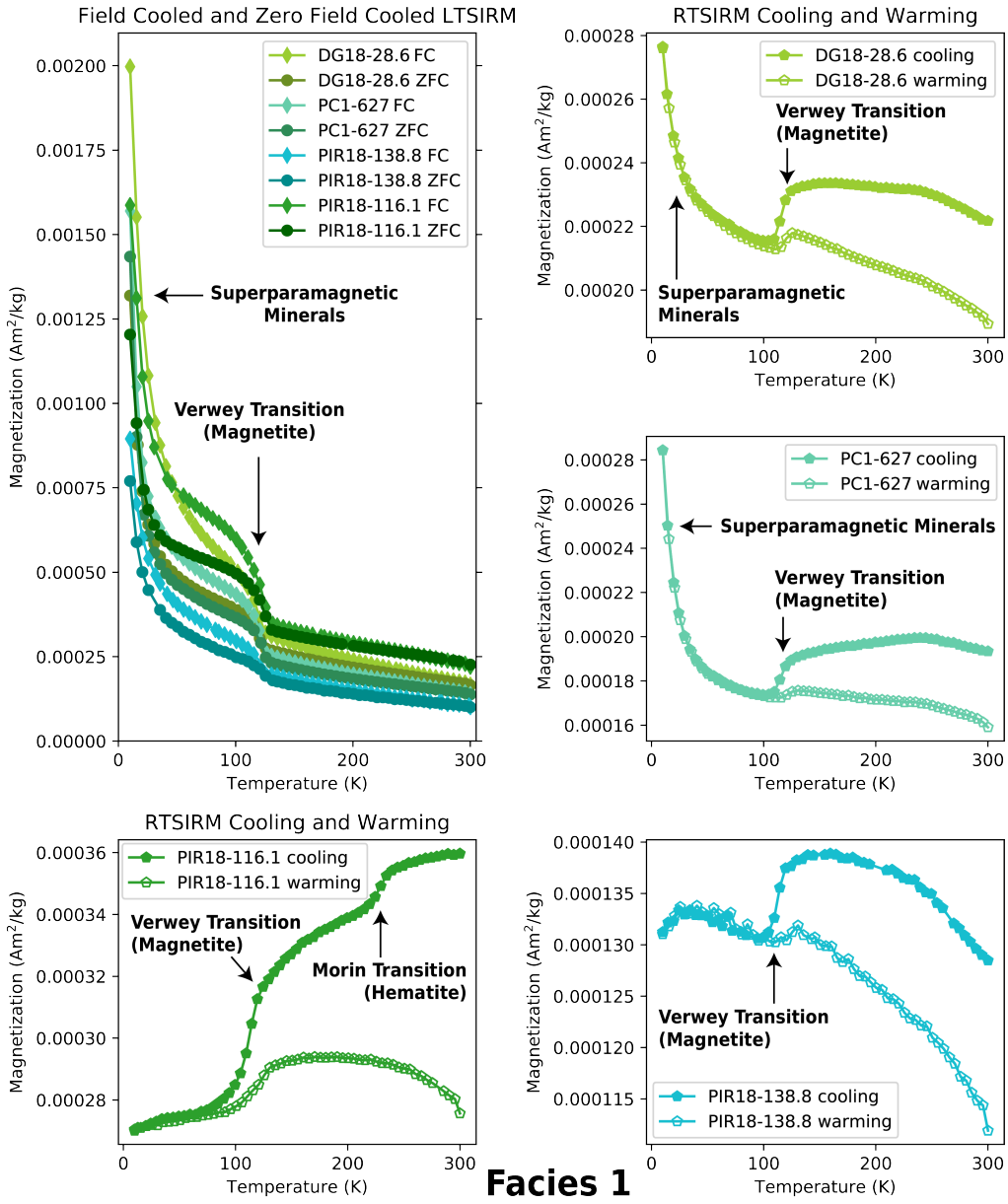

Figure S1. Low-temperature saturation isothermal remanent magnetization (LTSIRM) and room-temperature saturation isothermal remanenent magnetization (RTSIRM) curves for samples identified as Facies 1 from the outcrop sections at Brownstone Falls (DG18) and Presque Isle River (PIR18) as well as core PC-1 from the same region as PIR18 (Fig. 1). Both LTSIRM and RTSIRM curves record the Verwey transition, identifying magnetite within the samples (Verwey, 1939; Feinberg et al., 2015). The total magnetization (y-axis) and thus the total abundance of magnetite is one order of magnitude lower in these samples than in Facies 2 (Fig. S2). Relative to this low ferromagnetic content, superparamagnetic phases are abundant as noted by the elevated magnetization at <30 K especially pronounced in the field-cooled (FC) and zero-field cooled (ZFC) LTSIRM data.

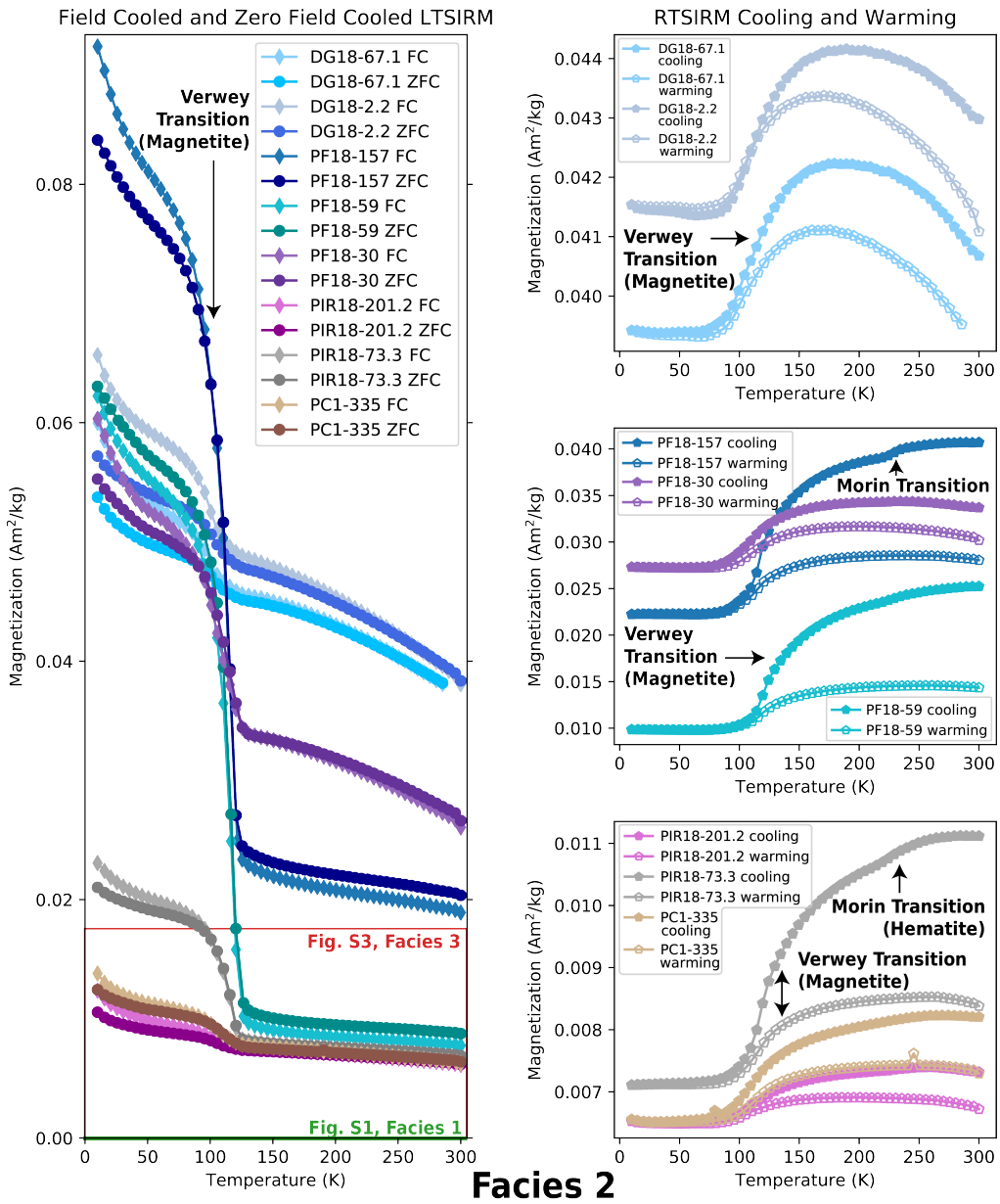

Figure S2. Low-temperature remanent magnetization curves for samples identified as Facies 2 from outcrop sections at Brownstone Falls (DG18), Potato River Falls (PF18) and Presque Isle River (PIR18) as well as core PC-1 from the same region as PIR18 (Fig. 1). For abbreviations see Fig. S1. The Verwey transition is noted in all experiments identifying magnetite within the samples. However, the total magnitude of the transition and the shape between locations indicating differences in abundance, grain size and/or composition. We interpret this to be due to differences in detrital input in each region potentially with slightly different provenance. The Morin transition associated with hematite is observed in some samples, but in many, it may be masked due to the abundance of magnetite or the non-stoichiometric chemistry/crystal structure common in natural samples (Morin, 1950; Wang et al., 2015). Boxes in the LTSIRM plot denote the scale of y-axis in the Facies 1 (Fig. S1) and Facies 3 (Fig. S3) plots wherein the detrital material has been reduced or oxidized respectively reducing the magnitude of the saturation magnetization.

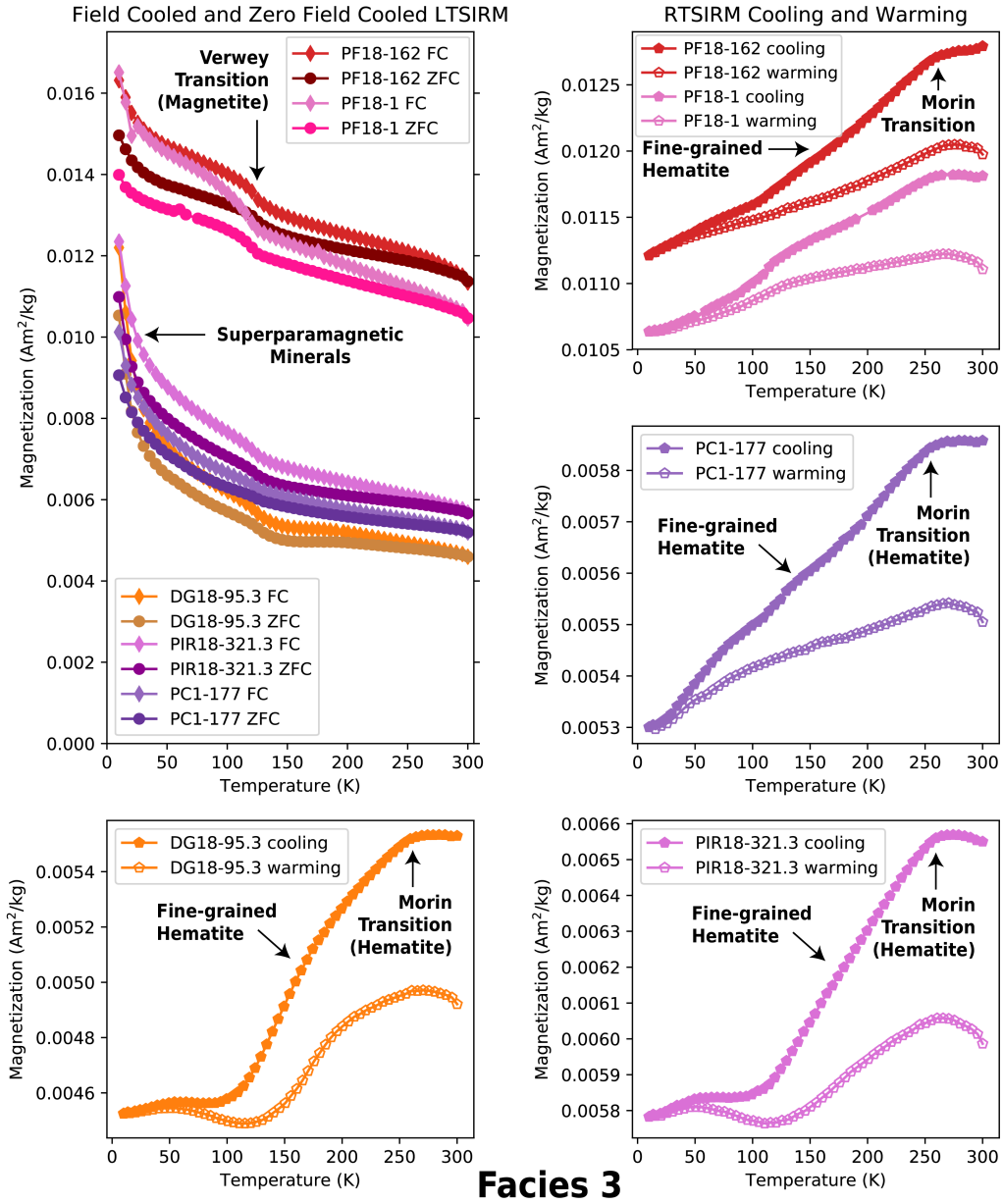

Figure S3. Low-temperature remanent magnetization curves for samples identified as Facies 3 from outcrop sections at Brownstone Falls (DG18), Potato River Falls (PF18) and Presque Isle River (PIR18) as well as core PC-1 from the same region as PIR18 (Fig. 1). For abbreviations see Fig. S1. In the LTSIRM experimental data, we see a reduction of total magnetization and the Verwey transition compared to Facies 2 (Fig. S2) consistent with oxidation. RTSIRM curves all contain a Morin transition at $\sim$ 250 K, but the progressive decrease in magnetization upon cooling could be from fine-grained pigmentary hematite ($<$ 90 nm) which has a wide range of Morin transition temperatures (Özdemir et al., 2008).

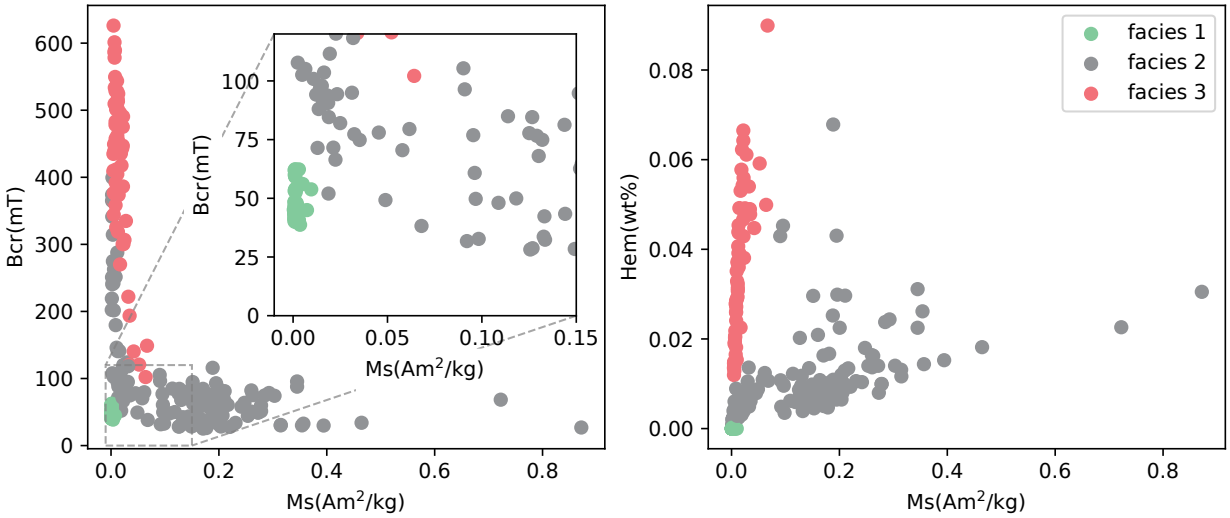

Figure S4. Cross-plots of rock magnetic parameters that delineate the magnetic facies as described in the main text. Plotted data is a compilation from all three outcrop sections and three drill cores (PC-1 and previously published DO-8 and WC-9 (Slotznick et al., 2018).) Bcr = coercivity of remanence; Ms = saturation magnetization.

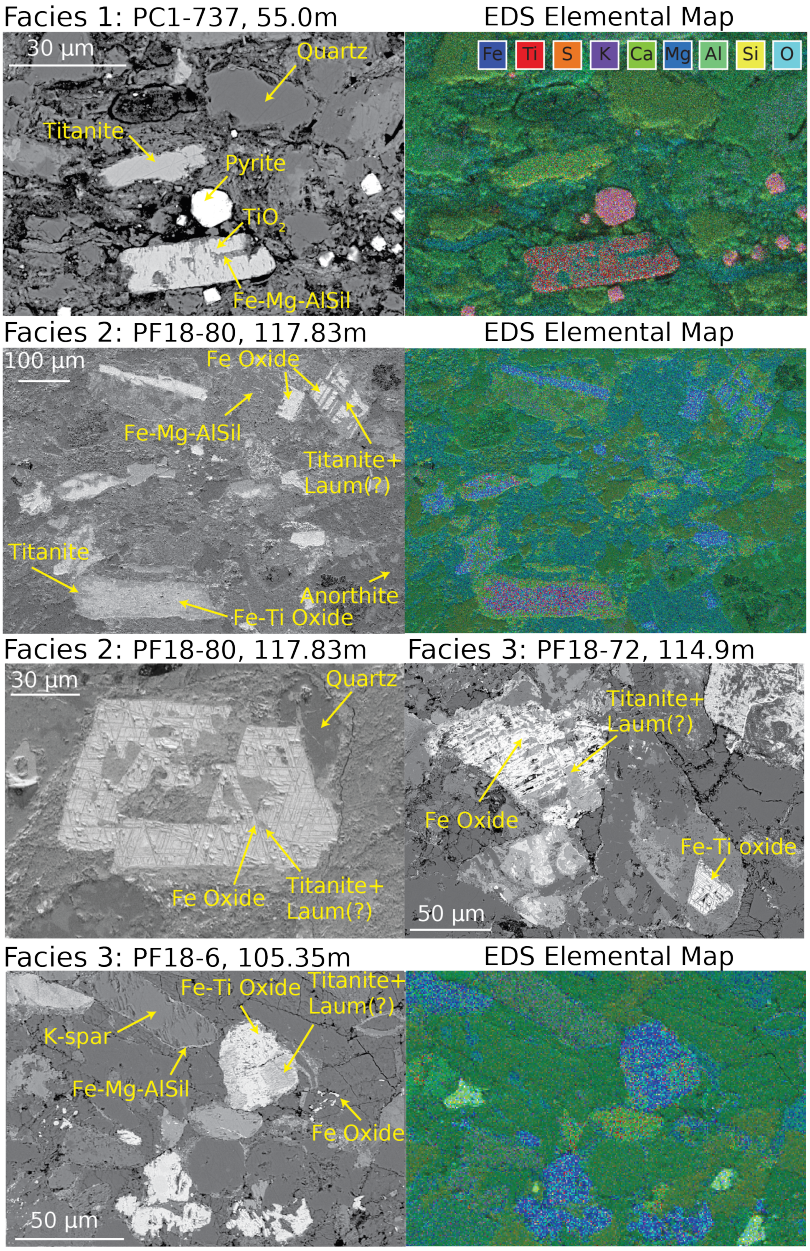

Figure S5. Representative backscatter electron images with mineral identifications via energy dispersive X-ray spectroscopy (EDS); EDS elemental maps are shown for three of the five images with the same color scheme/legend used for all of them. Facies 1 contains abundant pyrite with no obvious iron oxides only titanium oxides. An iron-magnesium alumnosilicate (Fe-Mg-AlSil), potentially chlorite or another clay mineral, is found closely associated with the titanium oxide perhaps forming authigenically during dissolution of the grain. Another iron-magnesium alumnosilicate grain is seen deformed by an overlying grain suggesting it is detrital. Facies 2 contains abundant grains of iron oxides and iron-titanium oxides with high-temperature oxyexsolution textures suggesting they are of igneous origins and detrital in nature. Close association with titanite (and perhaps laumontite (Laum?)) is noted in many of these phases. Facies 3 also has evidence for detrital iron (titanium) oxides which also are intermixed with titanite (and perhaps laumontite). Fine-grained authigenic iron oxides have formed in interstitial spaces between grains.

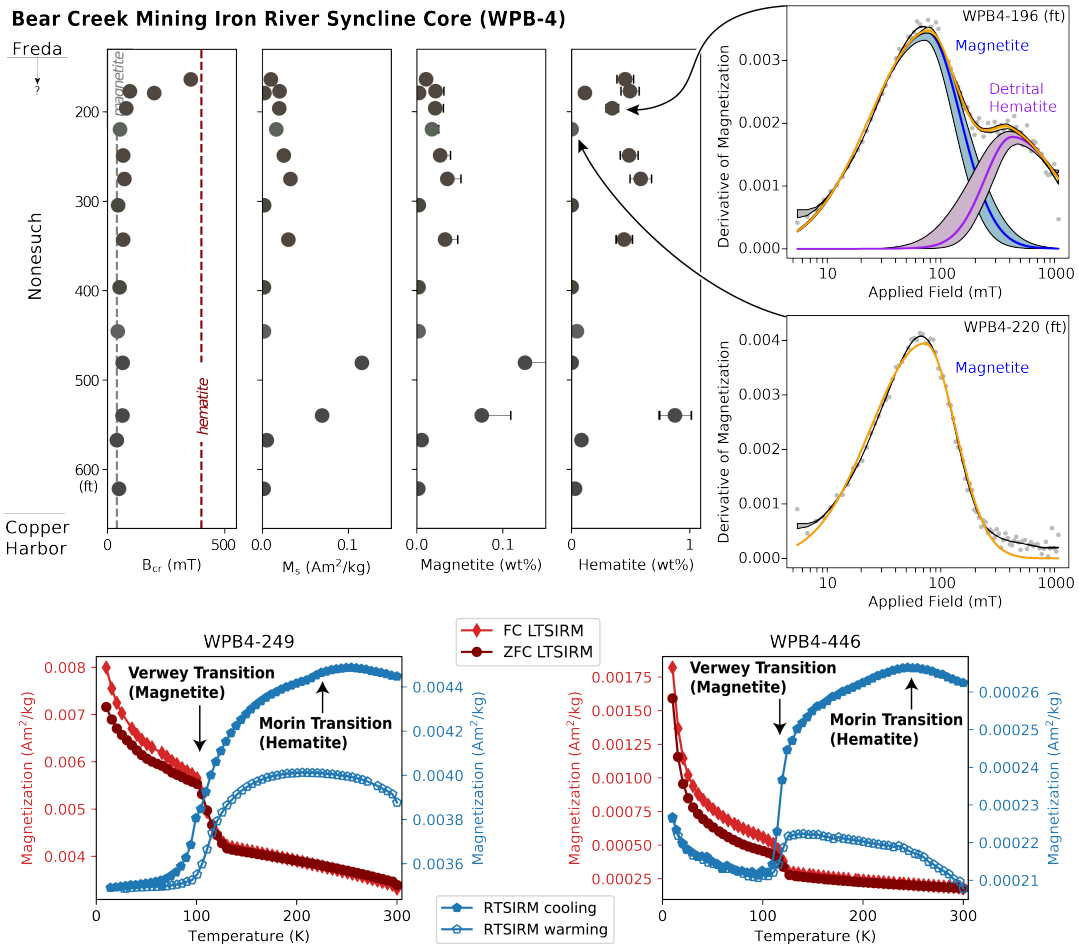

Figure S6. WPB-4 rock magnetic data plotted stratigraphically as well as low-temperature rock magnetic experiment data for two samples. Magnetic parameters and absolute quantification of magnetic minerals followed procedure for other drill cores (see Appendix for details.) Example representative coercivity spectra are shown. Magnetite and hematite are both identified via low-temperature analyses and these remanent magnetization curves do not look remarkably distinct from other cores. However, the WPB-4 rock magnetic data shows distinct stratigraphic patterns when compared to other sections. For example, samples with high M_s (saturation magnetization) occur lower in the stratigraphic section and sometimes have low levels or no hematite identified via coercivity spectra. One such sample (WPB4-220) as well as other horizons of the core had a chroma of green-yellow (Munsell code of GY). Similarly while low abundances of high-coercivity hematite are seen throughout the core, none of the analyzed samples had a Munsell chroma greater than 1 (interpreted to indicate pigmentary hematite.) These observations suggested caution in applying the magnetic facies interpretations from other sections so we have not done so; instead data points are colored using Munsell color data (Table S2). No detailed stratigraphic log was made for this section, but detailed analyses of the lower transition suggested a formation contact at 649.5 ft; however, the upper transition to sustained fluvial facies is unknown, occurring somewhere below 139.5 ft core depth. For abbreviations see Fig. S1, B_{cr} = coercivity of remanence.

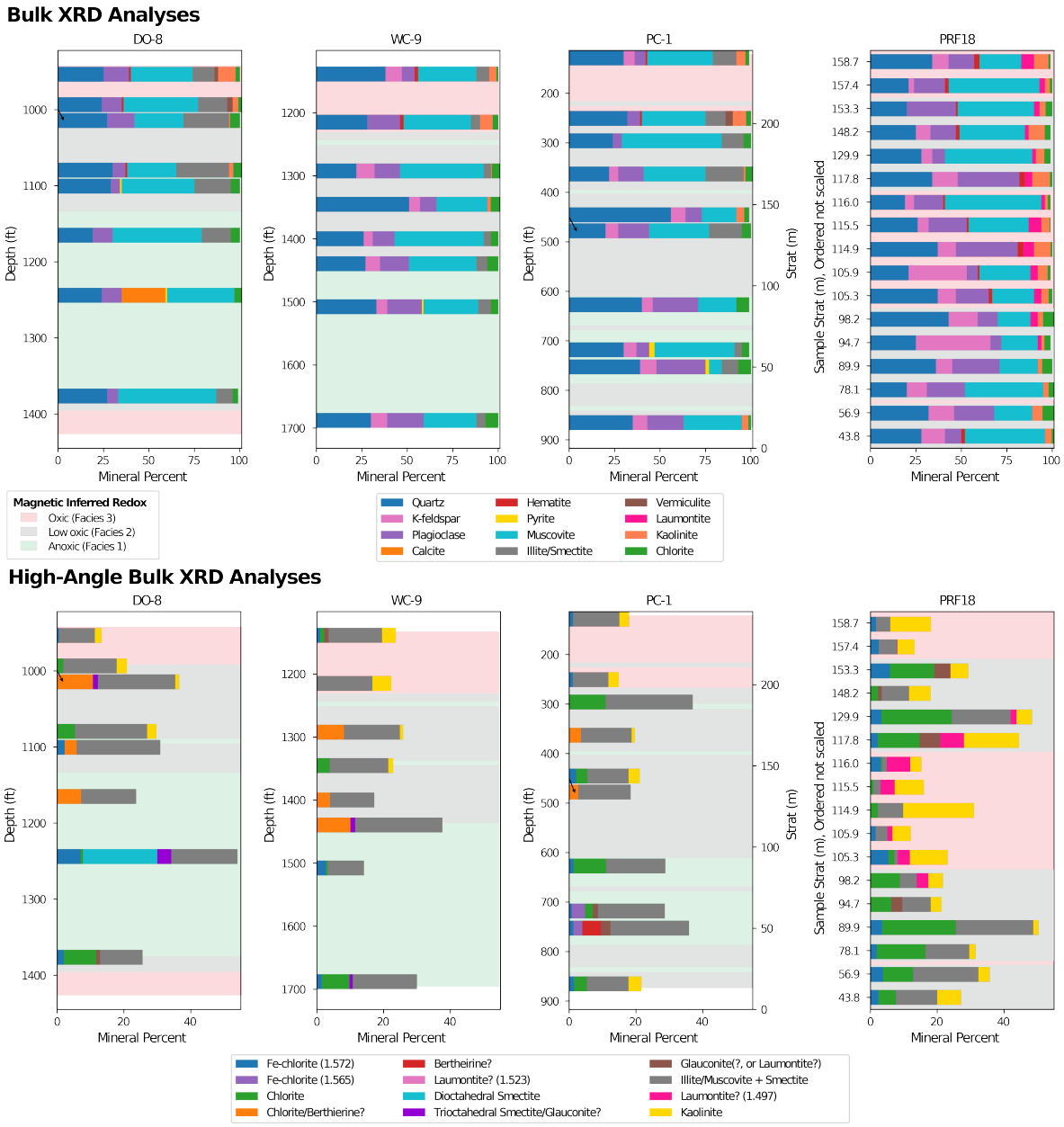

Figure S7. X-ray diffraction (XRD) mineral percent for bulk powdered specimens from cores DO-8, WPB-4, PC-1, and outcrop section PRF18. Magnetic inferred redox is shown in the light shading behind the data for comparison. Core data is plotted stratigraphically, while for ease of viewing, data from PRF18 is ordered stratigraphically but relative distances between samples are not kept to scale. Additionally, note the arrows showing that one sample in DO-8 and PC-1 are moved slightly from their stratigraphic positions. The upper plots represent bulk XRD analyses whereas the lower represent distinct analyses focused on the high-angle region of the diffraction pattern to specifically interrogate clay mineralogy. When multiple peaks or shifted peaks were observed for the same mineral, the theta angle is noted. Berthierine cannot be distinguished from chamosite in these XRD analyses so listed identifications of berthierine here could actually be either phase or a mixture.

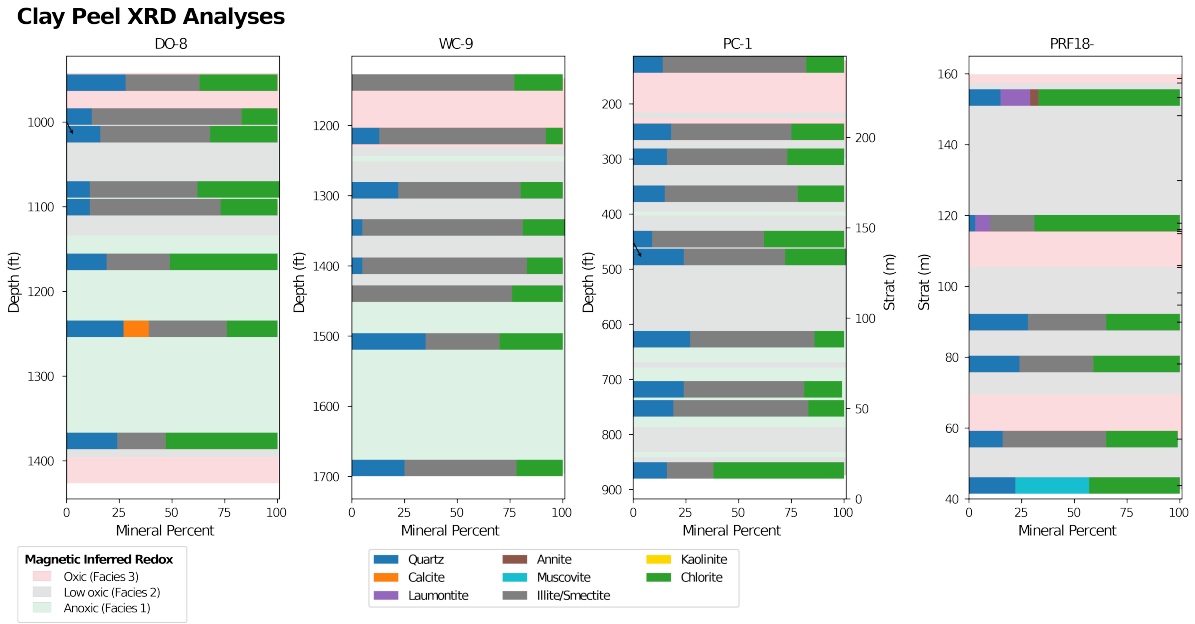

Figure S8. XRD mineral percent for clay peels of specimens from cores DO-8, WPB-4, PC-1, and outcrop section PRF18. Magnetic inferred redox is shown in the light shading behind the data for comparison. Data is plotted stratigraphically except one sample in DO-8 and PC-1 are moved slightly from their stratigraphic positions as noted by the arrows. Not all samples from PRF18 were analyzed using this technique; ticks on the right side of the plot show the stratigraphic position of all samples in Fig. S7.

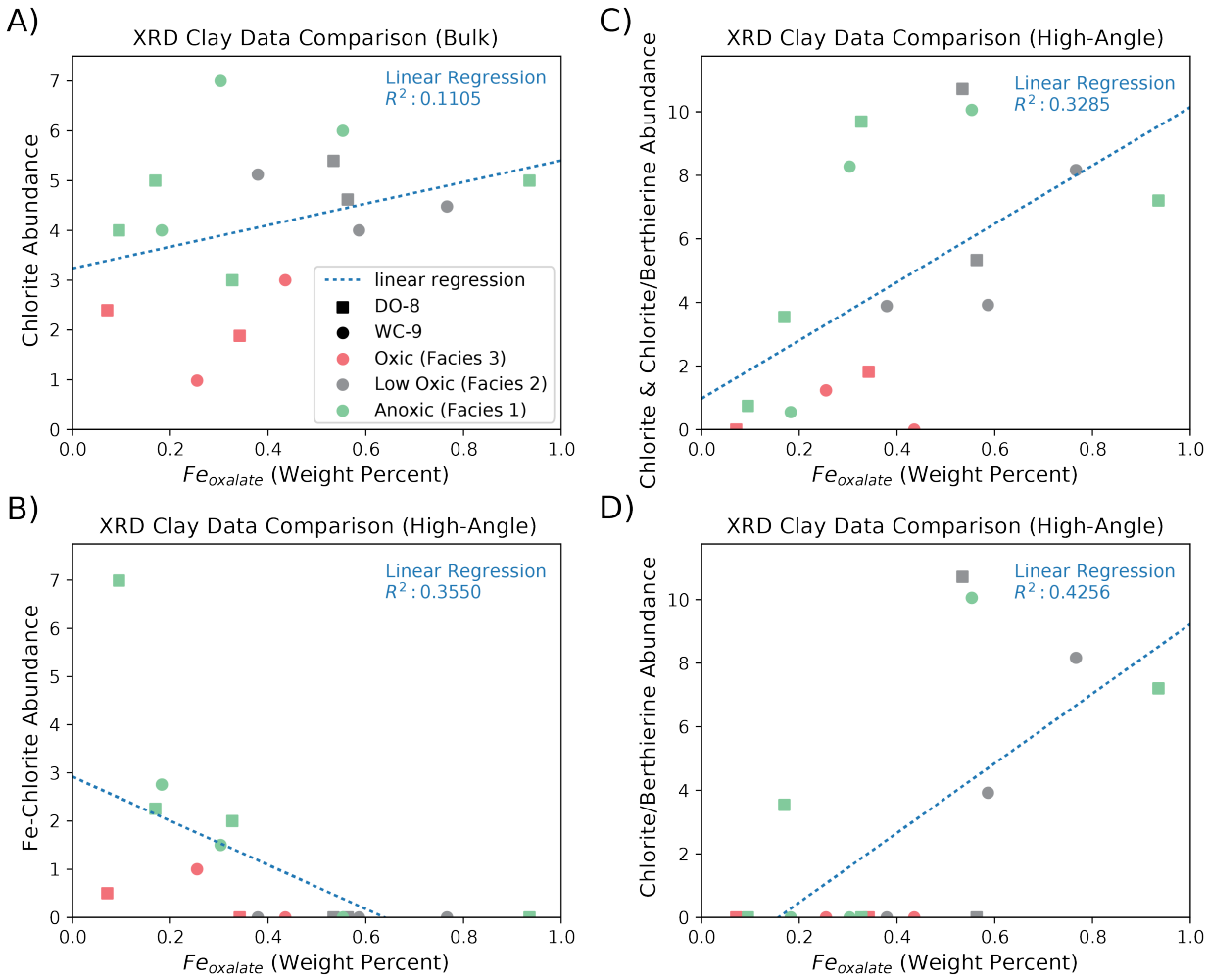

Figure S9. Selected comparison plots that showed a correlation between certain iron-bearing clays and iron extracted during the oxalate step of the iron speciation sequential extraction ($Fe_{oxalate}$.) Iron speciation extractions on a paired specimen were only performed on cores DO-8 and WC-9 (Slotznick et al., 2018) so only XRD data from those cores is utilized. Chlorite as determined by bulk XRD analyses (top of Fig. S7) has a weak but positive correlation with $Fe_{oxalate}$ (A). When interrogated in more depth and separated by specific clay minerals, a negative correlation is seen with Fe-chlorite (Fe-chlorite (1.572) in Fig. S7 as Fe-chlorite (1.565) is only noted in core PC-1) (B). A positive correlation is seen of other chlorite minerals and berthierine (C). This becomes statistically more robust when only the chlorite/berthierine minerals are considered (Fig. S7, berthierine? minerals are only noted in core PC-1), but there also is a decrease in sample number (D). Overall, this supports analyses of Slotznick et al. (2020) suggesting $Fe_{oxalate}$ includes iron from berthierine/chamosite minerals.

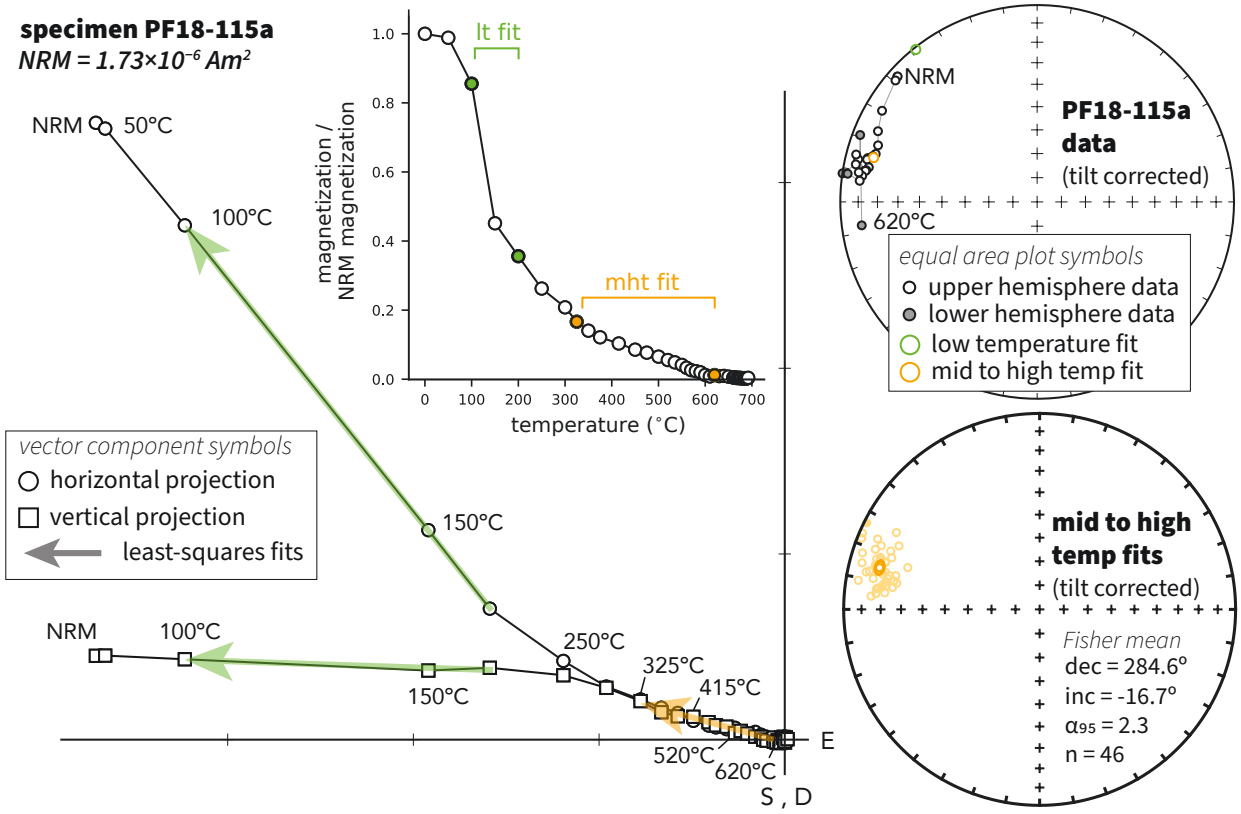

Figure S10. Thermal demagnetization paleomagnetic data for a specimen (PF18-115a) with the "mht" component shown as vector component plots, magnetic moment plots and equal area plots. Samples with this component are fine to medium-grained sandstone. These specimens typically have a large low-temperature overprint (shown with green arrow in the vector component plot) and a component that progressively unblocks from ~325 to 620°C with minimal remanence above this component. The specimen equal area plot shows data up to the 620°C step as the directions are unstable above that step. The "mht" component directions are shown for the 44 samples that had this component in the lower right equal area plot. The component has a direction similar direction to the pigmentary hematite (upper hemisphere) and is therefore interpreted to have formed through secondary fluid migration through the higher permeability sandstones. NRM = natural remanent magnetization.

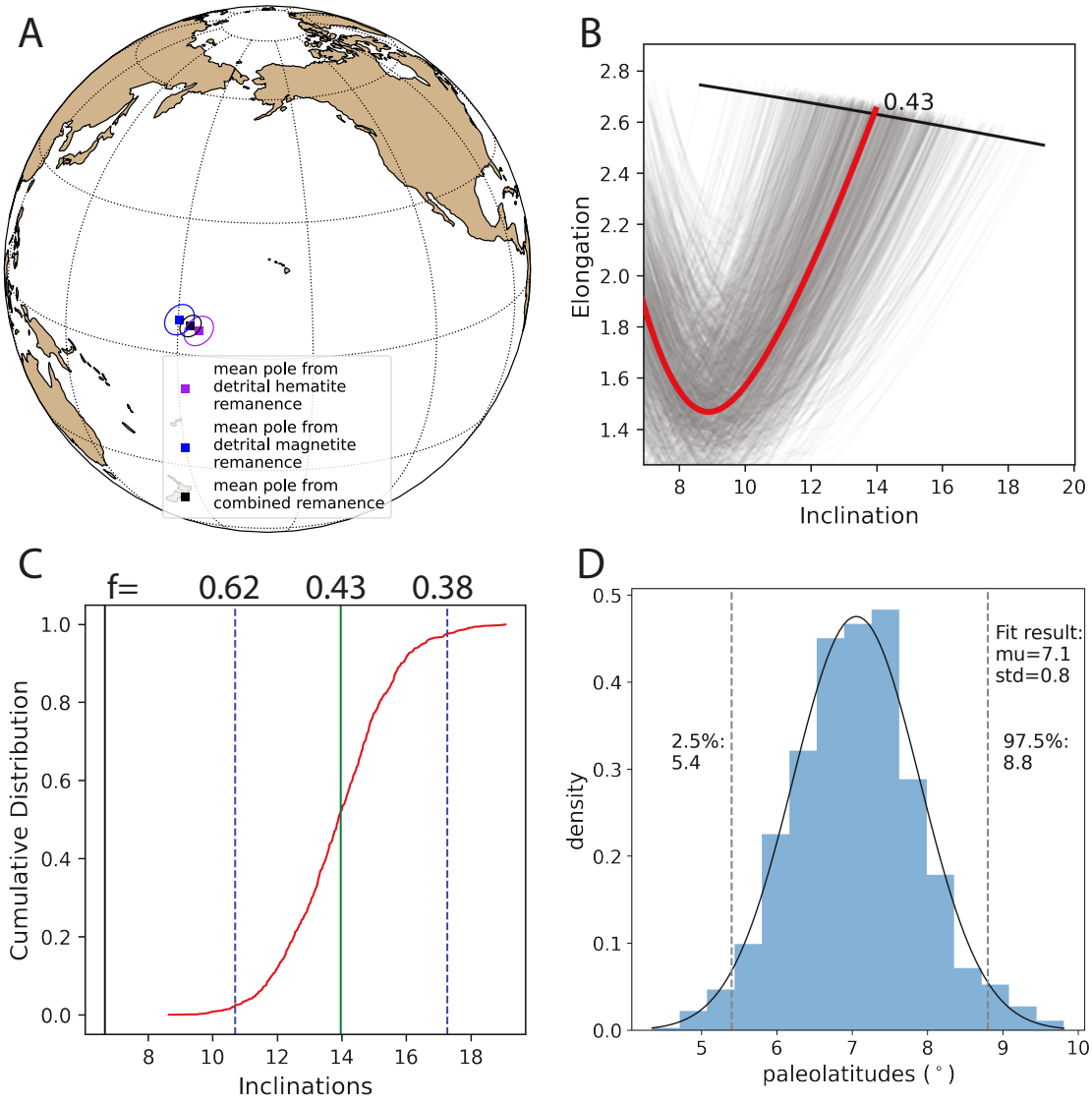

Figure S11. Results of the estimated amount of inclination shallowing of the detrital remanent magnetization of the Nonesuch Formation using the elongation/inclination method (Tauxe & Kent, 2004). (A) The resultant mean paleomagnetic poles of the detrital hematite remanence (purple), detrital magnetite remanence (blue), and combined detrital hematite and magnetite remanence (black) incorporating inclination shallowing uncertainty using the method of (Pierce et al., 2022) (poles positions detailed in Table S1). (B) For the combined detrital data, the E/I method results in an estimated flattening factor of f=0.43 (red curve) based on where elongation/inclination intersects that predicted by the TK03 paleosecular variation model (black curve). The grey lines show the analysis applied to 1,000 bootstrap resamples which provide an estimate of the uncertainty associated with the f factor estimate. C) The cumulative distribution of all plausible inclinations from the E/I bootstrap results. D) The distribution of the paleolatitudes implied from the mean inclinations that result from the E/I method bootstrap resamples. The 95% bounds span a range of paleolatitude that needs to be incorporated into the uncertainty on the resulting paleomagnetic pole. Incorporating the uncertainty on the mean position increases the uncertainty on the paleolatitude. Applying the method of Pierce et al. (2022) gives a paleolatitude of 7.1±2.8° N for the PRF18 locality at the time of Nonesuch deposition.